

**INVESTIGATION OF CORRELATION
BETWEEN 1/F ELECTRONIC NOISE AND
STRUCTURAL PROPERTIES IN NANO SIZED
VANADIUM OXIDE FILMS**

Master of Science Thesis

Emrah DİRİCAN

Eskişehir, 2017

**INVESTIGATION OF CORRELATION BETWEEN 1/F ELECTRONIC NOISE AND
STRUCTURAL PROPERTIES IN NANO SIZED VANADIUM OXIDE FILMS**

Emrah DİRİCAN

MASTER OF SCIENCE THESIS

Material Science and Engineering Department

Supervisor: Prof. Dr. Ramis Mustafa ÖKSÜZOĞLU

Eskişehir

Anadolu University

Graduate School of Sciences

November, 2017

This thesis study was supported by Anadolu University Scientific Research Project (BAP) Commission with Project No: 1604F171 and Technological Research Council of Turkey (TUBITAK) within the scope of 1001 project with Project No: 213M494

FINAL APPROVAL FOR THESIS

This thesis titled “Investigation of correlation between 1/f electronic noise and structural properties in nano sized vanadium oxide films” has been prepared and submitted by Emrah Dirican in partial fulfillment of the requirements in “Anadolu University Directive on Graduate Education and Examination” for the Degree of Master of Science in Material Science and Engineering has been examined and approved on 21/11/2017

Committee Members

Signature

Member (Supervisor)	: Prof. Dr. Ramis Mustafa ÖKSÜZOĞLU
Member	: Prof. Dr. Hasan Hüseyin ERKAYA
Member	: Assoc. Prof. Dr. Erhan AYAS

.....

Director

Graduate School of Sciences

ABSTRACT

INVESTIGATION OF CORRELATION BETWEEN 1/F ELECTRONIC NOISE AND STRUCTURAL PROPERTIES IN NANO SIZED VANADIUM OXIDE FILMS

Emrah DİRİCAN

Department of Material Science and Engineering

Anadolu University, Graduate School of Sciences, November, 2017

Supervisor: Prof. Dr. Ramis Mustafa ÖKSÜZOĞLU

Vanadium oxide thin films are used in microbolometer pixels as the sensing layer. Their electrical properties such as resistivity, the temperature coefficient of resistance and 1/f electronic noise are closely related to their structural properties. In this study, VO_x thin films were deposited on Si₃N₄/SiO₂/Si substrates by pulsed DC reactive magnetron sputtering technique. Some of the films were post-deposition annealed at 200°C and 300°C under pure N₂ atmosphere for three hours. The post-annealing effects on the films' structures were investigated by transmission electron microscopy, selected area electron diffraction, electron spectroscopic imaging, Grazing-Incidence X-Ray diffraction, Raman spectroscopy, and X-Ray photoelectron spectroscopy techniques. For electrical characterization, four-point probe technique was used. The correlation between electrical and structural properties of the films was discussed within the framework of the obtained results. The 1/f noise-structure correlation was discussed on the basis of the 1/f noise results obtained by our research group in a previous study. As a result of these discussions, it was concluded that the different 1/f noise values of as-deposited, 200°C and 300°C annealed films are mainly caused by the different VO₂ grain size of these films. In addition, the electrical conduction mechanism of 200°C annealed film was explained by charge hopping.

Keywords: Vanadium oxide thin film, Pulsed DC reactive magnetron sputtering, Selected area electron diffraction, Electron spectroscopic imaging, 1/f noise.

ÖZET

NANO ÖLÇEKLİ VANADYUM OKSİT FİLMERDE 1/F ELEKTRONİK GÜRÜLTÜ İLE YAPISAL ÖZELLİKLER ARASINDAKİ İLİŞKİNİN İNCELENMESİ

Emrah DİRİCAN

Malzeme Bilimi ve Mühendisliği Anabilim Dalı

Anadolu Üniversitesi, Fen Bilimleri Enstitüsü, Kasım, 2017

Danışman: Prof. Dr. Ramis Mustafa ÖKSÜZOĞLU

Vanadyum oksit ince filmler mikrobolometre piksellerinde algılayıcı katman olarak kullanılmaktadır. Bu filmlerin, özdirenç, direncin sıcaklık katsayısı ve 1/f elektronik gürültü gibi elektriksel özellikleri yapısal özellikleriyle yakından ilişkilidir. Bu çalışmada, vanadyum oksit ince filmler $\text{Si}_3\text{N}_4/\text{SiO}_2/\text{Si}$ altaşlar üzerine darbeleri DC reaktif magnetron sıçratma tekniği ile büyütülmüştür. Üretim sonrası bazı filmlere 200°C ve 300°C sıcaklıklarda, saf N_2 atmosferi altında üç saat süreyle ısıl işlem uygulanmıştır. Üretim sonrası ısıl işlemlerin, filmlerin yapısal özellikleri üzerindeki etkisi geçirimli elektron mikroskobu, seçili alan elektron kırınımı, elektron spektroskopik görüntüleme, sıyırma açısı X-Işını kırınımı, Raman spektroskopisi ve X-Işını fotoelektron spektroskopisi teknikleriyle incelenmiştir. Elektriksel karakterizasyonlar için dört-nokta iğne tekniği kullanılmıştır. Filmlerin elektriksel ve yapısal özellikleri arasındaki ilişki elde edilen sonuçlar çerçevesinde tartışılmıştır. 1/f gürültü-yapı ilişkisi, araştırma grubumuzca daha önceki bir çalışmada elde edilen 1/f gürültü sonuçları temelinde tartışılmıştır. Yapılan bu tartışmalar sonucunda, tavlansız, 200°C ve 300°C ' de tavlansız numunelerin farklı 1/f gürültü değerlerinin, bu filmlerin farklı VO_2 tane boyutundan kaynaklandığı sonucuna varılmıştır. Buna ek olarak, 200°C ' de tavlansız filmin elektriksel iletkenlik mekanizması yük atlaması ile açıklanmıştır.

Anahtar Sözcükler: Vanadyum oksit ince film, Darbeleri DC reaktif magnetron sıçratma, Seçili alan elektron kırınımı, Elektron spektroskopik görüntüleme, 1/f gürültü.

ACKNOWLEDGEMENT

First of all, I would like to express my deepest gratitude to my supervisor Prof. Dr. Ramis Mustafa Öksüzođlu for providing me with a rare laboratory environment and for guiding me through his knowledge and experience during my thesis study.

I am thankful to my colleagues Ercan Őener, Sinan Özgün, Ahmet Murat Yađcı, Can Yavru, Rifat Kaçar, Erdal Volkan Batur and Gökçenur Çakmak for their support and friendships. This journey has become more unforgettable with their sharings. I will always remember them with gratitude.

I would like to acknowledge the Scientific and Technological Research Council of Turkey (TUBITAK) for supporting me with the scholarship within the scope of 1001 project with the project no: 213M494. I would also like to thank the Scientific Research Projects Commission of Anadolu University as it supported this thesis study with the project no: 1604F171.

Last but not the least, I would like to express my best appreciation to my family members for their understanding and patience. Their unconditional love and help were always with me and I would not be successful on this challenging way without their support. For this reason, I dedicate this thesis study to them.

Emrah Dirican

Kasım, 2017

STATEMENT OF COMPLIANCE WITH ETHICAL PRINCIPLES AND RULES

I hereby truthfully declare that this thesis is an original work prepared by me; that I have behaved in accordance with the scientific ethical principles and rules throughout the stages of preparation, data collection, analysis and presentation of my work; that I have cited the sources of all the data and information that could be obtained within the scope of this study, and included these sources in the references section; and that this study has been scanned for plagiarism with “scientific plagiarism detection program” used by Anadolu University, and that “it does not have any plagiarism” whatsoever. I also declare that, if a case contrary to my declaration is detected in my work at any time, I hereby express my consent to all the ethical and legal consequences that are involved.

.....
Emrah Dirican

TABLE OF CONTENT

TITLE PAGE.....	i
FINAL APPROVAL FOR THESIS.....	ii
ABSTRACT	iii
ÖZET	iv
ACKNOWLEDGEMENT	v
STATEMENT OF COMPLIANCE WITH ETHICAL PRINCIPLES AND RULES	vi
TABLE OF CONTENT	vii
LIST OF TABLES.....	ix
LIST OF FIGURES	x
LIST OF VISUALS	xiii
LIST OF SYMBOLS.....	xiv
LIST OF ABBREVIATIONS.....	xv
1. INTRODUCTION	1
1.1. Structure of The Thesis.....	1
1.2. Vanadium Oxide Phases and Their Properties.....	1
1.3. Electrical Properties of Vanadium Oxide Thin Films Required for Microbolometer Applications.....	7
1.4. Literature Review of 1/f Noise Studies.....	11
1.5. Thin Film Production: Pulsed DC Reactive Magnetron Sputtering	13
1.6. Aim of the Study.....	19
2. MATERIALS AND METHODS	23
2.1. Fabrication of Thin Film Sample	23
2.1.1. Substrate preparation	23
2.1.2. Thin film deposition	24
2.1.3. Post-annealing process	26
2.2. Thin Film Characterization	27
2.2.1. Electrical characterization.....	27
2.2.1.1. Four-Point probe technique.....	27
2.2.2. Structural characterization	32
2.2.2.1. X-Ray diffraction technique.....	32
2.2.2.2. X-Ray photoelectron spectroscopy	34

2.2.2.3. Raman spectroscopy	38
2.2.2.4. Transmission electron microscopy	42
3. EXPERIMENTAL RESULTS	51
3.1. Electrical Results	51
3.2. Structural Characterization Results	58
3.2.1. Grazing-Incidence X-Ray diffraction results.....	58
3.2.2. Raman results.....	59
3.2.3. X-Ray photoelectron spectroscopy results	62
3.2.4. Transmission electron microscopy results.....	65
3.2.4.1. Selected area electron diffraction patterns	65
3.2.4.2. Transmission electron microscopy images	69
3.2.4.3. Elemental mapping.....	72
3.2.4.4. Pore size distribution study of the films	76
4. DISCUSSION.....	80
5. CONCLUSION.....	84
REFERENCES.....	88
RESUME	

LIST OF TABLES

Table 1.1. Sheet resistance and resistivity results of the as-deposited film deposited on the bare $\text{Si}_3\text{N}_4/\text{SiO}_2/\text{Si}$ substrate from the previous study [45]	21
Table 1.2. Electrical results of the VO_x thin films deposited on finger-structure electrodes [45]	21
Table 2.1. Production parameters of the deposited VO_x thin film samples.....	26
Table 2.2. Geometric correction factors for regular geometries [50].....	31
Table 2.3. Spectroscopic notations of electron energy levels based on principle quantum number, n ; orbital angular momentum, l ; spin angular momentum, s ; and total angular momentum, j	36
Table 2.4. Frequency shifts (cm^{-1}) of the VO_2 Raman peaks from the literature...	41
Table 2.5. Frequency shifts (cm^{-1}) of the V_2O_5 Raman peaks from the literature. .	42
Table 2.6. Frequency shifts (cm^{-1}) of the V_6O_{13} , V_2O_{13} and VO_x Raman peaks from the literature.	42
Table 2.7. Acquisition parameters of the ESI images	49
Table 3.1. Electrical results of the VO_x thin films deposited on $\text{Si}_3\text{N}_4/\text{SiO}_2/\text{Si}$ substrates. N.A. (no analysis) indicates that analysis could not be performed due to oscillations in voltage.	51
Table 3.2. Fitting parameters of vanadium and oxygen peaks observed in the spectra.....	64
Table 3.3. Fitting parameters of the satellite peaks observed in the spectra.....	65
Table 3.4. Interplanar spacing values ($d(\text{\AA})$) of some VO_x phases from PDFs; in order to compare with $d(\text{\AA})$ values measured from electron diffraction patterns of the as-deposited, 200°C and 300°C annealed films.....	66

LIST OF FIGURES

Figure 1.1. VO _x phase diagram [1]	2
Figure 1.2. Calculated binary phase diagram showing the formation energies of stable stoichiometries of VO _x . The inset is a magnified view [1].....	3
Figure 1.3. Phase diagrams of V ₂ O ₃ showing a) structural transformation under different temperature and applied pressure and b) unstable and metastable structures. PI, PM, and AFI imply paramagnetic insulator, paramagnetic metal and anti-ferromagnetic insulator, respectively [1]	4
Figure 1.4. Phase diagrams of V ₃ O ₅ showing a) structural transformation under different temperature and applied pressure and b) unstable and metastable structures. PM, PI, AFI imply paramagnetic metal, paramagnetic insulator, anti-ferromagnetic insulator, respectively [1]5	5
Figure 1.5. Phase diagrams of VO ₂ showing a) structural transformation under different temperature and applied pressure and b) unstable and metastable structures. PI and PM imply paramagnetic insulator paramagnetic metal, respectively [1].....	5
Figure 1.6. Phase diagrams showing a) unstable and metastable structures of V ₂ O ₅ and b) metastable phases [1].....	7
Figure 1.7. IR transmittance of the atmosphere [7]	8
Figure 1.8. Effect of working pressure and current on film deposition rate in simple DC sputtering [24]	15
Figure 1.9. Hysteresis behaviour of the system pressure with changing the reactive gas flow rate. The dotted line shows the pressure change when working gas flow rate is changed [24]	18
Figure 1.10. Hysteresis behaviour on cathode voltage and deposition rate with changing reactive gas flow rate at a constant current [24]	18
Figure 2.1. Sample holder showing the position of the samples.....	23
Figure 2.2. Comparison of circuit schemes of two-point and four-point configurations [47].....	27
Figure 2.3. Illustration of electrical measurement with FPP [49]	29
Figure 2.4. Parameters for the samples having regular geometric shapes [50]	30
Figure 2.5. Orientation of crystallographic planes in a thin film sample [51]	33
Figure 2.6. Schematic illustration of energy terms for the derivation of kinetic energy of the photoelectrons measured by analyzer [52]	35

Figure 2.7. Schematic illustration of an XPS system [55]	38
Figure 2.8. Energy diagram of Raman scattering.....	39
Figure 2.9. Geometry for electron diffraction and definition of camera length, L [61].....	44
Figure 2.10. a) Formation of diffraction spots and b) polycrystalline diffraction rings formed by crystals of same phase oriented differently [60]	45
Figure 2.11. Contrast formation in BF mode of TEM [60]	46
Figure 2.12. Three window method: Background is determined by the pre-edge images (ΔE_1 , ΔE_2) and subtracted from post-edge image (ΔE_3). Only the black area contributes to the corresponding elemental map [63]	48
Figure 3.1. lnR-versus-temperature curve of as-deposited film of VO _x -1	52
Figure 3.2. lnR-versus-temperature curve of as-deposited sample of VO _x -6	53
Figure 3.3. lnR-versus-temperature curve of VO _x -2 sample annealed at 200°C ...	54
Figure 3.4. lnR-versus-temperature curve of VO _x -3 sample annealed at 200°C ...	54
Figure 3.5. lnR-versus-temperature curve of VO _x -4 sample annealed at 200°C	55
Figure 3.6. lnR-versus-1000/T curves of the VO _x thin films: the curves were obtained from heating cycles.....	56
Figure 3.7. ln σ -vs-1000/T curves of the as-deposited and 200°C annealed films.	57
Figure 3.8. Pre-exponential factors σ_a as a function of the calculated activation energies (ΔE_a) of the VO _x thin films.....	58
Figure 3.9. XRD patterns of the VO _x thin films. VO _x indicates possible layered phases of VO _x , e.g., V ₆ O ₁₃ , V ₃ O ₇	59
Figure 3.10. Raman spectra of substrate, as-deposited, 200°C and 300°C annealed films	61
Figure 3.11. XPS spectra of as-deposited, 200°C and 300°C annealed films	64
Figure 3.12. SAED patterns of a) the substrate and b) the as-deposited film	67
Figure 3.13. SAED patterns of a) the 200°C and b) the 300°C annealed films.....	68
Figure 3.14. TEM images of the as-deposited film: a) BF, b) DF	69
Figure 3.15. HRTEM images of the as-deposited film showing the crystal regions with measured interplanar spacings.....	70

Figure 3.16. BF image of the 200°C annealed film	70
Figure 3.17. HRTEM image of the 200°C annealed film showing the crystal regions with measured interplanar spacings.....	71
Figure 3.18. BF image of the 300°C annealed film	71
Figure 3.19. TEM images of the 300°C annealed film: a) DF image b,c) HRTEM images showing the crystal regions with the measured interplanar spacings.....	72
Figure 3.20. Cross-sectional elemental maps of the as-deposited film: a) vanadium b) oxygen c) nitrogen.....	73
Figure 3.21. Cross-sectional elemental maps of the 200°C annealed film a) vanadium and b) oxygen	74
Figure 3.22. Cross-sectional nitrogen map of the 200°C annealed film.....	75
Figure 3.23. High angle annular dark field (HAADF) image of the 200°C annealed film. The inset image shows a magnified image.....	75
Figure 3.24. Cross-sectional elemental maps of the 300°C annealed film: a) vanadium b) oxygen c) nitrogen	76
Figure 3.25. Pore area determination steps: The image processing of the as-deposited film was given as an example.....	77
Figure 3.26. Pore area distribution histograms extracted from the vanadium maps	78
Figure 3.27. Pore area distribution histograms extracted from the oxygen maps	79

LIST OF VISUALS

Visual 2.1. Bestec Ultra High Vacuum Sputter System present at Advanced Technology Thin Film Laboratory of Anadolu University.....	25
Visual 2.2. FPP system present at Advanced Technology Thin Film Laboratory of Anadolu University.....	32
Visual 2.3. X'pert Pro MRD instrument present in Bilkent-UNAM	34
Visual 2.4. TECNAI F30 TEM instrument present in Bilkent-UNAM	49
Visual 2.5. NNL-600I FIB system present in Bilkent-UNAM	50

LIST OF SYMBOLS

Å	: Angström
Ar	: Argon
Ar ⁺	: Argon ion
e ⁻	: Electron
eV	: Electron-Volt
GPa	: Giga-Pascal
Hz	: Hertz
J	: Joule
K	: Kelvin
kHz	: Kilo-Hertz
kΩ	: Kilo-Ohm
kg	: Kilogram
mbar	: Mili-Bar
mK	: Mili-Kelvin
mA	: Mili-Amper
mTorr	: Mili-Torr
MΩ	: Mega-Ohm
μm	: Micro-Meter
nm	: Nano-Meter
N ₂	: Nitrogen gas
O ₂	: Oxygen gas
V	: Volt
sccm	: Standard cubic centimeters per minute
sq	: Square
~	: Approximately
°C	: Celcius degree
ρ	: Resistivity
Ω	: Ohm
λ	: Wavelength

LIST OF ABBREVIATIONS

AFI	: Anti-Ferromagnetic Insulator
BF	: Bright Field
CMOS	: Complementary Metal Oxide Semiconductor
DC	: Direct Current
DF	: Dark Field
ESI	: Electron Spectroscopic Imaging
EELS	: Electron Energy Loss Spectrum
FIB	: Focused Ion Beam
FPP	: Four-Point Probe
GIXRD	: Grazing Incidence X-Ray Diffraction
HRTEM	: High Resolution Transmission Electron Microscopy
IR	: Infrared
LWIR	: Long Wave Infrared
MIT	: Metal Insulator Transition
PDF	: Powder Diffraction File
PI	: Paramagnetic Insulator
PM	: Paramagnetic Metal
PECVD	: Plasma Enhanced Chemical Vapour Deposition
PDC-RMS	: Pulsed DC Reactive Magnetron Sputtering
PSD	: Power Spectral Density
RF	: Radio Frequency
ROIC	: Read Out Integrated Circuit
SAED	: Selected Area Electron Diffraction
TCR	: Temperature Coefficient of Resistance
TEM	: Transmission Electron Microscopy
VO _x	: Vanadium Oxide
XRD	: X-Ray Diffraction
XPS	: X-Ray Photoelectron Spectroscopy

1. INTRODUCTION

1.1. Structure of The Thesis

This thesis study is about vanadium oxide (VO_x) thin films used in microbolometers as sensing layer and includes their electrical and structural investigations. The structure of this thesis was planned as follows.

Chapter 1 provides a background to and emphasizes aim of the study. Section 1.2 presents the phase diagrams of VO_x and gives the properties of some important phases in detail. Section 1.3 exhibits information about the application. The general understanding of IR detection and working principle of a microbolometer are presented in this section. The important figure of merits affecting microbolometer performance and the electrical properties of the thin film layer influencing these figure of merits are given. As one important electrical property and the title of the study, the literature review of 1/f noise studies is presented in Section 1.4. Section 1.5 exhibits the theory of thin film deposition by pulsed direct current (DC) reactive magnetron sputtering (PDC-RMS) technique. Finally, Section 1.6 gives the research question and the aim of the study.

Chapter 2 consists of two main sections. Section 2.1 gives experimental details of the thin film deposition and subsequent post-annealing process. Section 2.2 gives a technical background of the characterization methods in addition to the experimental details.

Chapter 3 presents all obtained results with their explanations. The discussion of these results is made in Chapter 4. Finally, the conclusion is given in Chapter 5.

1.2. Vanadium Oxide Phases and Their Properties

Vanadium is a transition metal with [Ar]3d³4s² electronic configuration and forms many oxide compounds with oxygen. Each compound has different properties and influences the properties of the film when occurs. Therefore, this section seeks to the examination of VO_x phase diagrams and the properties of some VO_x phases included in these diagrams.

In Figure 1.1, an optimized VO_x phase diagram was presented from the work published by N. Bahlawane and D. Lenoble [1]. This phase diagram shows VO_x

phases whose oxygen fractions are in the range of 0.50-0.75. Beside the border phases, which are VO and VO₃, the diagram also includes two well-known phase groups; Magnèli phases with the general formula of V_nO_{2n-1}, between V₂O₃ and VO₂; and Wendsley phases with the general formula of V_nO_{2n+1} which are also known as layered vanadium oxides.

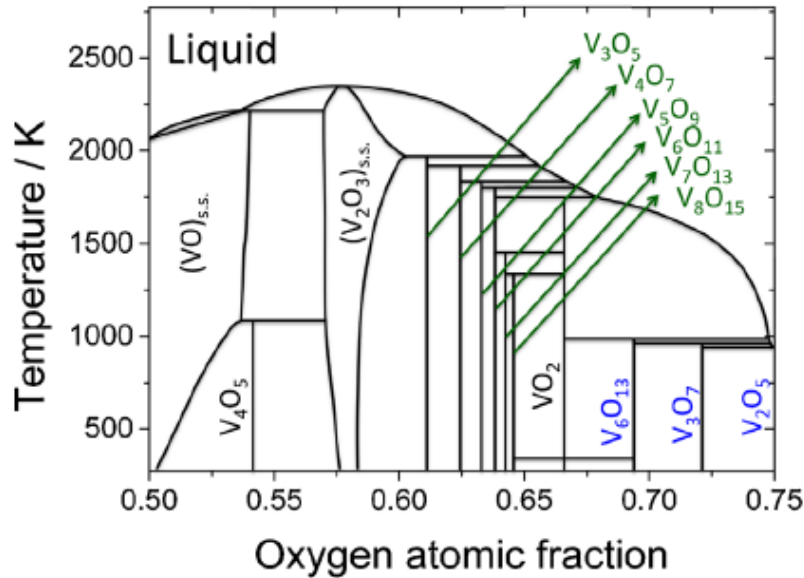


Figure 1.1. VO_x phase diagram [1]

While some stoichiometries of VO_x occur only in stable structures, the others also have unstable and metastable structures. Figure 1.2 presents the convex hull line of the calculated VO_x phase diagram. The dots on the line indicate the stable structures of the relevant phases. These contain cubic divanadium trioxide V₂O₃ (Ia3), monoclinic trivanadium pentoxide V₃O₅ (P2/c), tetragonal vanadium dioxide VO₂ (P42/mnm), monoclinic trivanadium heptaoxide V₃O₇ (C2/c), orthorhombic divanadium pentoxide V₂O₅ (Pmnm), and the monoclinic vanadium trioxide VO₃ (C2/m) [1].

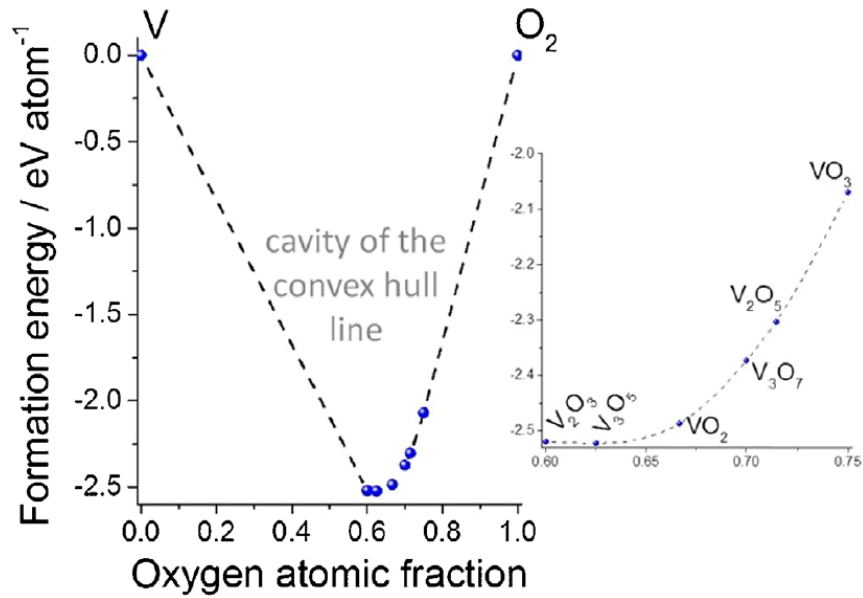


Figure 1.2. Calculated binary phase diagram showing the formation energies of stable stoichiometries of VO_x. The inset is a magnified view [1]

Vanadium sesquioxide, V₂O₃, exists in paramagnetic trigonal metal phase with the R3c symmetry at room temperature and crystallizes in corundum structure of VO₆ octahedra. Upon cooling, it changes its structure to a monoclinic insulating phase, with the symmetry group of I27a (see Figure 1.3). The monoclinic structure into which metallic phase transforms is a distorted one. The electrical resistivity of the metallic phase is seven orders of magnitude lower than the insulating phase [1]. On the other hand, paramagnetic insulating (PI) phase can be obtained by alloying (e.g. with Cr) [2].

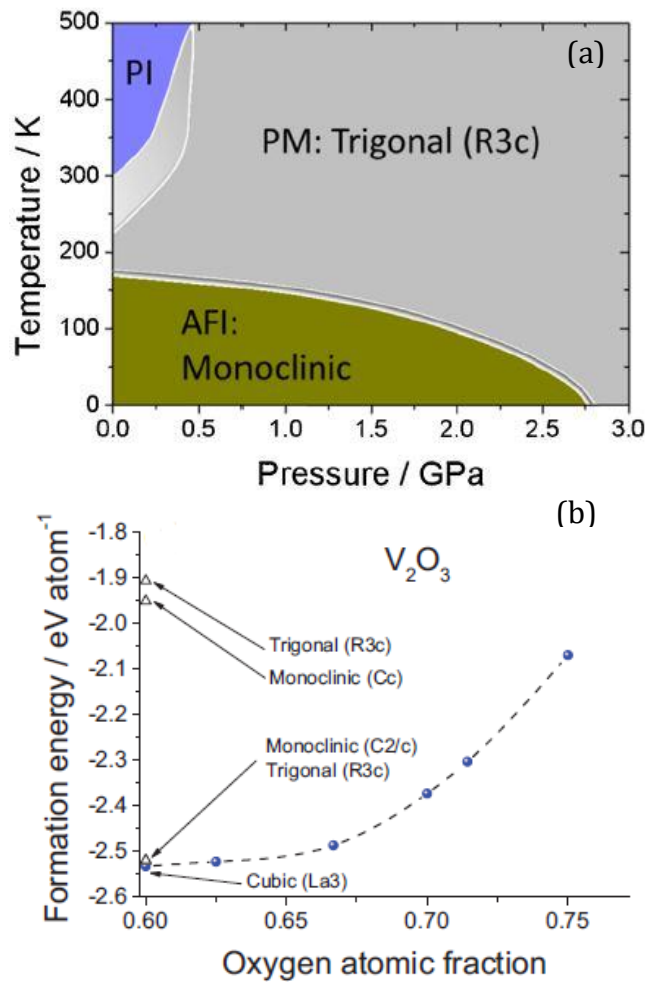


Figure 1.3. Phase diagrams of V_2O_3 showing a) structural transformation under different temperature and applied pressure and b) unstable and metastable structures. PI, PM, and AFI imply paramagnetic insulator, paramagnetic metal and anti-ferromagnetic insulator, respectively [1]

V_3O_5 undergoes a decoupled sharp insulator-to-metal transition at 428K (insulating below 428K). This transition occurs with a change in symmetry group from P2/c to I2/c while the lattice remains as monoclinic. The electrical resistivity decreases more than two orders of magnitude with this transition. In both phases, oxygen atoms built a hexagonal close-packed structure in which 3/5 of the octahedral sites filled with vanadium atoms. With increasing external pressure, the temperature of this transition decreases strongly, as it seen from Figure 1.4a. A transition from anti-ferromagnetic to paramagnetic insulating phase is also seen at 75K upon heating [1].

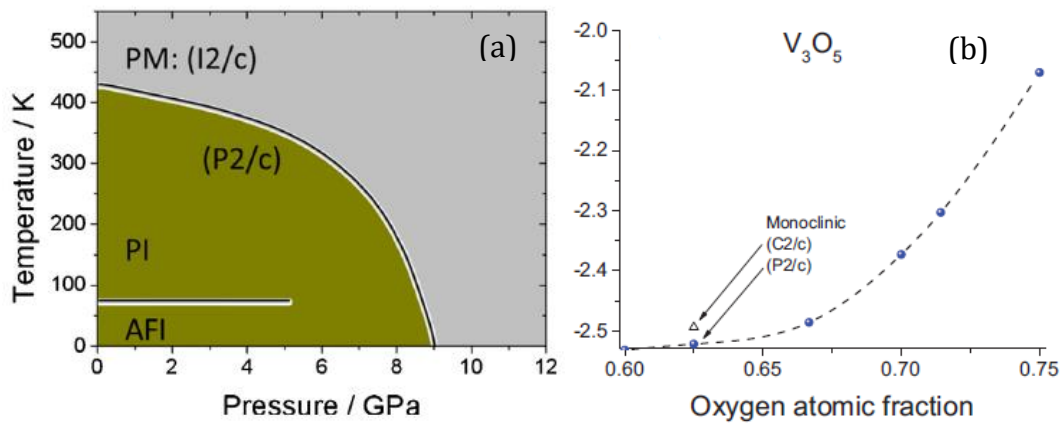


Figure 1.4. Phase diagrams of V_3O_5 showing a) structural transformation under different temperature and applied pressure and b) unstable and metastable structures. PM, PI, AFI imply paramagnetic metal, paramagnetic insulator, anti-ferromagnetic insulator, respectively [1]

VO_2 forms two monoclinic insulating phase and a metallic tetragonal phase through a long temperature and pressure range. The monoclinic phase with crystal symmetry of $P2_1/c$ occurs at temperatures lower than $\sim 340K$ ($68^\circ C$), in the absence of any external pressure (This phase was overlooked in calculated phase diagram in Figure 1.5b). Above this temperature, it transforms into tetragonal phase with $P4_2/mnm$ symmetry. The monoclinic VO_2 with the $C2/m$ symmetry is metastable and can be formed either by doping of VO_2 or under high pressure.

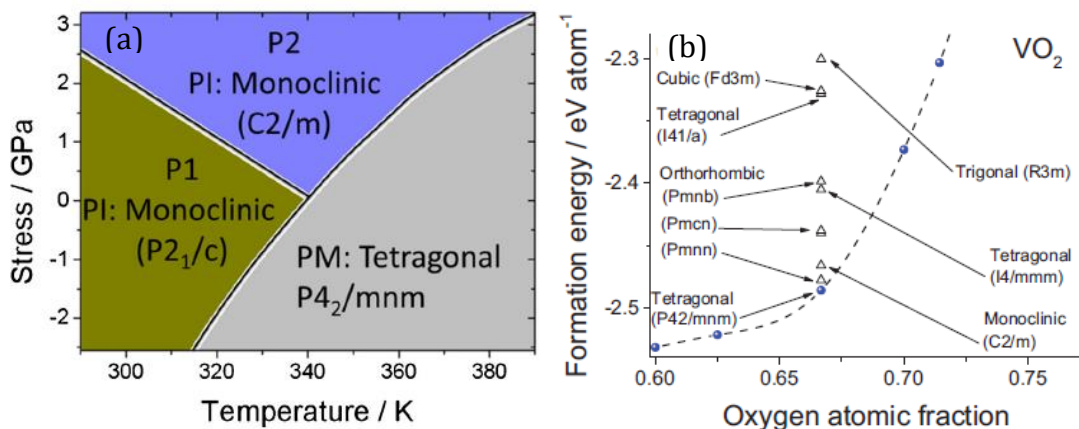


Figure 1.5. Phase diagrams of VO_2 showing a) structural transformation under different temperature and applied pressure and b) unstable and metastable structures. PI and PM imply paramagnetic insulator paramagnetic metal, respectively [1]

The layered oxides of vanadium are frequently encountered in structural analyzes. This group consists of V_2O_5 , V_3O_7 , V_4O_9 and V_6O_{13} compounds which are

also known as Wendsley phases. The metastable monoclinic VO_2 with C2/m symmetry is also included in this family as the last member of the layered oxides. Except for the monovalent phases, the members of this group are composed of mixed valences of +4 and +5.

The most saturated and highly stable layered oxide of the V-O system is V_2O_5 . Therefore, it has a high resistance at room temperature [3]. It can be easily formed as a consequence of natural aging at the high ambient of O_2 . It consists of chains of edge-sharing VO_5 square pyramids and shows insulator to semiconductor (SIT) transition at $\sim 530\text{K}$. Below this temperature, it crystallizes in orthorhombic structure with the Pmmn symmetry (see Figure 1.6.a).

The crystallization of V_3O_7 compound occurs in the monoclinic structure with C2/c symmetry in the temperature range of 4.2-950K. In this structure, it shows electrically insulating character. The lattice consists of VO_5 and VO_6 polyhedra sharing edges or vertexes. The V^{+4} ions occupy octahedral sites assembling in single and double chain whereas other sites are occupied by V^{+5} ions.

The lattice structure of V_4O_9 is a combination of distorted VO_6 octahedra, VO_5 pyramids and VO_4 tetrahedra which share edges and corners. It can be formed by oxygen reduction of V_2O_5 phase [6]; therefore, it provides conductance via oxygen vacancies (positive charge carriers). The literature shows that it can crystallize into two common structure; either orthorhombic with Cmcm symmetry or tetragonal with P42/mnm symmetry [4, 5].

V_6O_{13} is a layered oxide of alternating single and double layers of VO_6 octahedra. The single layers contain V^{+4} cations whereas double layers contain both V^{+4} and V^{+5} cations. V_6O_{13} compound exhibits a phase transition from a high temperature metallic to low-temperature semiconducting phase at 150K. The metallic and semiconductor phases have C2/m and P21/a space group symmetries, respectively. From calculated phase diagram in Figure 1.6.b, crystal structures of above-mentioned compounds can be seen.

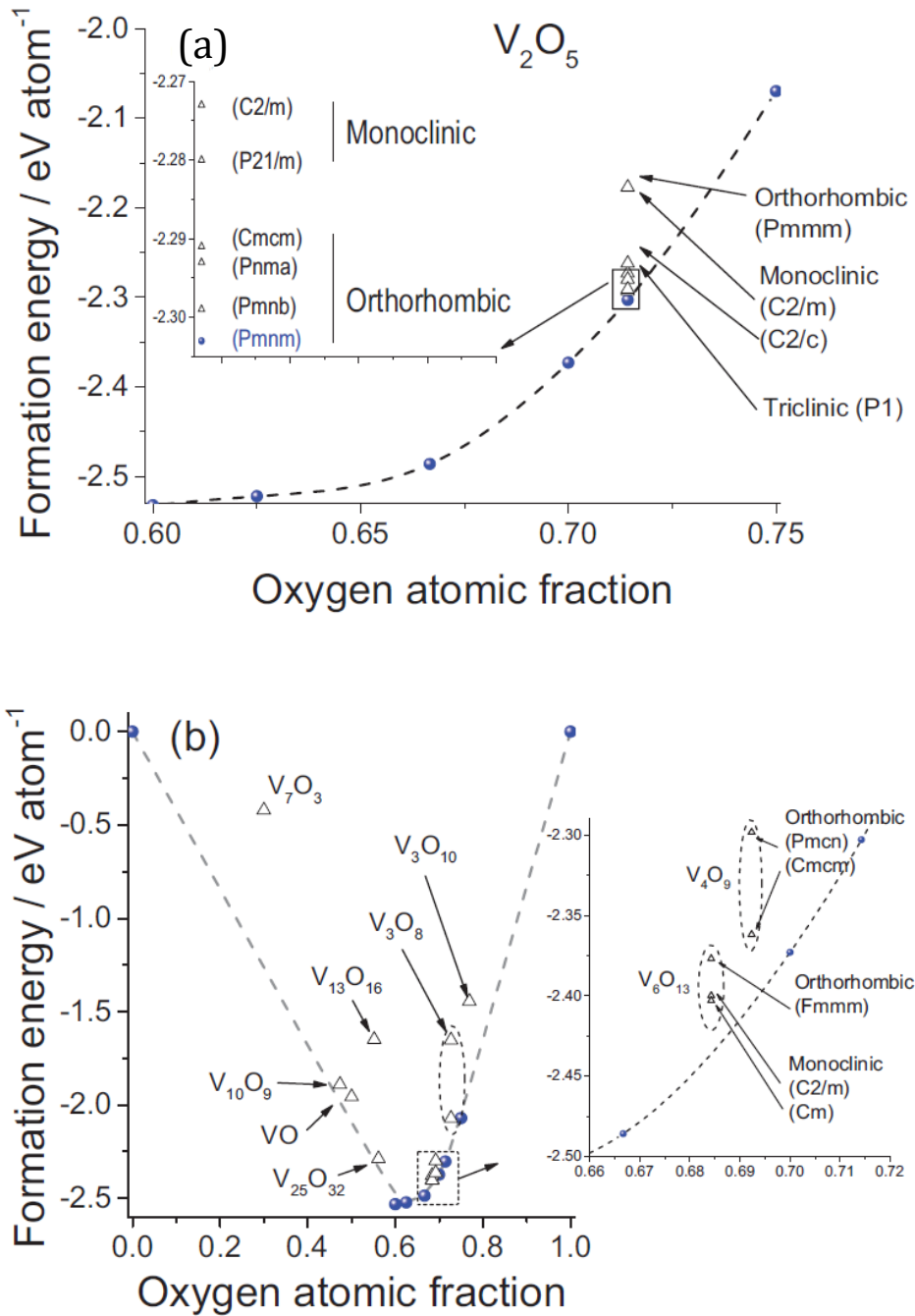


Figure 1.6. Phase diagrams showing a) unstable and metastable structures of V₂O₅ and b) metastable phases [1]

1.3. Electrical Properties of Vanadium Oxide Thin Films Required for Microbolometer Applications

All objects emit infrared (IR) radiation because of the thermal energy they have. The wavelength of the radiation depends on the temperature of the object. This phenomenon is used in IR detectors especially to improve the visibility of an object in the dark environment. IR radiation is situated in the range of 0.75-1000 μm

in the electromagnetic spectrum. However, most of the IR range is absorbed by the molecules such as H₂O and CO₂ in the atmosphere. Therefore, only the wavelength ranges which are allowed by the atmosphere to be transmitted can be used in the application. Most of the IR detectors are designed to detect 8-14 μm wavelength (LWIR, Long way infrared) range while there are also detectors detecting both 3-5 μm and 8-14 μm ranges. These ranges can be observed from Figure 1.7 that shows the typical IR transmittance of the atmosphere. The shaded areas show the selected wavelength ranges (atmospheric windows) in which transmittance of IR radiation is strong. For instance, a black body at 300K emits IR radiation giving the high-intensity peak at 10 μm . IR detectors collect these radiations and convert them into an image based on the temperature difference. IR detectors can be classified into two groups: cooled type photon detectors and uncooled thermal detectors. The cooled detectors require cryogenic cooling systems which raise the cost and weight; this makes them unsuitable for some applications. On the other hand, uncooled thermal detectors can operate at room temperatures and provide wide spectral response [6, 7].

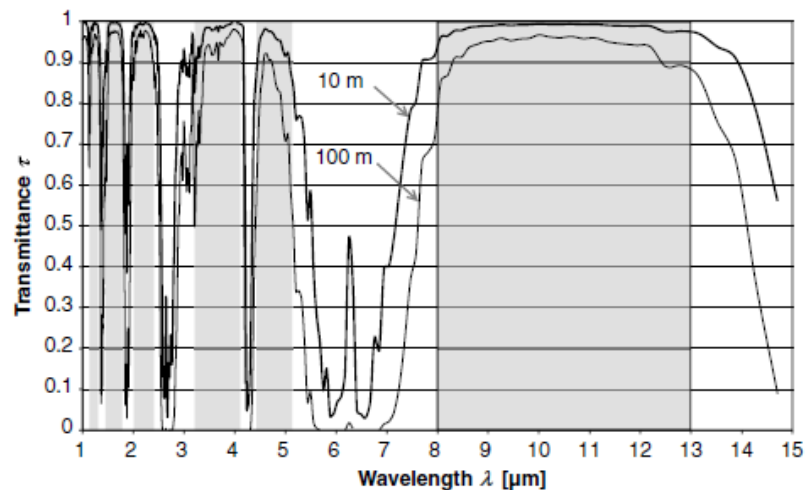


Figure 1.7. IR transmittance of the atmosphere [7]

A microbolometer is an uncooled thermal sensor and thermal detectors are constructed of the arrays of microbolometer sensors (Focal plane arrays, FPAs). Each microbolometer sensor within an array is called pixel. A microbolometer consists of an absorber layer, a sensing layer, a thermal isolation structure, and

underlying read-out integrated circuit (ROIC). The sensing layer is also called the active layer. The general operating principle of a microbolometer is as follows: When the incoming IR beam strikes to the detector, it is absorbed by the absorber layer and transferred into the sensing layer beneath the absorber layer. The IR radiation changes the resistance of the sensing layer. This change in resistance is conveyed by metallic contacts to the ROIC and converted into a measurable signal such as voltage or current. After processing of the signal, it is displayed on a monitor as a thermal image. Thermal isolation is an important issue in the detectors to prevent the dissipation of the perceived IR energy. Microbolometers are commonly fabricated in the suspended structure (or microbridge structure) with a vacuum package to provide thermal isolation [8, 9].

Three figures of merits given in Equation (1.1), (1.2), and (1.3) are commonly used in the evaluation of the performance of a microbolometer. The first one is the thermal time constant (τ). It is defined as the elapsed time during cooling of the sensor which was heated by the incoming IR beam. The responsivity (R_v) is expressed as the output signal (voltage or current signal) of a microbolometer pixel per incident radiation power on the pixel. The detectivity (D^*) give information about signal-to-noise ratio. These figures of merits are expressed as follows

$$\tau = \frac{C}{G} \quad (1.1)$$

$$R_v = \frac{\alpha \eta I_b R_0}{G \sqrt{1 + \tau^2 \omega^2}} \quad (1.2)$$

$$D^* = \frac{R_v \sqrt{A_d \Delta f}}{V_n} \quad (1.3)$$

where G is the thermal conductance, C is thermal capacity, η is IR absorptivity, I_b is applied bias current, R_0 is bolometer resistance at room temperature, ω is modulation frequency, Δf is bandwidth, A_d is effective absorption area and V_n is noise voltage which includes $1/f$ and some other noise components [8].

For semiconductors, the mobile charge carrier density increases with an increase in temperature. Arrhenius-like relation is used in order to define the temperature dependency of resistance in semiconductor materials

$$R(T) = R_0 \times \exp\left(-\frac{\Delta E_a}{k_B T}\right) \quad (1.4)$$

where R_0 , T , k_B , ΔE_a are pre-coefficient, absolute temperature, Boltzmann constant, and thermal activation energy, respectively. The slope of the $\ln R$ -versus- $1000/T$ curve gives $\Delta E_a/k_B$ ratio. Because k_B is a constant, ΔE_a can be calculated readily.

The temperature coefficient of resistance (TCR, α) is an important material parameter. It is a measure of resistance change caused by temperature change. It is calculated by the formula of

$$\alpha(TCR) = \frac{\partial(\ln \rho)}{\partial T} = \frac{\partial(\ln R)}{\partial T} = -\frac{\Delta E_a}{k_B \times T^2} \quad (1.5)$$

where R is the sheet resistance of the material. Therefore TCR can be calculated by obtaining the slope of the $\ln R$ -versus-temperature curve. Improving TCR and resistance is a good way to increase detector responsivity. However, high resistance also gives rise to high noise voltage (V_n) which affect the detectivity.

Particularly in semiconductors through which a current is following, there are voltage fluctuations occurring very frequently at low frequencies. This phenomenon is called 1/f noise, also known as pink and sometimes flicker noise. It is examined by power spectral density (PSD) analysis. For this, voltage spectral noise density is read at a specifically applied current and selected frequency, from a recorded spectrum. The Hooge's formula for voltage spectral noise density is expressed by

$$V_{1/f}^2 = k_{1/f} \frac{I_b^2 R^2}{f^\beta} \Delta f \quad (1.6)$$

where $k_{1/f}$ is 1/f noise factor, I_b is the bias current, R is resistance, f is frequency, Δf is the bandwidth of noise measurement and β is an empirical factor. The 1/f noise factor is frequently used to evaluate the 1/f noise property of a thin film material.

VOx thin films are preferred as sensing layer in microbolometers due to their showing high TCR ($\leq -2\%/K^{-1}$), low resistivity/sheet resistance and low 1/f noise properties.

1.4. Literature Review of 1/f Noise Studies

The sources of 1/f noise are still an open debate in the literature. It is accepted that the combination of both bulk and surface effects creates 1/f noise. The bulk effects include the fluctuations in both carrier concentration and carrier mobilities; arising from carrier trapping-detrapping effects. A surface effect responsible for 1/f noise is believed to be dangling bonds at the material surface. Moreover, non-ohmic contact is another source of the 1/f noise. Some studies in the literature on the investigation of 1/f noise were presented below. These studies can be a guide to evaluate the 1/f noise properties of the produced films within the scope of this thesis.

V. Yu. Zerov et. al. [10] produced the VO_x thin films with various O₂ partial pressures (changing between 10-20%) by reactive magnetron sputtering technique in order to investigate the optimum sputtering conditions. It was determined that 1/f noise level of the films depends on the amount of VO₂ content and grain size; such that noise parameter, K , increases with increasing VO₂ content and grain size. It was suggested that the martensite-like transformation character of VO₂ phase is the reason for the 1/f noise. A. Ahmed and R. N. Tait fabricated 50x50 μm bolometers with an active layer of amorphous a-Ge_xSi_{1-x}O_y of 700 nm thick [11]. The 1/f noise behaviour of the fabricated bolometers was investigated. The 1/f noise factor, $k_{1/f}$, was calculated as 2.9×10^{-11} . At 250 Hz and 4 μA, the 1/f noise value was found as 7×10^{-13} V²/Hz. This value was compared to some other materials used in the bolometer fabrication. It was seen that a-Ge_xSi_{1-x}O_y exhibits higher 1/f noise than VO_x and metals. This higher noise value was attributed to the trapping centers formed by oxygen atoms. The study confirmed that amorphous semiconductor materials show higher 1/f noise compared to crystalline ones. Chi-Anh and Moon evaluated excess noise performance of amorphous V-W-O material as a candidate for bolometric material. They measured the random telegraph signal (RTS) noise and 1/f noise. While no RTS noise was found in the films, the 1/f noise level calculated as 4×10^{-15} V²/Hz at 20 Hz with a bias current of 5.4 μA. The 1/f noise factor was calculated as 6×10^{-12} . The material 1/f noise comparison showed that 1/f noise value of V-W-O is lower than the other materials except VO_x [12]. The 1/f noise was investigated at different temperatures (293-310K) in the frequency range of 10-

100 Hz. It was observed that 1/f noise decreases with the increasing temperature. This behaviour was ascribed to the reduction of material resistivity at high temperatures. In another study, Hojun Ryu et. al. studied the sputtered silicon antimony film for microbolometer application and compared its 1/f noise property to the plasma enhanced chemical vapour deposited (PECVD) amorphous silicon film. The structural investigation of the silicon antimony film showed that the film consists of the finely formed crystals with the crystal sizes lower than 20 nm. The PSD-versus -frequency plots demonstrated that the sputtered silicon antimony film shows lower noise value than PECVD deposited silicon. This result related to the nano-sized crystalline structure of the silicon antimony film which distributed evenly in the film matrix. The films' 1/f factor, K , was calculated between 0.4-224.9x10⁻¹⁰ [13]. Another material that can be a candidate for bolometric applications is nickel oxide thin film. In one study, 60 nm thick films were produced by DC sputtering method and annealed at 320°C for different durations. The films annealed for 7.5 hours showed an electrical resistance value of 10 MΩ. These films showed a TCR value exceeding -3.22%/°C and suitable noise with the 1/f noise factor of 3.5x10⁻¹² [14].

One other candidate for the application is the mixed phase VO_x films. In one study, the mixed phase VO_x (1.3≤x≤2) thin films were fabricated by PDC-RMS with radio frequency (RF) substrate bias; and showed superior electrical and 1/f noise properties [15]. The structural characterization indicated that the films consist of the nanocrystalline columnar microstructure; with nanotwins embedded in amorphous VO_x matrix. The spectral current density-versus-frequency plot of the films, produced with and without substrate bias, showed that the biased nanotwinned VO_x sample exhibit ~6 orders smaller 1/f noise (1/f noise factor was estimated between 5x10⁻¹² and 5x10⁻¹⁵) compared to the unbiased nanocrystalline VO_x sample. In addition, it was found that the biased films ≥800Å exhibit lower normalized Hooge parameter in comparison to biased films ≤800Å [15].

Rui Xu and his colleagues deposited the boron-doped nanocrystalline Si_{0.78}Ge_{0.22}:H films by PECVD method diluted with argon and at a substrate temperature of 230°C. As a result, the partially crystallized films were obtained with grain sizes changing between 15-30 nm. The 1/f noise factor was calculated by

fitting the PSD curve according to Hoog's formula as 7×10^{-14} . This value is lower than those of the traditional nanocrystalline Si, a-SiGe and a-SiGeO thin films. It is believed that this low $1/f$ noise level arises from the nanostructures involved in the amorphous structure which cause hydrogen variation and defect reduction [16]. Young Bong Shin et. al. deposited the Nb-doped TiO_{2-x} films by RF reactive magnetron sputtering technique at different O_2 partial pressures. Above 4.3% O_2 partial pressure, the films occurred in an amorphous structure. It was shown that the resistivity of the films was increased with the increasing O_2 partial pressure due to the reduction in oxygen vacancies. The Nb doping resulted in lower resistivity in comparison to pure TiO_{2-x} films. Moreover, the variation in resistivity is more controllable via Nb doping. The $1/f$ noise parameter-versus-resistivity plot of both pure and Nb-doped TiO_{2-x} revealed the dependency of $1/f$ noise on resistivity such that $1/f$ noise decreases by decreasing resistivity [17]. Al-doped ZnO (AZO) thin films prepared at different deposition temperatures (200°C, 300°C and 400°C) with DC sputtering on glass substrates by Barhoumi et. al. As a measure of the film inhomogeneity for the noise source relative to gold homogeneous films, $[\alpha\mu]_{\text{eff}}/[\alpha\mu]_{\text{Au}}$ ratio was considered. This ratio revealed the poorer crystallinity and higher $1/f$ noise of the AZO thin films compared to Au films. Furthermore, decreasing of $[\alpha\mu]_{\text{eff}}$ with the temperature indicated the improvement of homogeneity of the AZO thin films. The structural characterization of the AZO thin films showed the decrease of the grain boundaries and the increase of crystallinity with rising substrate temperature. As a result, lower $1/f$ noise value was obtained [18].

1.5. Thin Film Production: Pulsed DC Reactive Magnetron Sputtering

In previous investigations, various techniques such as pulsed laser deposition [19], ion beam sputtering [8], sol-gel method [20], electron beam evaporation [21], and spray pyrolysis [22] were used to deposit VO_x thin films. Compared to other techniques, magnetron sputtering provides advantages on the controlling of film thickness, the compact and homogeneous film deposition, the rate of deposition and film the adhesion to the substrate. As a combined technique, PDC-RMS is also used extensively in the production of mixed phase VO_x thin films. This technique requires

precise control of the process parameters (ratio of process gases, total gas pressure, DC power, deposition rate, substrate temperature, pulse frequency, and width etc.).

In a recent study, three methods are summarized to produce desired phase transition in VO_x films [23]: The first method is direct deposition of the films by selecting proper sputtering parameters. The second method is a reduction method. In this method, a V₂O₅ film having a high oxidation state is deposited at the beginning. Afterwards, this film is annealed under a reducing atmosphere such as N₂, Ar or in vacuum to reduce V₂O₅ to VO₂ phase. In the third method, vanadium or VO_x film with low oxygen fraction is grown under a high vacuum atmosphere, and generally at room temperature; then, a post-annealing procedure is applied under an O₂ ambient. These methods are also instructive for the production of mixed phase VO_x thin films. However, the first method is the hardest way to obtain the desired film properties. In the majority of the studies in the literature, heat treatments are also applied to the magnetron sputtered films at the time of and/or after deposition to obtain suitable films. It is reported that the heat treatment processes must be lower than 400°C to be compatible with complementary metal oxide semiconductor (CMOS) circuits.

As a deposition method, sputtering defines a physical phenomenon in which surface of a target material is bombarded with energetic ions resulting in the ejection of the surface atoms. The ejected atoms, then, condense on a substrate material by crossing a low-pressure environment to form a film. Applying a sufficiently high DC voltage between two electrodes, grounded anode and a negatively charged cathode which are immersed into a low pressure gas ambient, initiates a gas discharge. Analogous to dielectric breakdown in insulating materials, a gas discharge occurs as a result of the electrical breakdown of the gas medium. After the breakdown, a discharge current begins to flow; therefore, electrically insulating gas becomes a conducting medium which is also known as plasma [24].

The sputtering process begins when a stray electron is accelerated toward anode under the applied electrical field. The electron gains a kinetic energy and collides with a molecule of working gas and convert it into a positively charged ion; typically, argon is used as working gas in the process. After this collision, an

additional electron is produced, besides the positive gas ion. Equation (1.7) below shows this interaction.



The resulting two electrons are also driven toward the anode and cause more neutral gas atoms to ionize. Conversely, the positive gas ions are accelerated toward the cathode; strike the target material there, and cause the target atoms and secondary electrons to be scattered into the gas atmosphere. The secondary electrons also experience collisions with neutral gas atoms. This event continues in this way until a sufficiently high current flows and causes the gas to breakdown [24].

Up to this point, sputtering mechanism was defined via simple DC sputtering. In simple DC sputtering, at low pressures, the mean free path between collisions are large and ionization efficiency is low. Therefore, plasma can not be sustained at pressures lower than ~ 10 mTorr. The efficiency can be increased at higher pressures. However, because excessive collisions will occur at very high pressures, most of the sputtered atoms can not reach to substrate to deposit on. Thus, there is an optimum range of operation pressure (see Figure 1.8) at which sputtered atoms deposit efficiently while plasma is self-sustaining [24].

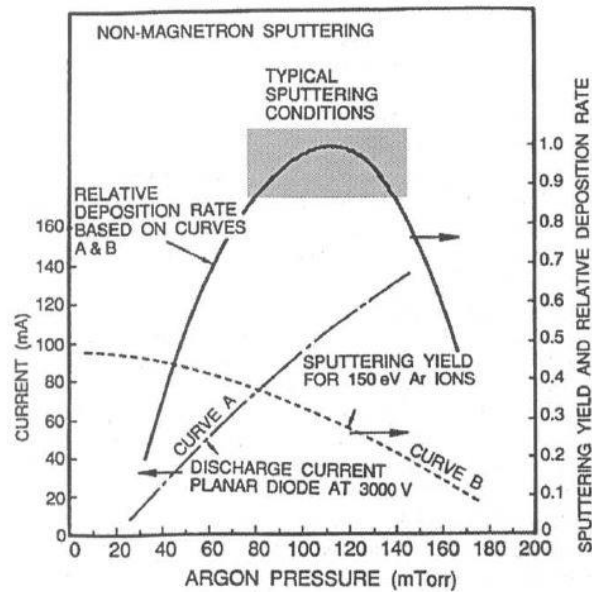


Figure 1.8. Effect of working pressure and current on film deposition rate in simple DC sputtering [24]

Even at low operating pressures, sputtered atoms from the target material undergo many scattering events. Hence, deposition rates are very low; such as a few hundred Å per minute for many metals. Increasing the gas pressure to the higher levels will not be a solution to the low rates because the increased contamination levels of O₂ and H₂O will lead to oxidation of the target material. This contamination on the target will additionally reduce the deposition rate [24, 25]. In summary, simple DC sputtering is problematic in some ways: plasma is not self-sustained at low pressures, scattering and contamination events give rise to low deposition rate, and modification of the deposited film structure is not controllable. Fortunately, these problems can be overcome by using magnetron sputtering technique. In fact, usage of magnetron technique in combination with DC sputtering is very common. In magnetron sputtering, the electrons, which ionize neutral gas atoms, are restricted to a narrow region nearby the cathode. By this way, gas ionization efficiency is increased without allowing electrons to disperse around the chamber. Therefore, the sputtering operation can be realized at lower pressures (typically a few mTorr), which prevent high degree scattering and contamination levels. Moreover, higher deposition rates (~1µm/minute for Al metalization alloys) or alternatively low voltage operations can be realized [24].

Thin films of semiconductor and insulating materials, e.g., oxides, nitrides are intensively studied for various applications. Targets of these materials in varying compositions are commercially available to deposit thin films with desired stoichiometries. However, film deposition from an insulating target is not possible via DC technique. This is because positive charge accumulation occurs at the surface of insulator targets that repels incident positive gas ions; therefore, the plasma shuts down, and sputtering operation can not be realized. By using RF sputtering technique, thin films can be directly deposited from insulating targets [24, 26]

An alternative to RF sputtering, DC reactive magnetron sputtering is very popular to produce semiconductor and insulating films from metallic targets. In this technique, a reactive gas, e.g., O₂ is introduced into the process chamber along with the working gas. After the reaction between the sputtered metal and the reactive gas atoms, the resulting compound condenses on the substrate. DC reactive magnetron sputtering is preferred because of its strengths: (i) It allows to control film

stoichiometries at high deposition rates. (ii) Elemental targets are easier to be purified to obtain high purity films. (iii) Elemental targets are conductive and so can be cooled more effectively, thus, a wide range voltages can be applied without avoiding cracking problems caused by thermal issues. (iv) Complexity and expense of RF sputtering can be avoided by using DC power supply.

Besides its strengths, undesirable effects also can be seen in DC reactive magnetron sputtering technique. The differential target poisoning with accompanying hysteresis effect is one of the well-known [25]. Target poisoning is the formation of an insulating layer on the target surface as a result of interaction between the reactive gas and target material. This formation causes the deposition rate to decrease and the film to grow as gas-rich (a change in film stoichiometry).

Figure 1.9 shows the hysteresis behaviour of system pressure. The dotted line in the figure represents the change in system pressure with changing working gas flow. In this case, the correlation between gas flow rate and system pressure is obviously linear. This is the situation for metallic film deposition. The hysteretic behaviour is observed along with the control of reactive gas flow in the system pressure for compound deposition. At low values of reactive gas flow, $Q_r(0)$, almost all reactive gas is consumed by the sputtered metal atoms. Therefore, there will be no essential change in the system pressure. After reaching a critical value of reactive gas flow, Q_r^* , a jump in the system pressure is observed. At this value, the amount of the reactive gas, pumped into the system, is higher than the consumed by metal atoms. This is a result of the oxide layer formed on the target surface at such high gas flow rates. In this case, metal atoms can not be sputtered from the target to react with the gas atoms. Thus, an increase occurs in the system pressure. If the flow rate is reduced again to control the system pressure, the trajectory followed by the system pressure will not be the same. This is because the gas pressure remains high until the oxide layer is removed by Ar ions and the sputtering of the metal target is achieved again. Two stable states are observed at the hysteresis plot. These are shown by A and B in Figure 1.9. In state A, metal-rich films are deposited whereas for state B the films are gas-rich or compound. The hysteresis effect shows itself at the cathode voltage and deposition rate as well (see Figure 1.10). Since more ion-induced secondary electrons are emitted when the oxide layer is sputtered, the

plasma current increases and the cathode voltage drops. In addition, the sputtering from a compound target is much slower than the sputtering from a metallic target. Therefore, decrease in the voltage and the deposition rate is seen by increasing the gas flow rate [24, 25].

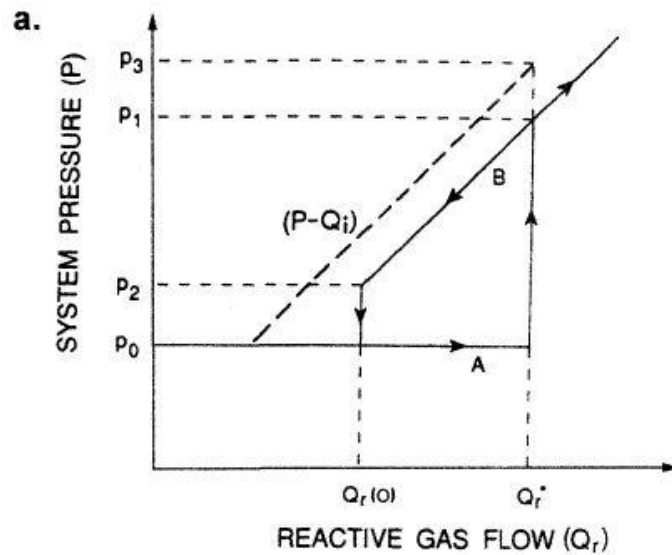


Figure 1.9. Hysteresis behaviour of the system pressure with changing the reactive gas flow rate. The dotted line shows the pressure change when working gas flow rate is changed [24]

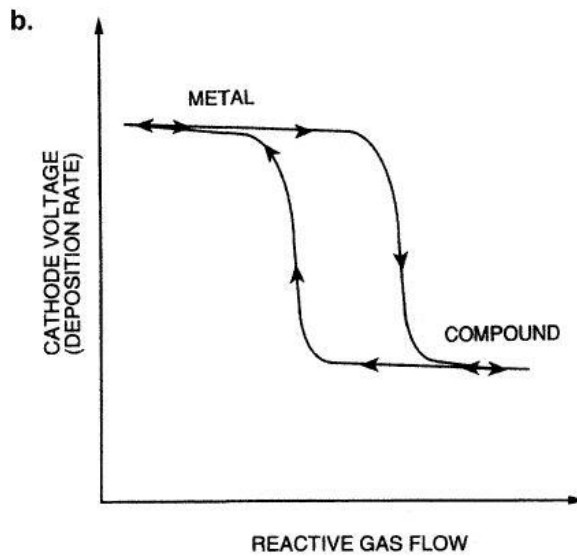


Figure 1.10. Hysteresis behaviour on cathode voltage and deposition rate with changing reactive gas flow rate at a constant current [24]

There are various methods for solving the hysteresis problem: increasing the pumping speed, increasing the target to substrate distance, obstructing reactive gas flow to the cathode and using pulsed DC power supply [25]. All these solutions also bring some difficulties with them. In our case, pulsed DC technique was used to overcome this problem.

At a typical sputtering voltage of -400 V, positive Ar ions are attracted by the cathode, and sputtering of metallic target occurs. When an insulating layer is formed on the surface of the target, low energy ions are built upon the insulating layer surface. This causes the formation of a parasitic capacitor. As the voltage of the capacitor climbs, Ar ions can not strike the surface with sufficient energy. Moreover, the ions can be totally repelled when more charge builds up. Reversing cathode voltage suddenly to a positive value, e.g., +100 V, for a short time, causes the insulator surface to be charged with -100 V. This occurs because electrons are attracted in the presence of positive voltage and accumulate on the insulator surface. After this short period of reversing voltage, the cathode voltage is brought back to actual sputtering voltage (-400 V). Because the negative potential of the surface (-100V) is summed up with the applied voltage (-400), Ar ions are accelerated under -500 V and strike to insulating layer with more energy. Consequently, the insulating layer is sputtered off the target [27].

1.6. Aim of the Study

VO_x thin films are used in many technological applications due to their remarkable physical and chemical properties. Some of these applications are smart windows [28, 29], memory devices [30], uncooled infrared (IR) detectors [21, 31, 32], gas sensors [33, 34], smart radiator device for spacecraft [35], and energy storage systems [22, 36]. The reason for VO_x thin films to be preferred in uncooled microbolometers is that they can meet the requirements such as high TCR ($\geq 2\%K^{-1}$) at room temperature, suitable sheet resistance or resistivity, relatively low 1/f noise and compatibility to CMOS ROIC at low process temperatures [8, 15, 37, 38]. However, in order to meet these requirements, the films must be grown in proper film structures.

Vanadium has various valence states and forms a number of oxide phases with oxygen due to its half-filled d shell. The principal oxides (VO, V₂O₃, VO₂, and V₂O₅) have a single valence (+2, +3, +4, +5, respectively) in their oxidation states. Vanadium–oxygen phase diagram (see Figure 1.1) also includes mixed valence oxides, such as V₆O₁₃, V₃O₇, V₄O₉, and V₇O₁₃ [1]. Among these oxides, VO₂ is desirable in uncooled microbolometers due to its high TCR value [9]. However, low metal-insulator transition (MIT) temperature at ~67°C of VO₂ limits the IR detection range. On the other hand, V₂O₅ is the most saturated phase and has high stability. It can be easily formed on the film surface as a consequence of surface oxidation in the presence of enough oxygen in the environment. It also shows high TCR value, but its high resistance gives rise to high 1/f noise [39, 40]. V₂O₃ has low formation energy and undergoes a transition from semiconductor to metal phase at ~-123°C, so its resistance is very low at room temperature. Because the high electrical resistance of a device results in a high level of noise, the use of V₂O₃ phase is important for the fabrication of low-noise microbolometers [8, 41]. Another low resistance phase is V₆O₁₃. It shows metallic character at room temperature [3]. V₄O₉ provides high TCR and low resistivity as well [4]. As a consequence, various VO_x phases can meet different requirements for the application. For this reason, mixed phase VO_x thin films are extensively studied.

Pulsed DC reactive magnetron sputtering technique is one of the most common technique studied in the literature to fabricate VO_x thin films [15, 42, 43]. Precise control of process parameters (e.g., reactive gas ratio, deposition power, deposition time, substrate temperature etc.) is required to obtain desired film properties by this technique. In general, VO_x thin films produced by sputtering methods are exposed to annealing processes at different temperatures and atmospheres during and/or after deposition, in the literature [32, 44].

In previous studies completed in our research group, optimization of process parameters of VO_x film deposition and post-annealing were accomplished. After optimization of film deposition process, a thin film sample with a sheet resistance of ~720 kΩ/sq was produced in as-deposited film condition (see Table 1.1) The film with this sheet resistance was deposited on a wafer covered with finger-structure electrodes. Prior to deposition, the electrodes were formed by lithography methods

on the wafer; with different finger surface areas (W) and distances between fingers (L). By adjusting these parameters of finger structures, it is possible to reduce the resistance of a deposited film by about 10 times. Consequently, 100 nm thick VOx thin films with sheet resistances ranging between 30 and 200 k Ω could be obtained in as-deposited film condition. Afterwards, optimization of the post-annealing process was performed in order to reduce 1/f noise values of the films below 10 kHz in the as-deposited state. For this aim, the films were annealed at 200°C and 300°C in an N₂ atmosphere for 3 (three) hours. The noise value of 200°C annealed film was found to be under 10kHz while the film at 300°C showed 1/f noise value above 40kHz (see Table 1.2). As a result, post-annealing at 200°C in the N₂ atmosphere for 3 hours gave the lowest noise value (unpublished master of science thesis, Ahmet Murat Yağcı, 2015 [45]).

Those changes in electrical properties observed throughout different film conditions appeared as an attractive phenomenon. Table 1.2 presents the electrical results of the films, which were deposited on finger-structure electrodes, from the previous study [45]. In addition, although suitable electrical properties were obtained for the application, the relation of these properties to structural properties was not established within the scope of the study. Therefore, the aim of the study in this thesis was to investigate the correlation between electrical –particularly 1/f noise– and structural properties of the nanoscale VOx thin films.

Table 1.1. Sheet resistance and resistivity results of the as-deposited film deposited on the bare Si₃N₄/SiO₂/Si substrate from the previous study [45]

Sample name	Sheet resistance (k Ω /sq)	Resistivity (Ohm.cm)	Ar/O ₂ gas flow ratio	Film thickness (nm)
# 55-1	720.6±0.35	7.2±0.1	2/0.4	100

Table 1.2. Electrical results of the VOx thin films deposited on finger-structure electrodes [45]

Sample	Resistance (k Ω)	TCR (%/°C)	f _c (kHz) @10 μ A	noise@30Hz (V ² /Hz)
As-deposited	60	-2.63	> 40 kHz	2.2x10 ⁻¹²
Post annealed - 3 hours@200°C	90	-2.73	8 kHz	2.2x10 ⁻¹³
Post annealed - 3 hours @300°C	206	-3.47	> 40 kHz	4.9x10 ⁻¹¹

For the study in this thesis, VO_x thin films were deposited by using PDC-RMS technique with the optimized process parameters in order to investigate structure-property correlation, especially relationship between electrical noise and nanostructure. Some of the films annealed at 200°C and 300°C in the N₂ atmosphere for 3 hours. Electrical characterization of the films performed by four-point probe (FPP) system. In order to obtain complementary results, several techniques were used for structural characterization Grazing-Incidence X-Ray diffraction (GIXRD), X-Ray photoelectron spectroscopy (XPS), Raman spectroscopy, transmission electron microscopy techniques (TEM), Selected area electron diffraction (SAED), and electron spectroscopic imaging (ESI).

2. MATERIALS AND METHODS

2.1. Fabrication of Thin Film Sample

2.1.1. Substrate preparation

In microbolometer fabrication, silicon nitride is used as supporting layer which provides thermal isolation. Its heat capacity and thermal conductivity values are 700 J/kg.K and 0.3 W/m.K, respectively. VO_x thin films which act as a thermal sensing layer are grown on this layer. Moreover, VO_x thin films crystallize well on silicon nitride [8, 46].

In this study, thin films were deposited on square shaped Si₃N₄/SiO₂/Si substrates which are 10x10 mm² in size. The substrates were cut from an 3-inch Si₃N₄/SiO₂/Si wafer. The wafer consists of a 1µm-thick SiO₂ layer on the top which is formed by thermal oxide coating on Si (100). Silicon nitride (Si₃N₄) layer, then, is deposited on wafers with a thickness of approximately 250 nm by using PECVD. Before deposition, the substrates were exposed to a cleaning procedure. For this purpose, the substrates were passed through acetone, propanol and deionized water, and then blow-dried with high purity N₂. After cleaning procedure, the substrates were placed into a sample holder as shown in Figure 2.1.

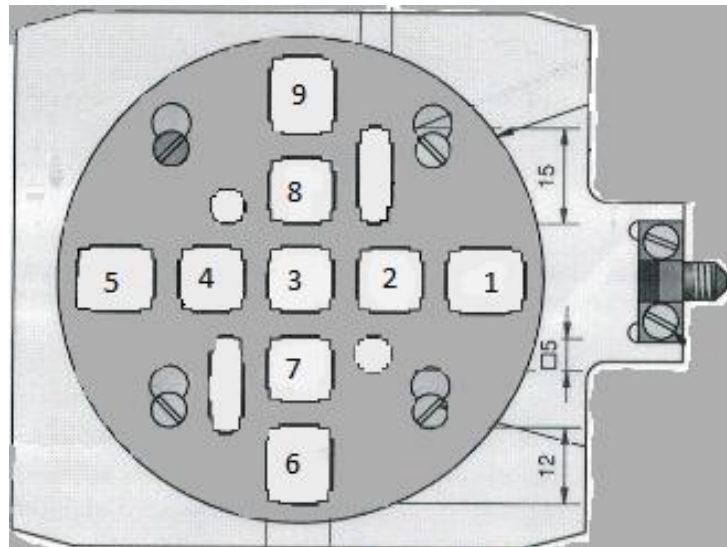


Figure 2.1. Sample holder showing the position of the samples

2.1.2. Thin film deposition

The deposition of VO_x thin films was realized by PDC-RMS (Bestec UHV-Sputter System, Visual 2.1) located at the advanced technology thin film laboratory of Material Science and Engineering Department of Anadolu University. The sputtering system is a design of Prof. Dr. Ramis Mustafa Öksüzoğlu. There are four vacuum chambers in the system: two process chambers (sputter1 and sputter2, which are approximately 100 liters and 80 liters in volume) and one annealing chamber arranged around a load-lock. The chambers are isolated from each other by electro-pneumatic actuated valves. Sample transfer is ensured by magnetic transfer rods from the load lock chamber to the sample station in the process chamber. During the sample transfer, the valves are opened with the help of software control. The chambers are evacuated into high vacuum levels by turbomolecular pumps which are also backed up with scroll type mechanical pumps. The scroll pumps, firstly, pump the chambers down to a rough vacuum level ($\sim 10^{-3}$ mTorr). The further ultra-high vacuum levels are achieved by turbomolecular pumps. All chambers are equipped with a full range gauge for pressure measurement from atmosphere-pressure to 5×10^{-9} mbar. The base pressure is measured by full range gauges whereas the baratron gauges measure the pressure at the time of the process. Each process chamber contains magnetron sources at the bottom of them, to which target materials are situated. The sample holder station is mounted on the manipulator top flange. It can be rotated with a motor driven. The distance between sources and the sample holder can be adjusted by moving the manipulator vertically. Also, the sources can be brought into a position inclined to the sample station by tilting them. The process chambers have gas inlets with mass flow controllers; the process gases are fed into the chambers by these inlets. All components of the system are controlled by the software of the system.



Visual 2.1. *Bestec Ultra High Vacuum Sputter System present at Advanced Technology Thin Film Laboratory of Anadolu University*

During thin film deposition, the impurity atoms from walls and components of the process chamber are also ejected. These impurities can be introduced into the deposited film and affect the quality. Moreover, foreign gases such as H₂, CO₂, N₂ and water vapour must be thrown out of the chamber to have a clean atmosphere and to reach optimal base pressures at $\sim 10^{-8}$ mbar and below. Therefore, in order to obtain high-quality films, system components must be cleaned periodically, and also subsequent bake-out procedure must be applied. Within this respect, before thin film deposition, the system components were sanded with Dremel brand flapwheels; and then passed through an ultrasonic ethanol bath. Afterwards, the system was baked out at 110°C for 48 hours to get rid of foreign gases and water vapour inside the chamber.

After cleaning and bake-out procedure, the sample holder, which carries substrates on it, was loaded into the load lock chamber and transferred into the process chamber. Metallic vanadium target (Kurt J. Lasker, 99.5% pure) was used for the deposition. DC power was set at 70 Watt (318 V - 220mA). The process chamber was pumped down to a base pressure of 1.2×10^{-8} Torr. Prior to reactive deposition, the surface of the target was pre-cleaned for 15 minutes via bombarding by Ar⁺ ions

to remove the oxide layer. After the pre-cleaning process, the chamber was vacuumed again to throw the sputtered oxide particles out of the ambient. As the processing gases, 2 sccm Ar (99.9999% purity) and 0.4 sccm O₂ (99.9999% purity) were continuously fed into the chamber during the deposition; the gas flow into the chamber was controlled by MKS 647 gas inlet controller.

2.1.3. Post-annealing process

In the previous work performed by our group, the post-annealing optimization of the VO_x thin films was performed in METU-MEMS center in order to use annealing ovens compatible with CMOS production and to test integrability of the films into the CMOS process. For this aim, the films were annealed at 200°C and 300°C for 3 hours in a high purity N₂ (99.995%) atmosphere. The best electrical results were obtained by annealing at 200°C. For optimizing the annealing time, the films were annealed from 1 to 3 hours at 200°C. The annealing for 3 hours gave the best results. In this annealing optimization process, the resulting change in the electrical properties of the films observed by annealing at 200°C and 300°C for 3 hours was decided to investigate. Therefore, the samples prepared within the scope of this study were also annealed at 200°C and 300°C for 3 hours under high purity N₂ atmosphere. Three groups of thin film samples were obtained at the end of the fabrication process: the as-deposited films and the films annealed at 200°C and 300°C for 3 hours under high purity N₂ atmosphere. Table 2.1 shows production parameters of all films produced in this study.

Table 2.1. Production parameters of the deposited VO_x thin film samples

Sample	Post-annealing condition	Ar/O ₂ flow ratio	Substrate	Film thickness
VO _x -1	as-deposited	2/0.4	Si ₃ N ₄ /SiO ₂ /Si	100
VO _x -5	as-deposited	2/0.4	Si ₃ N ₄ /SiO ₂ /Si	100
VO _x -6	as-deposited	2/0.4	Si ₃ N ₄ /SiO ₂ /Si	100
VO _x -2	200°C	2/0.4	Si ₃ N ₄ /SiO ₂ /Si	100
VO _x -3	200°C	2/0.4	Si ₃ N ₄ /SiO ₂ /Si	100
VO _x -4	200°C	2/0.4	Si ₃ N ₄ /SiO ₂ /Si	100
VO _x -7	300°C	2/0.4	Si ₃ N ₄ /SiO ₂ /Si	100
VO _x -8	300°C	2/0.4	Si ₃ N ₄ /SiO ₂ /Si	100
VO _x -9	300°C	2/0.4	Si ₃ N ₄ /SiO ₂ /Si	100

2.2. Thin Film Characterization

2.2.1. Electrical characterization

2.2.1.1. Four-Point probe technique

FPP technique is commonly used to measure electrical resistivity or sheet resistance and for the calculation of TCR of semiconducting thin film samples. The TCR measurement is performed by heating the sample via an integrated heating stage and recording the voltage changes for calculation of the resistance. The benefit of FPP technique can be better understood when compared with two-point probe system. Rather than using the two-probe configuration, the four-probe configuration provides elimination of parasitic voltage drops. In a two-point probe system, the current is sourced and the voltage is read through the same probes. Because the path of the voltmeter contains the contact, the probe, and the wire resistances, the voltage drops from these elements are also measured. Figure 2.2 comparatively represents the circuit schemes of two-point probe and FPP techniques [47].

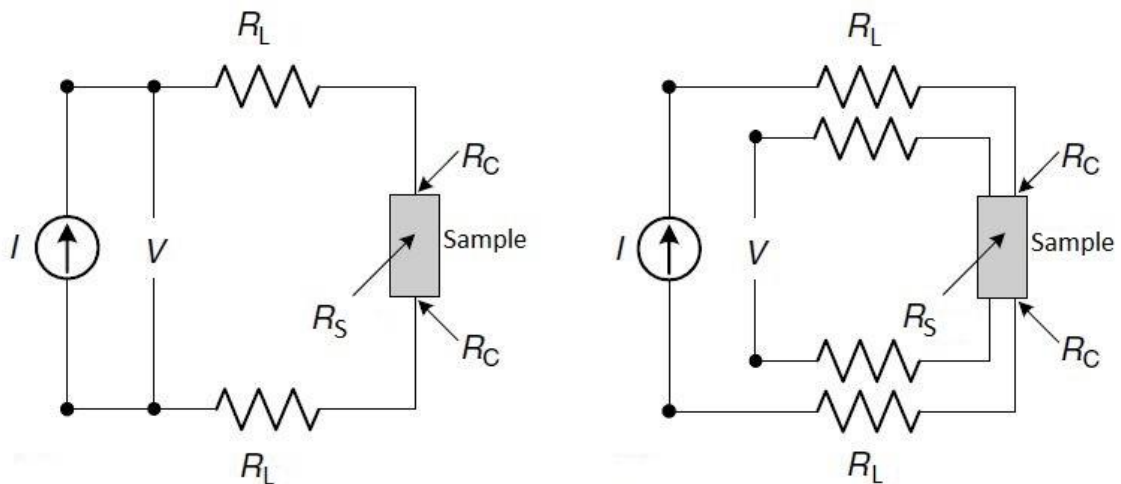


Figure 2.2. Comparison of circuit schemes of two-point and four-point configurations [47]

According to the figure, the total resistance measured by a two point probe system is given by

$$R_T = \frac{V}{I} = 2R_L + R_C + R_S \quad (2.1)$$

here, R_L , R_C and R_S are the wire-probe resistance, the contact resistance and the resistance of the sample under test, respectively. Obviously, it is not easy to measure R_S with two-probe configuration because of the contributions from R_L and R_C . On the other hand, although the four-probe configuration still has R_L , R_C on the voltage path, the current passing through the voltmeter is very small because the voltmeter has a high input impedance ($\sim 10^{12} \Omega$ or higher). Therefore, it is assumed that the voltage drop is only caused by resistance of the sample, R_S .

The advantages of FPP system are being fast and not requiring a calibration step for each measurement. Besides, it is commercially available and inexpensive. As a weakness of the system, probes can cause deformation on the surface of the sample. Eventhough the degree of the deformation is not severe, it can reduce the reliability of the measurement. In order to decrease the degree of deformation, the probes are made of springs.

In FPP technique, a direct current is sourced by outer two probes while inner two probes are used to measure the voltage drop occurring across the sample (see Figure 2.3) The resistivity measurement depends on the arrangement of the probes on the sample and geometry of the sample. For the reliability of the test, these factors should be taken into consideration. Typically, the four probes are equally spaced and aligned along a straight line (equally spaced in-line 4P) [48]. In the case of a 3D semi-infinite sample, the current spreads spherically into the sample and the resistivity is calculated by

$$\rho_{3D}^{line} = 2\pi s \frac{V}{I} \quad (2.2)$$

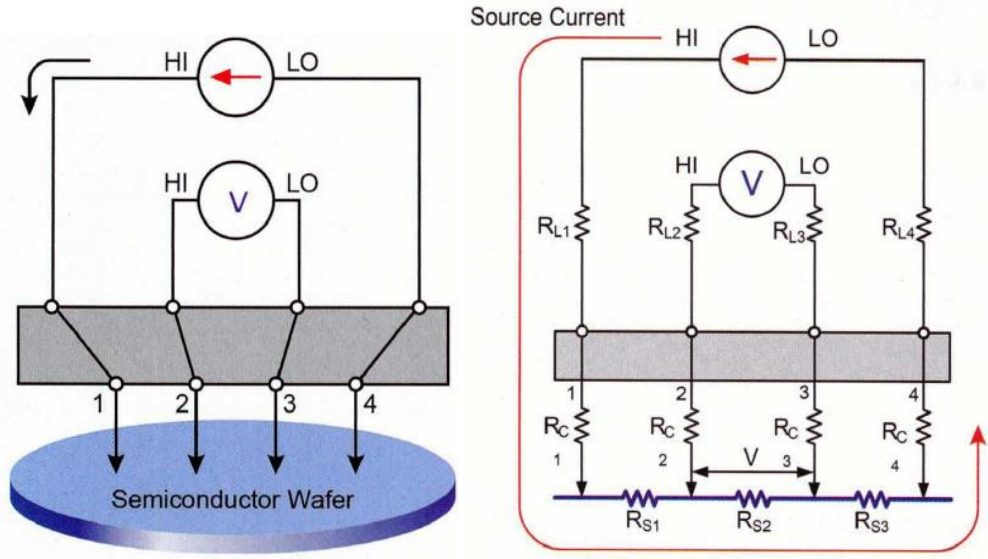


Figure 2.3. Illustration of electrical measurement with FPP [49]

where V is the voltage measured, I is the current forced and s is the probe spacing. When the sample thickness, t , is finite and very small compared to probe spacing ($t \ll s$), then the material turns into a 2D infinite sheet. In this case, the current spreads cylindrically into the material, rather than spherically. With equally spaced in-line four-probe configuration, the resistivity is given by

$$\rho_{2D}^{line} = \frac{\pi t V}{\ln 2 I} \quad (2.3)$$

As a character of 2D materials, resistivity is not dependent on the probe spacing. Here, a new term which is frequently used appears: It is called sheet resistance or surface resistivity and expressed by

$$R_{Sh} = \frac{\rho}{t} = \frac{\pi V}{\ln 2 I} [\text{ohm/square}] \quad (2.4)$$

The resistance of a rectangular-shaped sample is calculated by $R = \rho l / A$. The cross-section, A , of the rectangular shape can be defined by the width and the thickness as $A = wt$. If the shape is the special case of a square, then $w = l$, and $R = \rho / t = R_{Sh}$. This implies that irrespective of its dimensions, the resistance of a square sheet sample is equal to the sheet resistance. This also explains the unit of ohm/sq of the sheet resistance [48].

In real cases, the samples are not infinite in any dimension. Moreover, proximity of the probes to the boundaries of the sample, and the ratio of the sample dimension to the probe spacings affect the resistivity. Therefore, these factors must be introduced into the resistivity equation. The general expression of resistivity for finite-sized and random shaped bulk samples is given by

$$\rho = F \times \frac{V}{I} \times t \quad (2.5)$$

where $F=F_1.F_2.F_3$ is a geometric correction factor which consists of three different factors, namely, the ratio of sample thickness to probe spacing (t/s , F_1), the alignment of the probes in the proximity of a sample edge (F_2), and the finite lateral width of the sample (F_3). The correction factor of the thickness, F_1 , become equal to unity when $t/s < 0.2$. This rule is easily provided in the case of a thin film sample. Additionally, for a realistic case of a sample, F_1 and F_2 must be considered together [48]. In the literature, Smits submitted a table showing values of geometric correction factors for regular sample geometries [50]. This table is presented in Table 2.2 and the parameters used in calculation of these values are represented in Figure 2.4.

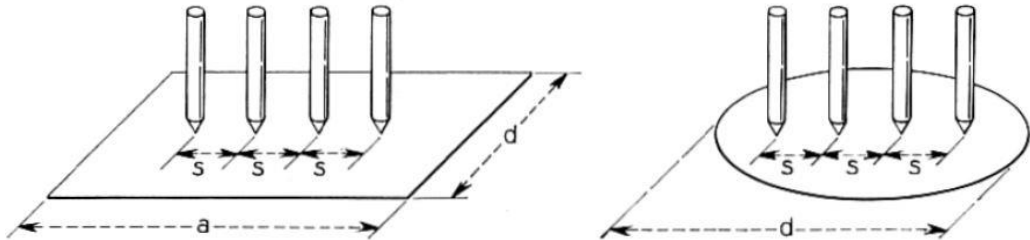


Figure 2.4. Parameters for the samples having regular geometric shapes [50]

Table 2.2. Geometric correction factors for regular geometries [50]

d/s	circle diam	$a/d=1$	$a/d=2$	$a/d=3$	$a/d\geq 4$
1.0				0.9988	0.9994
1.25				1.2467	1.2248
1.5			1.4788	1.4893	1.4893
1.75			1.7196	1.7238	1.7238
2.0			1.9454	1.9475	1.9475
2.5			2.3532	2.3541	2.3541
3.0	2.2662	2.4575	2.7000	2.7005	2.7005
4.0	2.9289	3.1137	3.2246	3.2248	3.2248
5.0	3.3625	3.5098	3.5749	3.5750	3.5750
7.5	3.9273	4.0095	4.0361	4.0362	4.0362
10.0	4.1716	4.2209	4.2357	4.2357	4.2357
15.0	4.3646	4.3882	4.3947	4.3947	4.3947
20.0	4.4364	4.4516	4.4553	4.4553	4.4553
40.0	4.5076	4.5120	4.5129	4.5129	4.5129
	4.5324	4.5324	4.5324	4.5325	4.5324

One of the most important property of VO_x thin films for microbolometer applications is their TCR value. It is usually given as percentage value (%TCR) and calculated by Equation (1.5).

In this study, sheet resistance and resistivity measurements were performed by Lucas Lab Pro4 resistivity system (see Visual 2.2). The system consists of four components; Keitley 2400 source meter, changable FPP head, Pro4 software and Pro4 stand. Probe spacings are 1,02mm and the highest applicable pressure on sample is 85 grams. Probes are made of Osmium. In addition, the system has an integrated heating stage and a thermocouple to measure the sample temperature.

In order to make the resistivity test, the sample is placed on the stage. After entering geometry of the sample and thickness of the film to the software, the probes are lowered onto the sample. The computer automatically controls the source meter and apply the ideal current for accurate readings. For temperature dependent resistance measurement, the heating source is adjusted to a specific heating rate. The changes occurring in voltage and temperature of the sample are recorded once for every 5°C of increasing stage temperature. The same procedure is also applied while cooling the sample. During resistance measurement, the temperature of the VO_x thin film is controlled to an accuracy of $\pm 2^\circ\text{C}$ using a PID controller (Eurotherm, 2216e). TCR values are calculated from obtained resistance-versus-temperature curves using Equation (1.5) in the temperature range from 24 to 100°C.



Visual 2.2. *FPP system present at Advanced Technology Thin Film Laboratory of Anadolu University*

2.2.2. Structural characterization

2.2.2.1. X-Ray diffraction technique

XRD technique is widely used to investigate the crystalline structure and the phase content of thin films. The XRD data present in the literature, and commercially available powder diffraction folders (PDFs) facilitate the evaluation of the obtained patterns. The technique does not require any sample preparation and the measurements can be performed in an open atmosphere with a non-destructive way. The area from which structural information is obtained is on the order of mm to cm, which is relatively large.

XRD obeys the well-known Bragg law which is

$$n\lambda = 2d\sin\theta \quad (2.6)$$

where λ is the wavelength of the X-Rays, d interplanar spacing and θ is the diffracted beam angle. Typically, 2θ is measured instead of θ in the spectrum.

In a thin film sample, lattice planes of crystals can be oriented in different directions relative to the surface of the sample. If the normal of lattice planes goes out of the sample surface, the planes are in the “out of plane” orientation. The planes in this orientation can be situated either parallel or inclined to the sample surface. If the normal of lattice planes lies parallel to the sample surface, it is said that the

planes are in the “in-plane” orientation. These manners of lattice planes are represented in Figure 2.5.

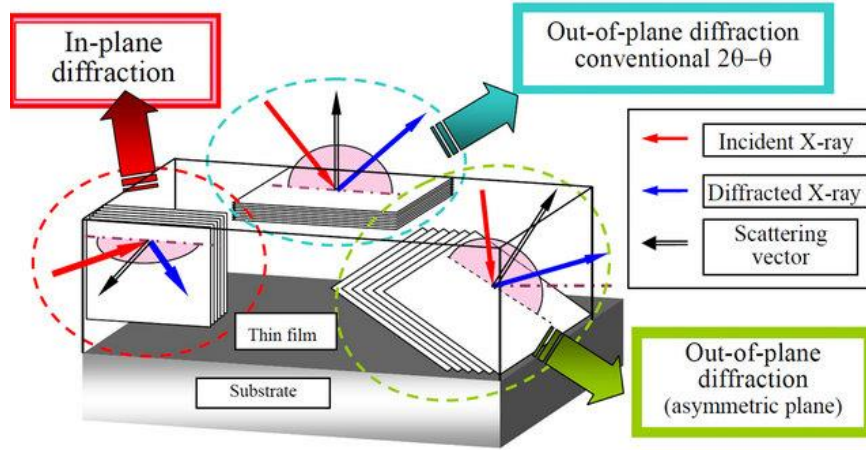


Figure 2.5. Orientation of crystallographic planes in a thin film sample [51]

In standard XRD (Bragg Brimento θ - 2θ) technique, the X-Ray source and the detector move symmetrically, relative to each other. For this reason, the technique is called symmetrical reflection measurement [51]. In this technique, the diffraction signals only from lattice planes parallel to sample surface (in out of plane orientation) are gathered. Because, typically, high angles of 2θ is scanned during measurement, X-Rays can penetrate deeply into the sample; such that also the diffracted beams from the substrate are collected by the detector. As a result, diffraction peaks of the substrate may surpass the peaks of the film and hinder analysis of the film.

In order to eliminate this effect and collect information only from the thin film, GIXRD technique is used. In this technique, the X-Ray source is adjusted to a fixed position to direct X-Ray beams on the sample at a specific low angle. Only the X-Ray detector is rotated in the scan range and collect diffracted beams. By this way, the diffracted beams from inclined planes are also detected by the detector. At extremely low angles of the incident beam, X-Rays are reflected by the sample surface. Increasing the incident angle slightly over a critical value causes the X-Rays to penetrate into the sample. In this case, the diffracted beams caused only by the film start to be collected. Further increasing the angle enhance the diffracted

intensity from the film, provided that the angle should not be allowed to exceed a critical value.

The GIXRD measurements were performed at Bilkent-UNAM laboratory. Panalytical X'pert Pro MRD device (see Visual 2.3) with $\text{CuK}\alpha$ radiation of 1,540598 nm wavelength. The system was operated at 40 kV and 25 mA. X-Rays were directed onto the samples at the grazing angle of 1° . The detector scanned a 2θ range from 10° to 70° by stopping at each $0,1^\circ$ for 20 seconds.



Visual 2.3. X'pert Pro MRD instrument present in Bilkent-UNAM

2.2.2.2. X-Ray photoelectron spectroscopy

XPS is a surface specific technique which can be used to identify elements and detect bonding states (or valence states) in a sample. In this technique, the characteristic X-Rays of a specific wavelength are directed onto a sample. This results in the ejection of core level electrons of the sample. The ejected electrons are called photoelectron and have some specific kinetic energies. The kinetic energy of a photoelectron is determined by the difference between binding energy and the energy directed photon. Because the energy of a directed photon is known, it is a direct indication of binding energy. After their ejection, some of the photoelectrons

undergo inelastic scatterings whereas some others scatter elastically. The inelastic interactions are the reason for the background in the spectrum. The electrons that have succeeded in escaping the surface are emitted in the vacuum and collected by electron energy analyzer [52].

In order to derive the kinetic energy of a photoelectron measured by an analyzer, E_k , the energy level scheme in Figure 2.6 can be used. According to the scheme, the kinetic energy of a photoelectron in the vacuum is calculated by $h\nu - E_b - \Phi_s$, where $h\nu$, E_b and Φ_s are photon energy, binding energy and work function of the sample, respectively. The kinetic energy measured by an analyzer with work function Φ_A is

$$E_{kin} = h\nu - E_b - \Phi_s - (\Phi_A - \Phi_s) \quad (2.7)$$

$$E_{kin} = h\nu - E_b - \Phi_A \quad (2.8)$$

Because the work function of the analyzer is a constant value, E_b can be calculated by measuring the kinetic energy of a photoelectron. Consequently, this equation is fundamental for the qualitative analysis in XPS [52].

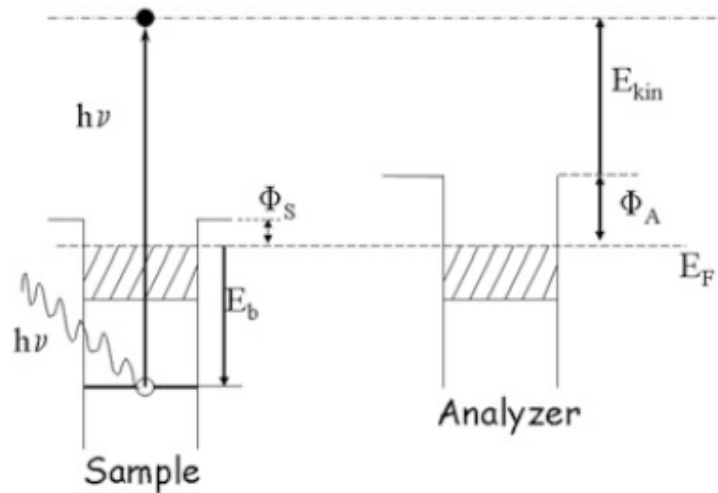


Figure 2.6. Schematic illustration of energy terms for the derivation of kinetic energy of the photoelectrons measured by analyzer [52]

Atomic electron levels are shown by nlj notation in spectroscopic notation system. Here, n denotes principle quantum numbers, e.g., 1,2,3,4... which can also be shown by K, L, M, N... letters. The angular momentum value, l , is equal to 0,1,2,3... for s, p, d, f subshells, and these letters are used in the notation. The j indicate total

angular momentum which is the absolute value of the sum of the angular momentum and spin momentum values; $j = |l + s|$. Table 2.3 exhibits notations of some possible electron levels. A photoelectron can belong to one of these electron levels associated with its energy [52].

Table 2.3. Spectroscopic notations of electron energy levels based on principle quantum number, n ; orbital angular momentum, l ; spin angular momentum, s ; and total angular momentum, j .

Quantum numbers				Spectroscopic notation
n	l	s	j	
1	0	$\pm 1/2$	$1/2$	$1s_{1/2}$
2	0	$\pm 1/2$	$1/2$	$2s_{1/2}$
2	1	$-1/2$	$1/2$	$2p_{1/2}$
3	1	$+1/2$	$3/2$	$2p_{3/2}$
3	0	$\pm 1/2$	$1/2$	$3s_{1/2}$
3	1	$-1/2$	$1/2$	$3p_{1/2}$
3	1	$+1/2$	$3/2$	$3p_{3/2}$
3	2	$-1/2$	$3/2$	$3d_{3/2}$
3	2	$+1/2$	$5/2$	$3d_{5/2}$

In the spectrum, the core electron energy levels whose total angular momentum values are higher than $1/2$, for p, d, f orbitals, appear in doublet peak structure. While all s orbitals are singlets, the other levels are doublets having a slight energy difference in between. For example, the p orbital for a specific principle quantum number, e.g., 3, consists of $3p_{1/2}$ and $3p_{3/2}$. The energy difference between doublets increases with increasing atomic number for same n and l while decreasing for l of the same n . The intensities of doublets are also proportional to each other. Their relative intensities are determined by the ratio of their degeneracy $(2j + 1)$ [52].

The chemical bonding between two atoms changes the binding energy of the electrons in the atoms. When a charge is transferred from an atom with a low electronegativity to another atom with a higher electronegativity, the charge of the former becomes positive, and the binding energy increases. On the other hand, the binding energy of the negatively charged atom decreases. These changes in the

binding energies appear as shifts in the spectrum and are called chemical shift. This is the main motivation for XPS analysis. Metal oxides show a shift of the metal XPS peaks to higher binding energies with the increase in their valence states. The energy peaks of different valence states of an element can take place at the same energy level with a chemical shift lower than peak width. Therefore, the attention must be given to separate the peaks to reveal the bonding states contained in the material [52].

In addition to electron core level peaks, XPS spectrum may contain some satellite peaks. These peaks can arise for various reasons. After excitation by X-Rays, a sample atom can remain at an excited state. The energy causing the atom to stay in that excited state is obtained by compromising the kinetic energy of the emitted photoelectron. This loss in the kinetic energy of the photoelectron gives rise to a satellite peak at a few eV higher binding energy side of the main element peak. For transition metals and rare earth metals these satellites can be quite strong. In some cases, these peaks can be discrete from the main element peaks (shake-up peaks). Sometimes, the energy loss occurring in the photoelectrons appear as a tail character (shake-off peaks) in the main element peak. This occurs when the photoelectrons interact with the electrons around the Fermi level. The tail character causes asymmetric peak shape. Beside these satellites, the satellites are also possible due to other type energy losses namely, plasmon loss peaks, satellite peaks caused by not using a monochromator, and multiplet splitting [52].

In XPS analysis, in order to determine the different bonding states of an element occurring in a sample, peak fitting, or so-called deconvolution process is applied. Because XPS peak character is a combination of Gaussian and Lorentz functions, peak deconvolution includes adjusting the Gaussian-Lorentz ratio besides the peak position, FWHM and peak area. In addition, determination of a correct peak shape requires background subtraction; thus, Shirley type background subtraction is always used in the literature [53, 54].

The XPS characterization of the VO_x thin films was performed by Thermo K-Alpha system with an X-Ray radiation of AlK_α at Bilkent-UNAM laboratories (an illustration of XPS measurement is shown in Figure 2.7). X-ray spot size was 400 μm. High-resolution spectra were obtained by an energy step size of 0.1 eV and pass

energy of 30 eV. The obtained spectra were analyzed by XPS 4.1 software. Because O1s peak is situated very close to vanadium core level peaks V2p_{1/2} and V2p_{3/2}, the peak deconvolution and background subtraction were applied by including these three peaks in the analysis. For the background subtraction, Shirley function was used.

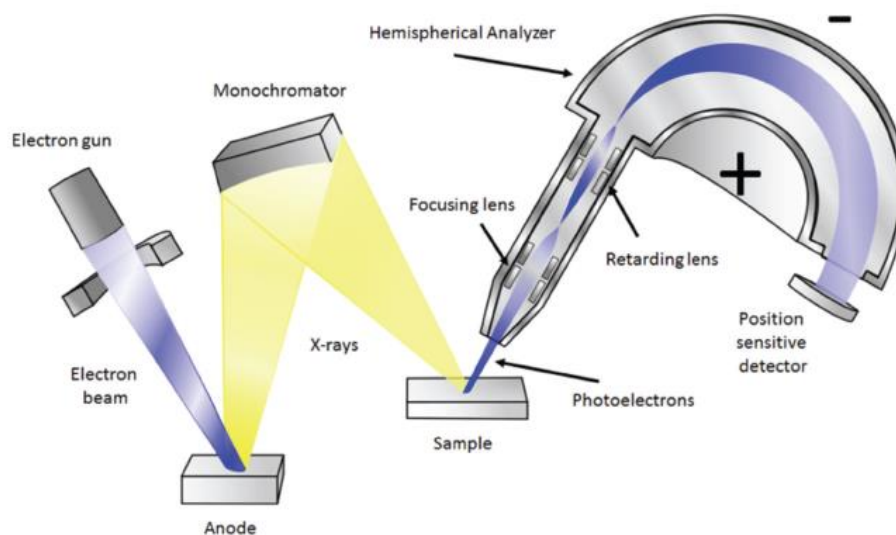


Figure 2.7. Schematic illustration of an XPS system [55]

2.2.2.3. Raman spectroscopy

In Raman spectroscopy, the laser beam of a specific wavelength is directed onto a sample, and the inelastically scattered beams, as a result of beam-molecule interaction within the sample, are collected. Scattering of the light from a sample occurs in different ways (see Figure 2.8). When the scattered light has the same frequency with the incident radiation, it is called Rayleigh scattering. Rayleigh scattering comprises more than 99.9% of all scattering phenomena. Thus, only a small portion of the scattered lights changes their frequencies and forms Raman scatterings. The change in the frequency is the result of molecular vibrations. Raman scattering has two components known as Stokes and anti-Stokes lines. When the incident light excites a molecule from a ground state to a higher energy state, the molecule may remain in an excited state during returning process. In this case, the frequency of the scattered light is lower than the frequency of the incident light. Therefore, Stokes lines appear in the spectrum with negative frequency shifts. Anti-Stokes lines appear in the spectrum when a molecule, found in an excited energy

state, is re-excited by the incident light and subsequently returns back to its ground state. This time, the frequency of the scattered light is higher than that of the incident light. Anti-Stokes lines display positive shifts in the spectrum. Stokes and anti-Stokes lines are symmetrically situated in the spectrum. However, due to the fact that most molecules are found in the ground state rather than an excited state at room temperature, Stokes lines are more intense than anti-Stokes lines. Because of this, Stokes scatterings are preferred as signals in conventional Raman spectroscopy. In Raman spectrum, frequency shifts are expressed as the reciprocal of wavelength (cm^{-1}) and shown in the horizontal axis [47, 56].

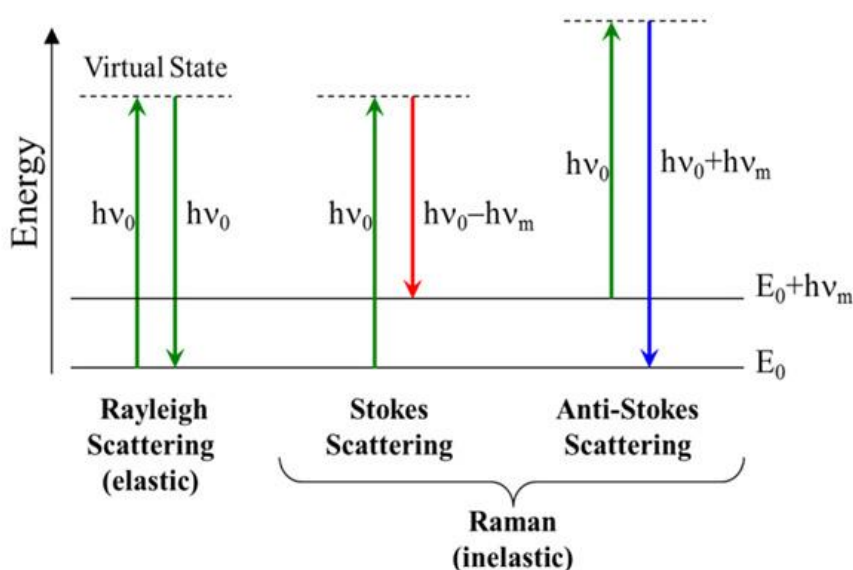


Figure 2.8. Energy diagram of Raman scattering

Understanding of process parameters is essential in order to obtain optimum results from Raman analysis. Raman spectrometers use various laser sources changing in wavelength [56]. Power of the laser is one parameter affecting the strength of the Raman signal and is on the order of milliwatts. Increasing the laser power will result in a higher signal power. Thus, it is desirable to keep the laser power as high as possible. Sometimes, the full laser power is used in the experiments. Unfortunately, some samples which are dark in colour or have absorption band close to the excitation wavelength tend to burn [57]. Consequently, a fine line should be chosen between maximizing the signal and burning the sample. Another key consideration is the aperture size. The aperture determines the amount of the Raman signal collected by the detector. Apertures are available as slits or

pinholes in design and can change in the range of 10-100 μm . As a general rule, the larger the aperture size, the higher the detector input signal. Usage of smaller sizes gives higher spectral resolution whereas the loss in spectral resolution is often insignificant in the case of larger sizes. The aperture size does not determine the resolution itself; the exposure time and the number of exposure are two parameters for adjusting the signal to noise ratio in the spectrum. The exposure time works analogously to one that exists in photographic cameras in which longer exposure times give better result in dim light. Hence, if the sample under examination is a weak Raman scatterer, then long exposure times also give better results. Increasing the number of exposures means averaging the collected spectra for a more accurate result. There is a trade-off between these two parameters to get a better-reduced noise. For samples having little shot noise, keeping the exposure time longer and the number of exposures low can produce less noise. For samples giving many Raman signals, precise control of these two parameters may not make a big difference [57].

Evaluation of Raman spectrum includes determination of characteristic peak positions and examination of peak intensities. In the present work, a literature survey was performed for the ascription of the peaks observed in the Raman spectra. Peak positions of various VO_x phases were determined. From the literature survey, Table 2.4, Table 2.5 and Table 2.6 were created on the basis of two important studies published recently. In one of these studies, Zhang et. al. [58] used two methods to prepare VO_x thin films with different stoichiometries. The first one is the post oxidation of the as-deposited vanadium films, which were deposited on Si (100) wafers from a vanadium target (99.95% purity) by magnetron sputtering. The post-oxidation was carried out in a furnace at 400°C in air with durations ranging from 10 min to 4 hours. The second one is the reduction of the as-deposited V_2O_5 thin films. The reduction process performed in a furnace of protective argon environment, at either 450°C or 500°C with a period ranging from 20 minutes to 10 hours. The phase evolution from VO_2 to V_2O_5 for the oxidation and V_2O_5 to V_2O_3 for the reduction processes could be observed by Raman inspection, respectively. The Raman results obtained from these experiments were used as a reference in order to deposit single phase V_2O_3 , VO_2 , V_6O_{13} , V_2O_5 thin films on Si(100) wafers with reactive sputtering by changing O_2/Ar gas flow ratios. The Raman spectra of these

films also presented in the study. In the study of Urena-Bergara et. al. [53], VO₂ thin films, fabricated on SiO₂/Si and Al₂O₃ substrates, were undergone thermal oxidation process from R.T. to 550°C, in the air. Phase transitions, occurred in VO₂ during oxidation, were investigated by Raman spectroscopy. Current and resistance changes also recorded in parallel with the Raman measurements to make a correlation with changing film stoichiometry. Consequently, the Raman peak positions and relative vibration modes were submitted in the study.

Table 2.4. Frequency shifts (cm⁻¹) of the VO₂ Raman peaks from the literature.

VO ₂					
[58]			[53]		
Oxidation of vanadium film	Redeuction of V ₂ O ₅	Reactive Sputtering	①	②	③
144	142	142	140	-	196
193	191	193	192	193	225
223	223	223	223	223	
260	260	260	260	262	
308	308	308	308	-	
334	334	334	338	342	
389	389	389	387	386	
497	437	497	395	398	
613	611	612	440	440	
			482	480	
			497	498	
			588	581	610
			613	614	
			661	662	
			823	829	

① As-deposited film fabricated by electron beam evaporation with 500°C substrate temp.
 ② Post oxidized up to 400°C and cooled down to R.T.
 ③ Post oxidized up to 450°C and cooled down to R.T.

Table 2.5. Frequency shifts (cm^{-1}) of the V_2O_5 Raman peaks from the literature.

V_2O_5					
[58]			[53]		
Oxidation of vanadium film	Reduction of V_2O_5	Reactive Sputtering	①	②	③
145	145	145	102	100	101
195	195	195	145	144	145
284	284	284	197		
303	303	303	284	282	284
405	405	405	304	304	303
483	700	483	405	405	405
528	996	701	481		483
701		992	528	529	528
			700	700	702
			995	995	996

① Post oxidized up to 500°C cooled down to R.T.
 ② Post oxidized up to 400°C cooled down to R.T.
 ③ Post oxidized up to 450°C cooled down to R.T.

Table 2.6. Frequency shifts (cm^{-1}) of the V_6O_{13} , V_2O_{13} and VO_x Raman peaks from the literature.

V_6O_{13}			V_2O_3	VO_x	
[58]		[59]	[58]	[53]	
Oxidation of vanadium film	Reduction of V_2O_5	Reactive Sputtering	Reduction of V_2O_5	Post oxidized up to 450°C cooled down to R.T.	
167	167	161	94	225	165
845	846	838	137	293	787
880	881	875	188	504	845
936	1033	925	275	576	881
992		978	300		912
1033		1025	403		934
			475		1031
			520		
			684		
			990		

VO_x - represents possible layered phases, such as V_6O_{13} , V_3O_7 according to relevant article

For Raman measurements in the present study, a He-Ne laser source with the wavelength of 532 nm was used. Laser power was kept at 10 mW and 50X objective lens was selected to minimize local heating of the samples.

2.2.2.4. Transmission electron microscopy

TEM is an indispensable technique for the structural characterization of nanometer-sized features. The samples which will be examined under TEM must be thin enough to transmit electrons. Therefore, thin films are ideal materials to reveal

their structural properties by TEM. We can separate the operation modes of TEM into two general classes; imaging modes and analytical modes. In imaging modes, structural features can be observed directly, whereas, in analytical modes, information about structure can be obtained indirectly by the analysis of the diffracted beam geometries and energies. It is worthwhile to emphasize that TEM allows data acquisition from imaging and diffraction modes almost simultaneously.

Electron diffraction can be understood in a similar way to Huygens principle for diffraction of light [60]. While Huygens principle explain generation of diffracted beams, Bragg equation makes a correlation to show how the diffraction angle depends on interatomic distance and the wavelength of the electrons

$$2d\sin\theta = n\lambda \quad (2.9)$$

The wavelength of the electrons which is accelerated under 300kV is about 0.00197 nm. Interplanar spacing value, d , is as small as 0.2 nm. From these values one can calculate with the help of Bragg equation that the diffraction angle is 0.28° . Compared to those in XRD, the diffraction angles are smaller in electron diffraction and change within the range of $0^\circ < \theta < 1^\circ$, as a rule. Moreover, the reflecting lattice planes are almost parallel to the incident beam. Therefore, the zone axis is regarded as the direction of the incident beam [60].

From a diffraction pattern, it is possible to calculate the interplanar spacings of a structure by measuring the distances of the spots or rings from the central spot. To do this it is necessary to derive camera equation (see Figure 2.9) [61]. Bragg equation is

$$2d\sin\theta = n\lambda \quad (2.10)$$

the wavelength of the electrons under 300kV is 0.00197 nm such that $\theta \sim 1^\circ$ [60].

Hence

$$\sin\theta \sim \tan\theta \sim \frac{1}{2}\tan(2\theta) \quad (2.11)$$

by the geometry of Figure 2.9

$$\tan 2\theta = \frac{r}{L} \quad (2.12)$$

we substitute

$$2d \frac{1}{2L} = \lambda \quad (2.13)$$

$$rd = \lambda L \quad (2.14)$$

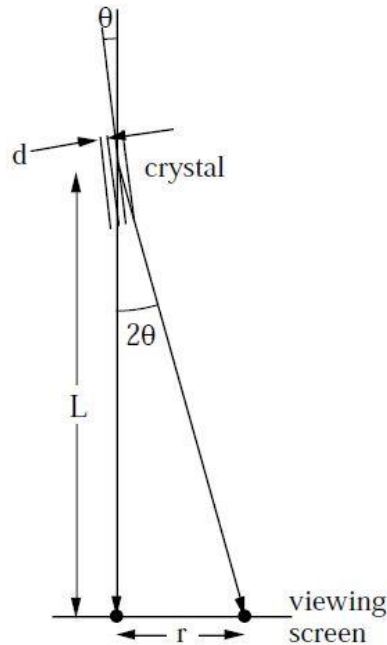


Figure 2.9. Geometry for electron diffraction and definition of camera length, L [61].

The appearance of an electron diffraction pattern depends on the crystallinity of a sample under examination. Each set of parallel lattice planes in a crystal forms two diffraction spots on the pattern as it is seen in Figure 2.10a. A single crystal sample consists of many sets of parallel lattice planes; therefore, a regular array of diffraction spots are observed in the pattern. Moreover, this pattern is the characteristic of that crystal structure. If the sample comprises more than one crystal of a phase, as in the case of a polycrystalline sample, nested rings appear in the pattern (Figure 2.10b). For the spots located on the same rings, d values are the same [60]. The diffraction patterns of a polycrystalline and an amorphous sample can sometimes look similar. However, in the amorphous sample, diffraction rings are broader and do not include any spots on them. In this case, the pattern is called diffuse rings. As the sample turns into a polycrystalline and grain size of the sample increases, the rings become narrower. If the grain size increases further, discrete spots appear on the rings [62].

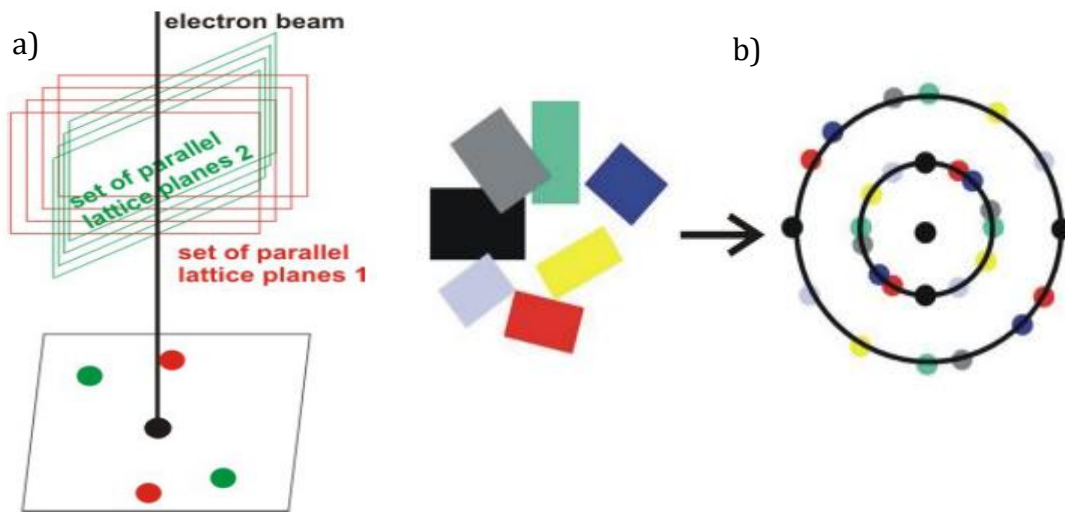


Figure 2.10. a) Formation of diffraction spots and b) polycrystalline diffraction rings formed by crystals of same phase oriented differently [60]

Before giving information about the imaging modes of TEM, it is useful to mention the basic contrast mechanisms seen in TEM. Elastic interactions are used in contrast forming mechanisms. The electrons passing through a TEM sample can undergo some elastic scatterings due to Coulombic interactions with the nuclei of the sample atoms. The positively charged nucleus of an atom deflects the electrons from their paths. The degree of this deflection is dependent on the magnitude of the charge in the core. The greater the magnitude, the greater the angle of the deflection. Because atoms with high atomic numbers carry more charge in their nuclei, they scatter electrons with higher angles. If an aperture is inserted into the back focal plane of the objective lens such a way that only electrons without any interaction are allowed to pass the aperture; then, the areas having higher atomic number in the sample appear in darker contrast than the areas having a lower atomic number. This is called mass contrast. Furthermore, the number of the scattered electrons increases with the increasing sample thickness. Thus, thick areas of the sample appear darker relative to thin areas. This type contrast is called thickness contrast (see Figure 2.11) [60]. Another type of contrast is caused by the crystalline areas in the sample. The electrons are strongly scattered by the planes of the crystals according to Bragg law. As a result, crystalline regions appear in dark contrast in the bright field (BF) image. This is known as diffraction or Bragg contrast. These three

contrast mechanisms can simultaneously contribute to image formation which complicating the interpretation.

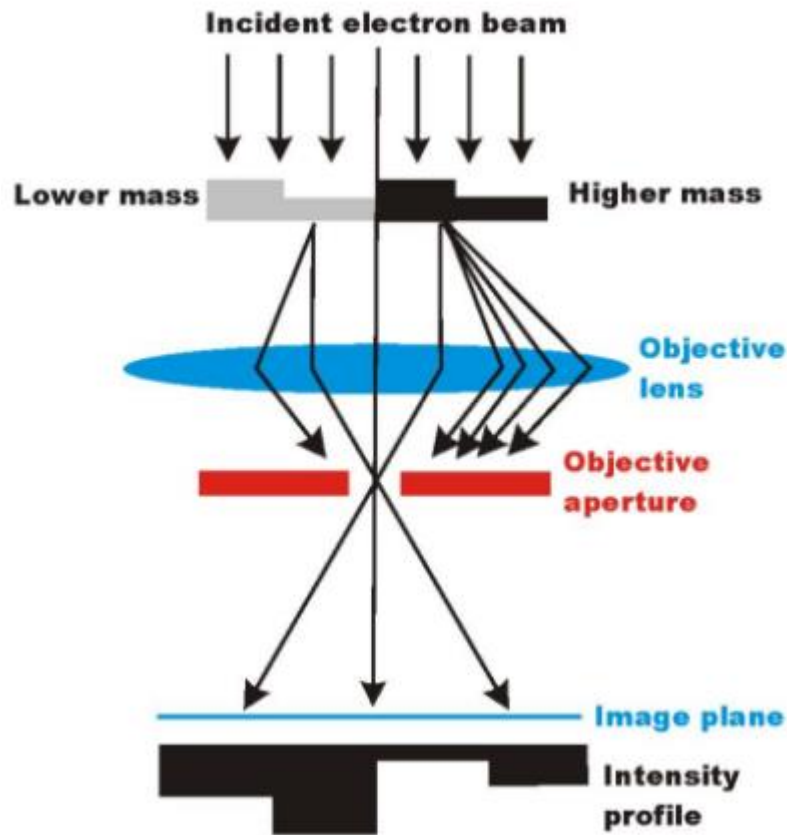


Figure 2.11. Contrast formation in BF mode of TEM [60]

In the BF mode, an aperture is placed into the back focal plane of the objective lens and only the direct beams are allowed to pass the aperture. In other words, the aperture is located on the way of the optical axis. The BF image, as a result, is created by the weakening of the direct beam. The scattered electrons due to any reason, are deflected away from the optical axis, so contribute to the formation of dark contrast. In dark field (DF) mode, one or more diffracted beams are allowed to pass the aperture by placing it appropriately. In this case, the diffracting areas in the sample appear in bright contrast while all other regions are dark.

High-resolution TEM (HRTEM) is used for direct observation of atomic structure and defects in a sample. It relies on image formation by phase contrast. HRTEM image provides structural information in 2D.

Beside elastical scatterings, a number of electrons passing the sample also undergo inelastic scatterings and suffer energy losses. The energy of these electrons is recorded as electron energy loss spectra (EELS). The EELS mainly consists of three parts: zero loss, low-loss (<100 eV) and high-loss (>100 eV) regions. Zero-loss region includes the electrons which are scattered elastically or without any interaction. The intensity of this region is high in thin samples. The electrons from this region do not carry useful information, and the damage of CCD chip can occur because of high intensity; hence, they are blocked during spectrum collection. The low-loss region includes plasmon peaks. The high-loss region is the most important part and includes energy losses resulting from ionization process of atoms. There are specific critical ionization energies for each energy shell of elements. Electrons after ionizing the atoms, lose their energies as the amount required for the ionization process. Therefore, electrons that undergo this kind of energy loss lead to the creation of ionization edges in the spectrum. Compared to other inelastic scatterings, ionization interactions are less frequent. As a consequence, intensities are lower in this region, and generally, detection of light elements are performed by EELS spectrum.

In order to reveal the porous structure of the films produced in the scope of the current study, elemental spectroscopic imaging (ESI, acquisition of elemental maps) seemed like an effective method. This is done by recording EEL (by means of Gatan Imaging Filter) spectrum of the corresponding element and applying the so-called three window method. The whole technique is called electron spectroscopic imaging. Three window method is applied by obtaining an image after a suitable ionization edge of the corresponding element (post-edge image, ΔE_3) and two additional images at energies lower than the ionization edge (pre-edge image1, ΔE_1 and pre-edge image2, ΔE_2) (see Figure 2.12). Only electrons within a specific energy range (energy windows; ΔE_1 , ΔE_2 , and ΔE_3 in Figure 2.12) can contribute to these images by using a selected energy slit. The pre-edge images are used to determine the background approximately and create a contrast-enhanced image of an elemental map.

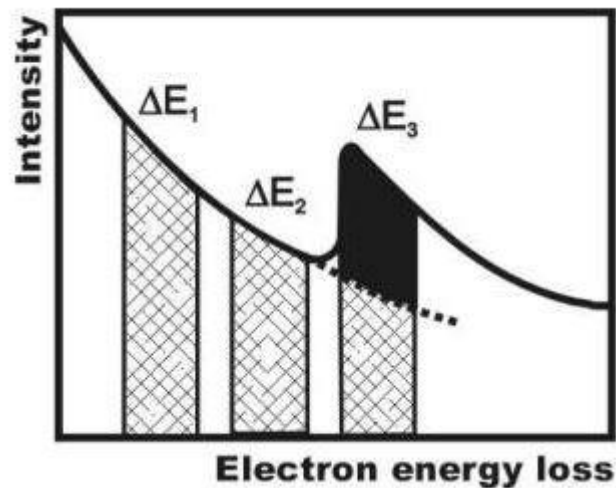


Figure 2.12. *Three window method: Background is determined by the pre-edge images (ΔE_1 , ΔE_2) and subtracted from post-edge image (ΔE_3). Only the black area contributes to the corresponding elemental map [63]*

In the present study, TEM investigation of VO_x thin films was completed at Bilkent-UNAM laboratories. TECNAI F30 system with 300 kV operating voltage was used in the experiments (see Visual 2.4.). Experimental parameters for elemental maps were given in Table 2.7. The ionization edges of vanadium (V-L) and oxygen (O-K) overlaps strongly in the spectrum. Therefore, complete separation of vanadium and oxygen and constitute reliable vanadium and oxygen maps are not possible. However, oxygen can not be found in a free state inside the VO_x films and is connected to vanadium. From this chemical consideration, we assumed that vanadium sites in the vanadium maps also include oxygen and vice versa. Here, our aim is to show pore regions where neither vanadium nor oxygen exists. We have taken oxygen maps beside the vanadium map as supplementary images. In addition, nitrogen maps were taken to check possible diffusion of nitrogen from the substrate into the film. TEM samples were prepared by NNL-600I model focused ion beam (FIB) system (see Visual 2.5). FIB is a fast and reliable technique. Sample preparation takes maximum 2-4 hours. Other techniques are not precise as much as FIB in selecting the target area.

Table 2.7. Acquisition parameters of the ESI images

	V-L	O-K	N-K
Center of energy windows:			
Pre-edge1 (eV)	463	484	353
Pre-edge2 (eV)	493	517	383
Post-edge (eV)	538	547	416
Slit width (eV)	30	30	30
Exposure time (image/s)	1/20	1/20	1/20

The FIB-prepared sample is an electron-transparent lamella which is mounted to a support grid. In order to prepare the lamella, firstly, platinum (Pt) is deposited on a selected rectangular area of the sample. Pt is deposited to mark the selected area, protect the top portion of the sample and glue the manipulator tip to the sample. Then, two trenches are dug on both long sides of the area. The resulting lamella is lifted out from its trench with the help of the manipulator tip. Then, the lamella is mounted to the grid from its one side. If the lamella is long, it is mounted from its two opposite sides, to ensure the stability. Finally, the lamella is further thinned by gallium ions to an electron-transparent thickness.



Visual 2.4. TECNAI F30 TEM instrument present in Bilkent-UNAM



Visual 2.5. *NNL-6001 FIB system present in Bilkent-UNAM*

3. EXPERIMENTAL RESULTS

3.1. Electrical Results

Electrical characterization of the produced VO_x thin films includes resistivity, sheet resistance and temperature dependent resistance measurements from which TCRs were calculated. The activation energies were extracted from lnR-versus-1000/T plots; therefore, pre-exponential factor σ_a (conductivity pre-exponential factor) and activation energy relation of the films were examined. The details of the measurements were given in section 2.2.1.1. The electrical results of all films were presented in Table 3.1. According to the results, sheet resistances of the as-deposited films are in the range of ~820-870 k Ω /sq. Annealing at 200°C for 3 hours in pure N₂ ambient decreases the sheet resistances down to ~235 k Ω /sq. Annealing at 300°C, in the same condition, raised the resistances again up to a range of ~310-335 k Ω /sq.

Table 3.1. Electrical results of the VO_x thin films deposited on Si₃N₄/SiO₂/Si substrates. N.A. (no analysis) indicates that analysis could not be performed due to oscillations in voltage.

Sample name	Post annealing	Sheet Resistance (k Ω /sq)	Resistivity (Ω .cm)	ΔE_a (eV)	TCR (-%/°C)	
					heating	cooling
VOx-1	as-deposited	823.3±1.5	8.2 ±1.5	0.307	3.8	3.7
VOx-5	as-deposited	830.7±3.5	8.3 ±0.3	—	N.A.	
VOx-6	As-deposited	866.3±2	8.6 ±3	0.331	4.1	3.9
VOx-2	200°C	235.1±0.5	2.3±2.5	0.262	3.2	3.1
VOx-3	200°C	234.1±2	2.3±2	0.265	3.3	3.3
VOx-4	200°C	231±3.5	2.3 ±1	0.307	3.8	3.4
VOx-7	300°C	309.1±0.5	3.0±5	—	N.A.	
VOx-8	300°C	316.3±2	3.1±3	—	N.A.	
VOx-9	300°C	332.3±2	3.3±1	—	N.A.	

As it is seen from the table, the TCR values calculated from the lnR-versus-temperature curves are very suitable for microbolometer applications (<-2%/°C). However, due to high fluctuations in voltage during the measurements, the TCR calculation of some samples could not be performed. These samples include an as-deposited film and the films annealed at 300°C. This is possibly due to the high defect states of these films. One observation from the table is that the room temperature sheet resistances (or resistivities) of the as-deposited films decrease nearly four times after annealing the films at 200°C. However, the decreases in TCR

values are not at this rate. Besides, the TCR value of the as-deposited sample VOx-1 is equal to that of VOx-4, which is annealed at 200°C.

The $\ln R$ -versus-temperature curves of the films were presented below (see Figure 3.1, 3.2, 3.3, 3.4, and 3.5). The inset plots show temperature dependency of the resistance of the produced films. The non-linear characteristic of the curves corresponds to the Arrhenius-like relation in accordance with Equation (1.4). This indicates that charge carrier migration is mainly thermally activated process. The TCR values were calculated both from the heating and the cooling cycles. The $\ln R$ values showed a linear change up to $\sim 40^\circ\text{C}$, which indicates almost a constant slope and TCR as well. Generally, only slight differences were observed between the TCR values obtained from the heating and the cooling cycles. Microbolometers are fabricated mostly to detect IR range of 8-14 μm , therefore, the TCRs were calculated around room temperature by linear fitting the $\ln R$ -versus-temperature curves up to $\sim 40^\circ\text{C}$.

The $\ln R$ -versus-temperature curves of VOx-1 and VOx-6 samples exhibit a linear change around room temperatures (see Figure 3.1 and 3.2). Because high electrical resistance gives rise to high TCR, the TCR values are considerably high. The TCR value of VOx-5 sample could not be calculated because of the fluctuations in voltage.

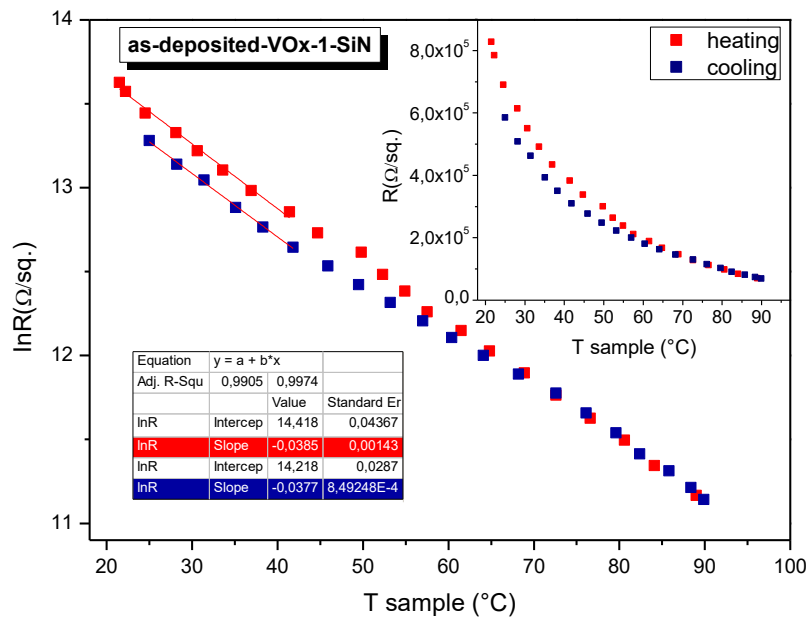


Figure 3.1. $\ln R$ -versus-temperature curve of as-deposited film of VOx-1

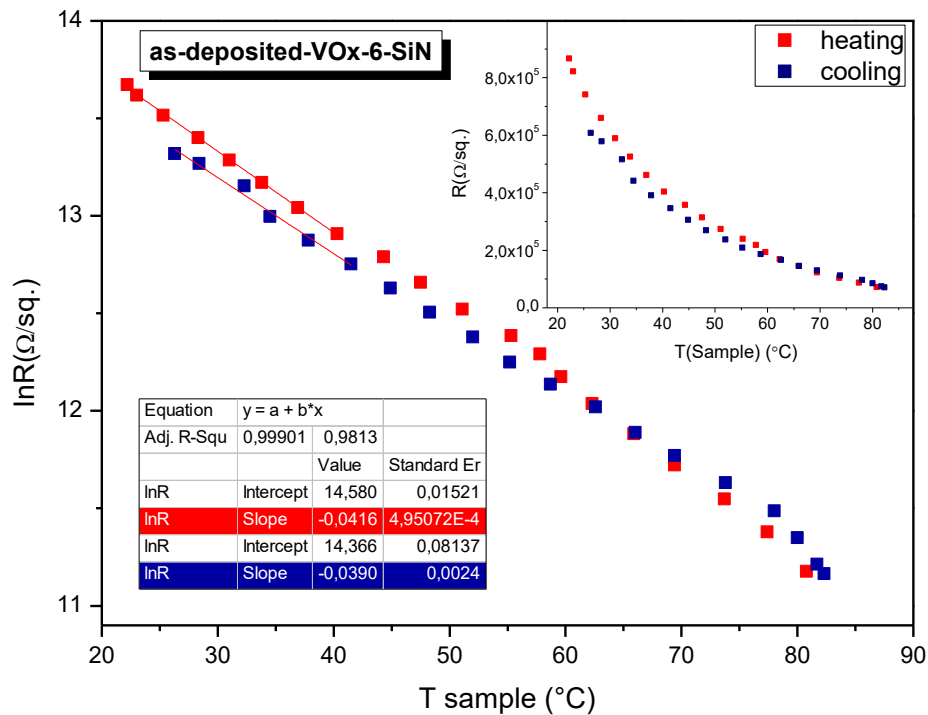


Figure 3.2. *lnR-versus-temperature curve of as-deposited sample of VOx-6*

The VOx-2 and the VOx-3 samples of the 200°C annealed films exhibit a linear change in lnR value at room temperatures (see Figure 3.3 and 3.4). Their TCR values are lower than those of the as-deposited films. This is consistent with the decreasing sheet resistances. Nevertheless, the TCR values are still high and do not show significant drops as the drops of sheet resistances were taken into consideration. While VOx-2 and VOx-3 samples show a slight hysteretic behaviour at high temperatures, this is more apparent for the VOx-4 sample (see Figure 3.5). Moreover, its TCR value is somewhat higher than those of other two samples, and the sheet resistance is slightly lower. This hysteretic behaviour is ascribed to the VO₂ phase content which is included more in the VOx-4 sample than other two samples [44].

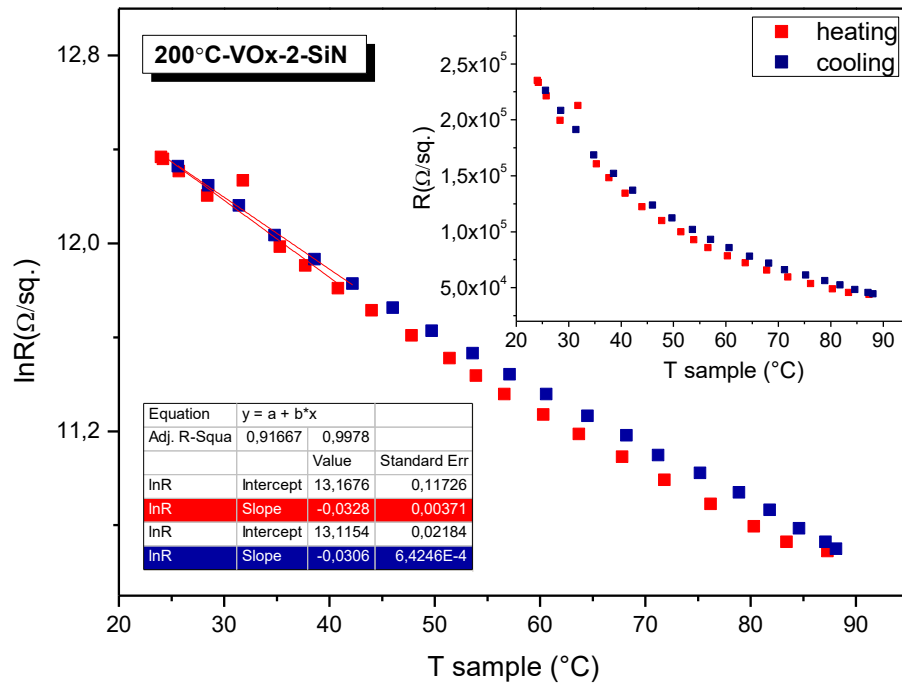


Figure 3.3. *InR*-versus-temperature curve of VOx-2 sample annealed at 200°C

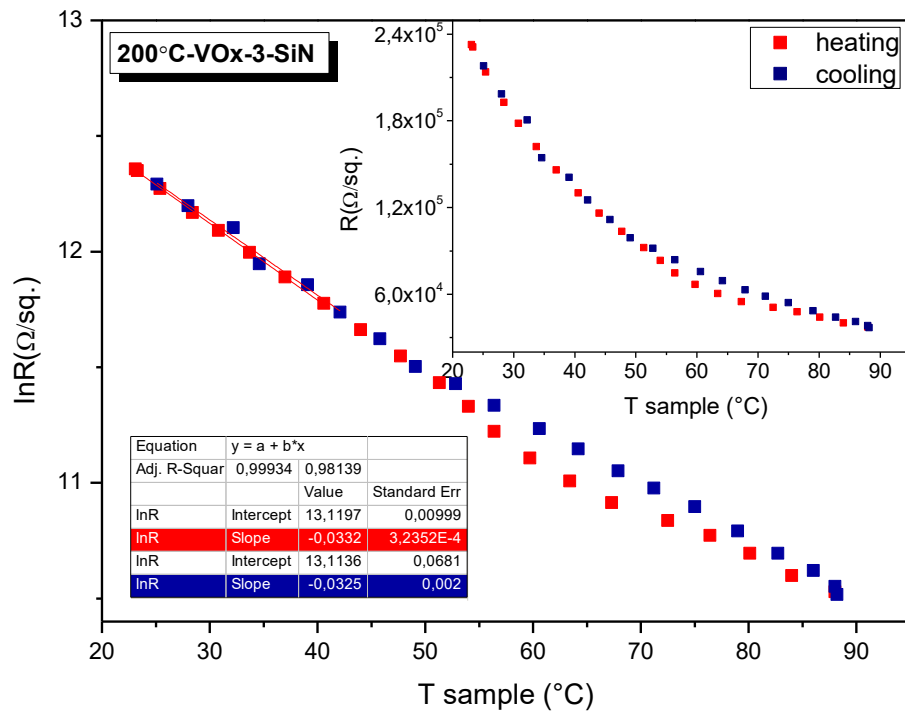


Figure 3.4. *InR*-versus-temperature curve of VOx-3 sample annealed at 200°C

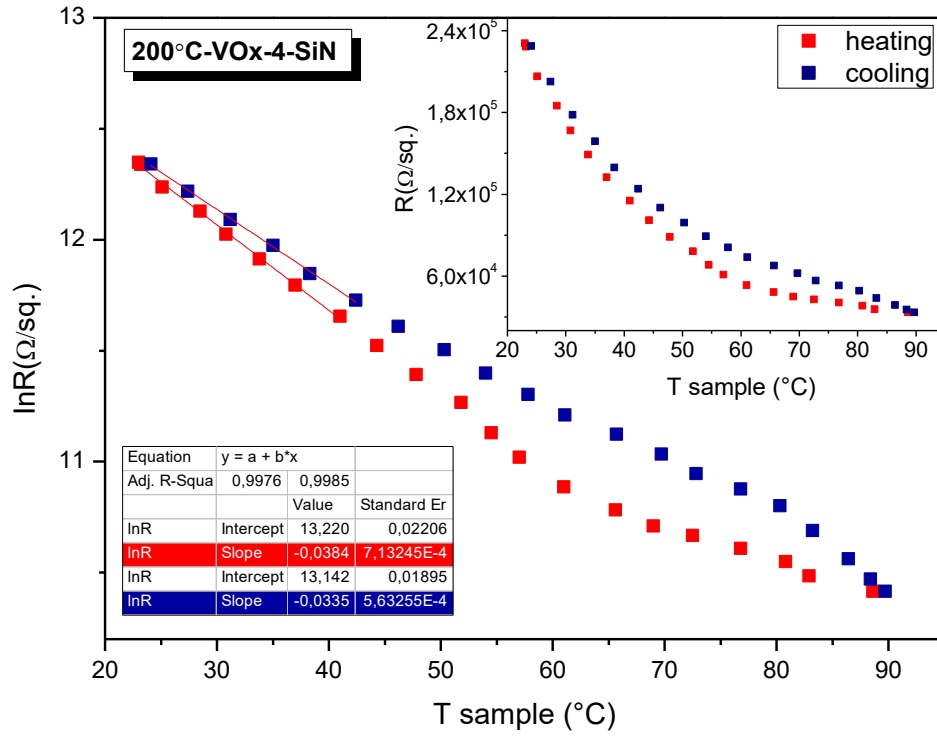


Figure 3.5. *lnR-versus-temperature curve of VOx-4 sample annealed at 200°C*

In Equation (1.4) if we take logarithms of both hand sides and rearrange the equation we obtain

$$\ln R(T) = -\left(\frac{\Delta E_a}{k_B}\right)\left(\frac{1}{T}\right) + \ln R_0 \quad (3.1)$$

ΔE_a can be directly obtained from a curve of $\ln R(T)$ -versus- $1000/T$, where the slope of this curve gives $\Delta E_a/k_B$ in the unit of K/1000. Another alternative way to calculate ΔE_a is using the relation in Equation (1.5). Here, the former method was used and the corresponding curves were given in Figure 3.6. The calculated ΔE_a values can be seen from Table 3.1. It can be noticed that these values are in direct proportion to the calculated TCRs for both the as-deposited and the 200°C annealed films.

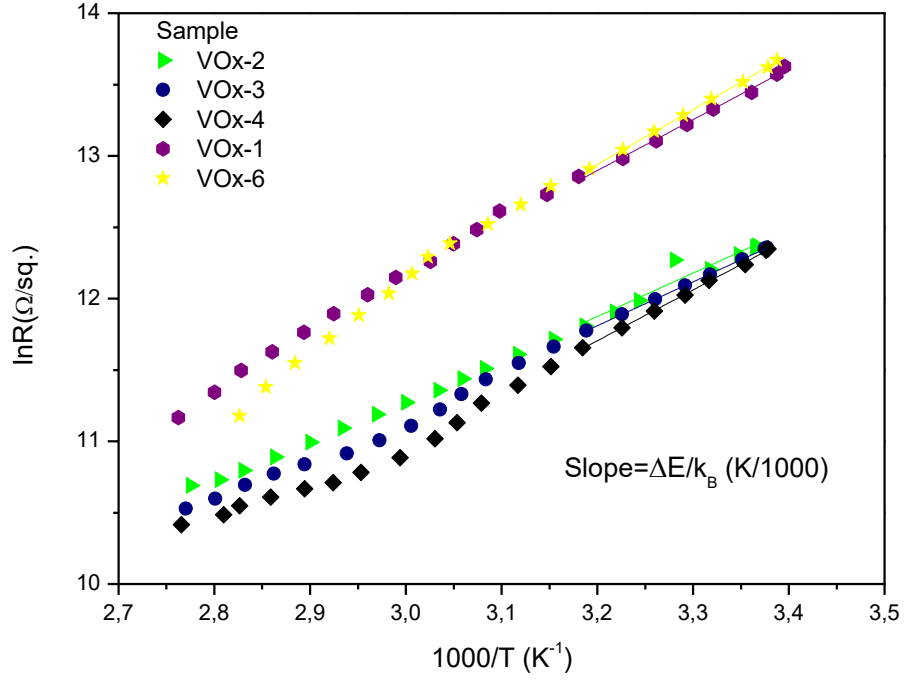


Figure 3.6. *lnR-versus-1000/T curves of the VOx thin films: the curves were obtained from heating cycles*

Moreover, we examined the pre-exponential factors (σ_a) of the films as a function of their activation energies. The well known Meyer-Neldel Rule (MNR) (also known as the compensation rule) has been observed in a variety of materials such as amorphous and nanocrystalline materials, exhibiting thermally activated behaviour [42, 64, 65]. According to the MNR, if electrical conductivity obeys Arrhenius-like relation in response to temperature variation, which is expressed as follows

$$\sigma = \sigma_a \exp\left(-\frac{\Delta E_a}{k_B \times T}\right) \quad (3.2)$$

then pre-exponential factor is correlated with activation energy according to the relation below

$$\sigma_a = \sigma_{a0} \exp\left(-\frac{\Delta E_a}{E_{MN}}\right) \quad (3.3)$$

where σ_{a0} and E_{MN} are constants, referring Meyer-Neldel pre-exponential factor and activation energy, respectively. The MNR rule mostly expressed below

$$\ln \sigma_a = \ln \sigma_{a0} + \left(-\frac{\Delta E_a}{E_{MN}}\right) \quad (3.4)$$

Similar to the resistance variations in response to temperature change observed in the VOx thin films, the electrical conductivities, as a function of temperature, exhibit Arrhenius-like relation. Therefore, by means of $\ln\sigma$ -vs- $1000/T$ plots, the $\ln\sigma_a$ values were obtained from the intercept values. The corresponding plot was drawn and given in Figure 3.7. The Intercept values were presented within the figure. The conductivity values were calculated by taking reciprocals of the resistivities (ρ).

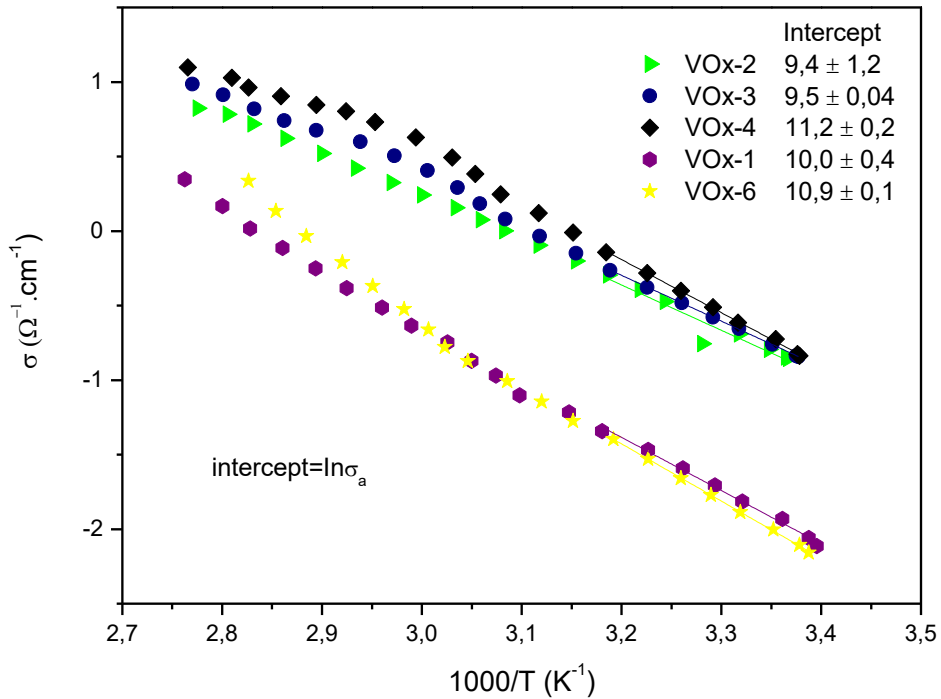


Figure 3.7. $\ln\sigma$ -vs- $1000/T$ curves of the as-deposited and 200°C annealed films

Figure 3.8 presents the pre-exponential factors as a function of the activation energies. The slopes and intercepts of the fittings were represented inside the figure. They correspond to $1/E_{MN}$ and $\ln\sigma_{a0}$ constants, respectively. The $\ln\sigma_a$ values of the 200°C annealed samples change linearly by activation energies, hence, there is an exponential relation between pre-exponential factors and activation energies of the film in accordance with Equation (3.3). The positive slopes indicate that the as-deposited film obeys the conventional Meyer-Neldel compensation rule. However, for the as-deposited films, two samples are not enough to see the type of the

trendline of this relation. Therefore, it is not possible to make an assessment of the as-deposited films. Consequently, because this does not constitute a critical point for the study, its assessment has been left to the ongoing studies.

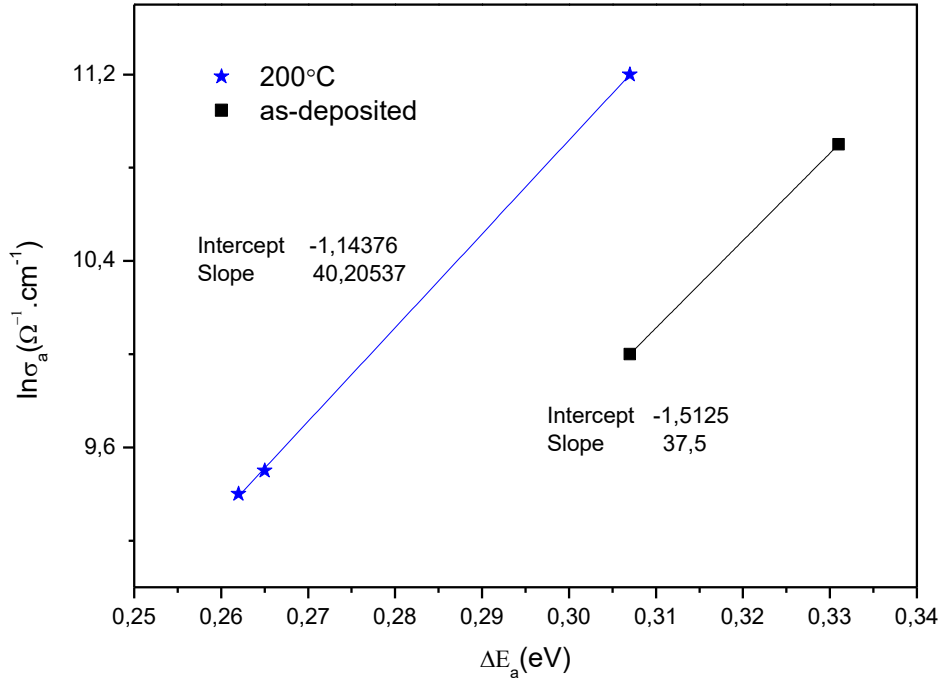


Figure 3.8. Pre-exponential factors σ_a as a function of the calculated activation energies (ΔE_a) of the VOx thin films

As a result, the differences observed in all electrical results of the produced films are indications of structural changes in micro-nano scale. Therefore, in order to investigate structural properties of the films in detail and make a correlation with electrical results, we chose one sample from each film group. The results of these structural investigations were presented in the following sections.

3.2. Structural Characterization Results

3.2.1. Grazing-Incidence X-Ray diffraction results

The conditions in which GIXRD measurements were performed were given in section 2.2.2.1. The GIXRD patterns of the as-deposited and the annealed films were presented in Figure 3.9. The GIXRD patterns of the as-deposited film and the 200°C annealed film do not include any characteristic peak. This suggests that the films are amorphous or nanocrystalline with very small grain sizes. On the other hand, the

GIXRD pattern of the 300°C annealed film show many characteristic peaks of VO_x phases. The film basically consists of monoclinic VO₂ phase with peaks appearing at ~27.89, 37.15, 42.24, 42.42, 44.78, 52.95, 52.60, 56.96°. Although these peak positions are in good agreement with VO₂ phase, most of these peaks also match with V₂O₃ phase. Therefore, we can not completely ignore the existence of V₂O₃ phase; so, the peaks have also remained as marked with the V₂O₃ phase in Figure 3.9. The other peaks of V₂O₃ phase appear at ~ 54.01 and 57.49°. The peak at ~65.07° was attributed to orthorhombic V₂O₅ phase. The peak located at ~ 51.88° could not be clearly attributed to any phase (illustrated as VO_x in Figure 3.9). The best match of this peak with a phase candidate was provided by V₂O₅ or V₆O₁₃ (PDF numbers 00-041-1426 and 00-027-1318, respectively).

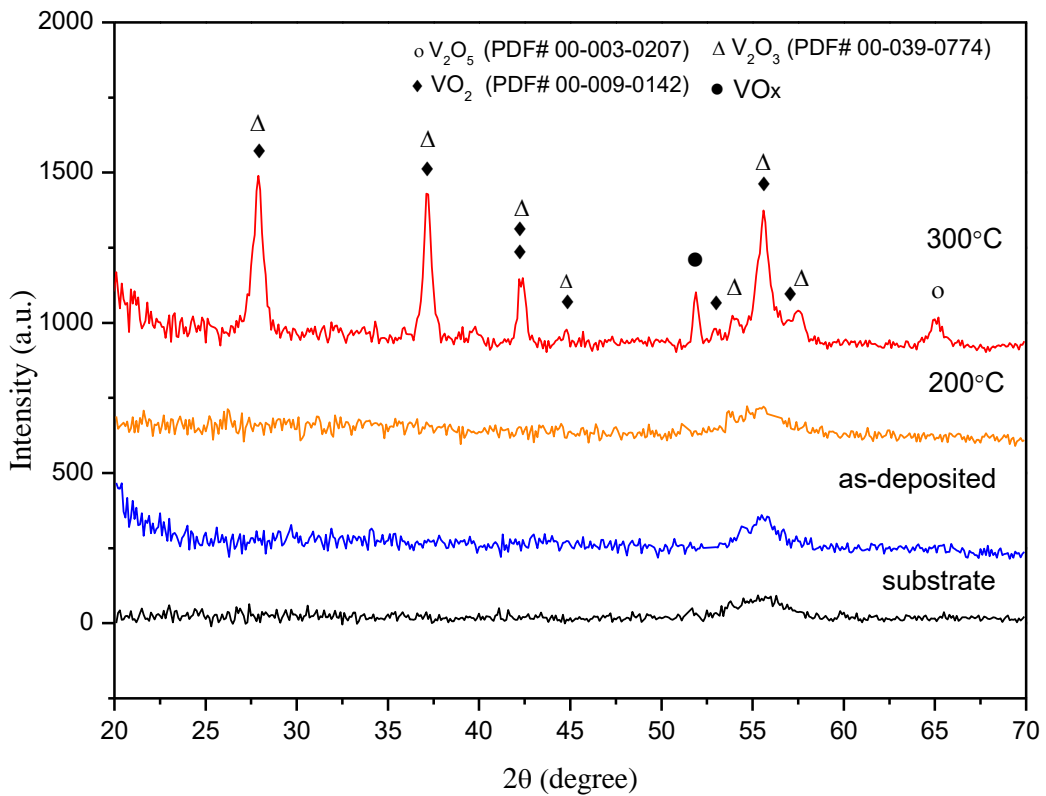


Figure 3.9. XRD patterns of the VO_x thin films. VO_x indicates possible layered phases of VO_x, e.g., V₆O₁₃, V₃O₇.

3.2.2. Raman results

Raman spectra of the films were presented in Figure 3.10. The power of the laser was set at 10 mW, and 50X objective lens was used to focus the laser beam.

The spectral resolution was calculated to be $\sim 1.16 \text{ cm}^{-1}$ in the range of 0-1200 cm^{-1} . The evaluation shows that the spectra contain V_2O_3 , VO_2 , V_6O_{13} and V_2O_5 phases. In as-deposited film, the peak located at $\sim 140 \text{ cm}^{-1}$ is related to soft phonon vibration of VO_2 phase. The peak at 192 cm^{-1} is an indication of monoclinic VO_2 phase with space group of P21/c. It relates to lattice vibration of V-V bond [53, 58]. V_2O_5 and V_6O_{13} are both layered oxides and show similar structure; therefore, they can show close Raman peaks in the spectrum [59]. V_6O_{13} exists in monoclinic structure with the space group of C2/m at room temperature while V_2O_5 crystallizes in orthorhombic structure with Pmmn space group. Their Raman modes can be divided into two groups: low-frequency external modes and high-frequency internal modes. External modes are caused by vibrations of units whereas internal modes are caused by the stretching and bending vibrations of V-O bonds [59]. The Raman peak appearing at 96 cm^{-1} was attributed to rigid-layer mode (external mode) of V_6O_{13} phase. In the spectrum, some of the peaks are situated at very close frequencies and create a multiple peak structure: the ones at $\sim 280, 285, 301 \text{ cm}^{-1}$ and $400, 403, 405, 410 \text{ cm}^{-1}$. At these frequencies, V_2O_5 and V_6O_{13} phases come into prominence. However, It is not easy to match some of these peaks directly with one of the two phases. Because the as-deposited films show relatively high sheet resistance, we suppose that these peaks are mostly the indication of V_2O_5 phase (high resistance phase [39, 40]). Therefore, while the peaks at 301 and 403 cm^{-1} were attributed to V_6O_{13} , the others at $280, 285, 400, 405$ and 410 cm^{-1} were attributed to V_2O_5 . These peaks represent the bending and stretching vibrations (internal modes) of V-O bonds [53, 59]. The peak at 520 cm^{-1} is common across all spectra and indicates silicon peak resulting from the substrate. Moreover, the broad peak lying between $\sim 920\text{-}1000 \text{ cm}^{-1}$ is obviously caused by the substrate as well. The intensity of this peak changes with film deposition and annealing; suggesting new phases may appear and disappear in the spectra. However, these phases could not be identified. After annealing at 200°C , all peak intensities decrease and some peaks disappear. The spectrum includes only the VO_2 peak at 140 cm^{-1} and the broad peak at $\sim 301 \text{ cm}^{-1}$. By annealing at 300°C new peaks appear in the spectrum. The peaks at 820 and 826 cm^{-1} were attributed to VO_2 phase. The peaks at $158, 167$ relate to external mode whereas $834, 873$ relate to internal modes of V_6O_{13} phase. The

peak located at 292 cm^{-1} was attributed to V_2O_3 phase [58, 53]. The surface occurrence of VO_x phases influence the overall electrical properties of the films. Therefore, XPS measurements were also carried out in order to obtain additional information about the phase content of the films.

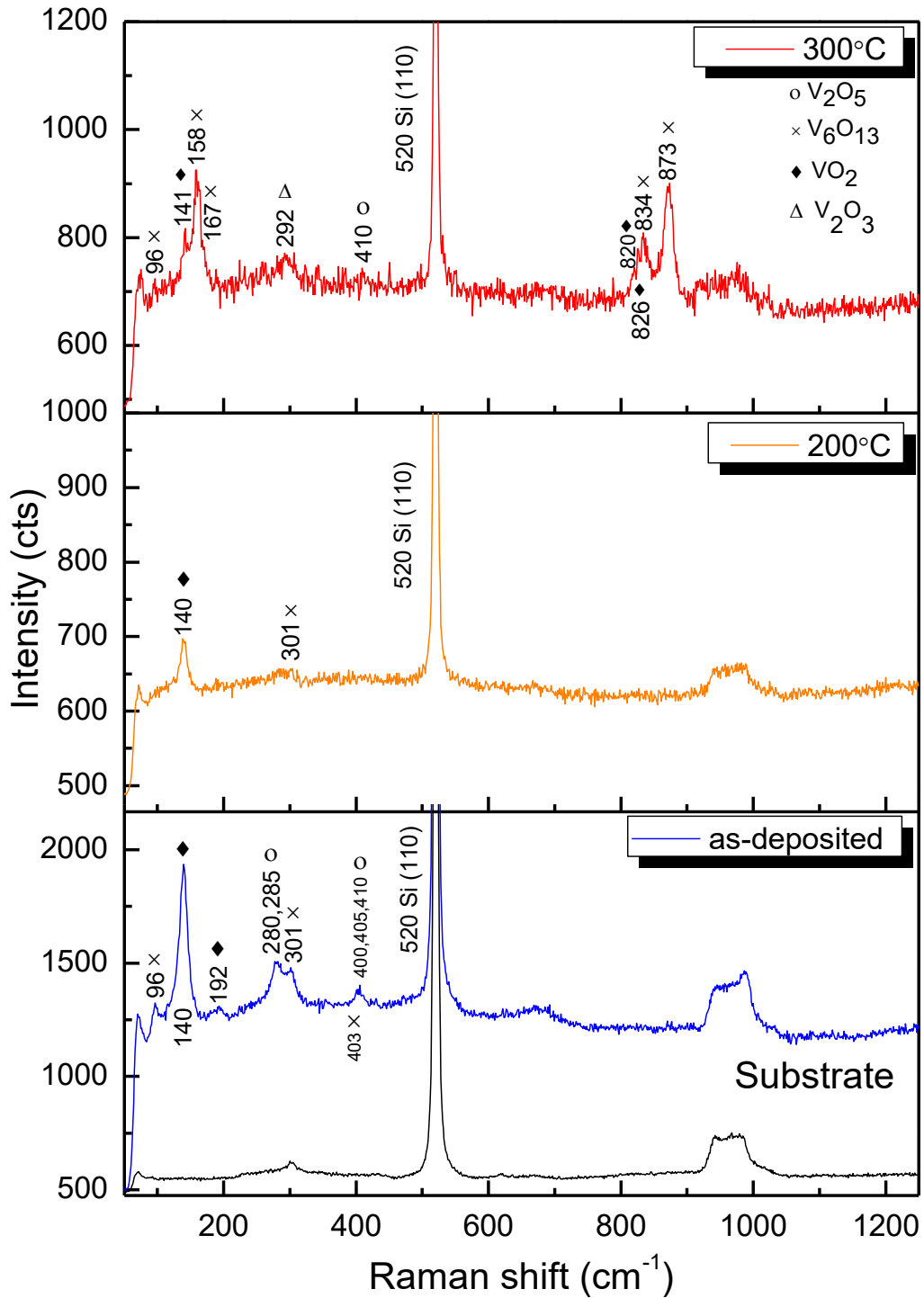


Figure 3.10. Raman spectra of substrate, as-deposited, 200°C and 300°C annealed films

3.2.3. X-Ray photoelectron spectroscopy results

Figure 3.11 shows the XPS spectra of the as-deposited and the annealed films. The spectra were obtained by deconvoluting the V2p and O1s energy levels. For this aim, XPS peak 4.1 software was used. The corresponding fitting parameters were given in Table 3.2. The spectra were calibrated according to the C1s peak located at ~ 284.8 eV. Shirley background was subtracted from all spectra. Due to spin-orbit splitting, V2p energy level consists of V2p_{1/2} and V2p_{3/2} sub-levels. They are found in close binding energies in the spectrum, so their peak extensions have some influence on each other. In addition, O1s energy level is also located very close to these energy levels. As a result, V2p_{1/2}, V2p_{3/2}, and O1s levels were included in one spectrum for accurate peak fitting and background subtraction procedures. Other details of the measurement were given in section 2.2.2.2. Compared to V2p_{1/2} peak, V2p_{3/2} has higher intensity, so mainly V2p_{3/2} peak was preferred to achieve the valence state determination more precisely. XPS is a surface sensitive technique, and its analytical depth is up to ~ 10 nm [66]. Ion etching of sample surface can be used to determine inner structure of the films by XPS; however, in this case, change in the oxidation state will occur due to the preferential etching of oxygen atoms. Therefore, ion etching was not preferred in our case.

The O1s peak deconvolution yields three components associated with oxygen in the as-deposited film (see Figure 3.11). The first one results from V-O bond and demonstrates VO_x formation. It is located at 530.2 eV. The second and the third components are located at 531.4 and 532.9 eV and were attributed to adsorbed oxygen and water [54, 67]. The adsorbed water component disappears in annealed films while other two components were also marked in the spectra. Furthermore, satellite peaks are needed to be introduced into XPS spectrum for a precise peak fitting, especially when the spectrum includes +4 and lower valence states. The satellite peaks are marked on the acquired spectra, and their fitting parameters are given in Table 3.3. Two of these satellites are found between V2p_{1/2} and O1s peaks, and one is found on the high binding energy side of the main oxygen peak located at 530.4 eV [54, 68].

The V2p_{3/2} peak was fitted into its components to determine the valence states of vanadium (see Figure 3.11). The results represent that all spectra contain V⁺⁴ and

V^{+5} valance states which are the indication of VO_2 and V_2O_5 phases, respectively. The V_2O_5 phase grows on film surface via surface oxidation and can be easily detected by XPS. In the as-deposited film, V^{+4} and V^{+5} peaks are located at binding energies of ~ 517.0 and 516.1 eV, respectively. These values are consistent with the values reported in previous works [69, 67]. The peak located at ~ 514.3 eV could not be attributed to any valance state of stoichiometric vanadium oxides. Thus, we concluded that this peak arises from non-stoichiometric phases which are present in valances between +2 and +3. After annealing at 200°C , this peak disappears suggesting that it transforms into an oxide phase with a higher valance state such that the presence of only V^{+4} and V^{+5} peaks at 200°C confirms that there is no phase with valance state lower than V^{+4} . The relative concentration of the phases calculated by dividing relevant valance peak area into the total area of the $V2p_{3/2}$ peak. The results were presented as area percentage inside the spectra (Figure 3.11). They reflect that VO_2 phase is dominant in the as-deposited and the 200°C annealed film. This can also be observed from the corresponding Raman spectra. The Raman peaks of VO_2 phase have higher intensities in comparison with other characteristic peaks in these spectra. After annealing at 300°C relative amounts of VO_2 and V_2O_5 phases change to 27% and 73%, respectively. Moreover, the peak FWHM of V_2O_5 become broader than VO_2 phase which normally must be the reverse because the core hole-3d electron interaction in electron configuration of V^{+4} state gives rise to a broader peak structure. This suggests that the broad V^{+5} peak may be caused by V_6O_{13} phase included within the peak structure. The corresponding Raman result also shows that the film includes V_6O_{13} phase [69].

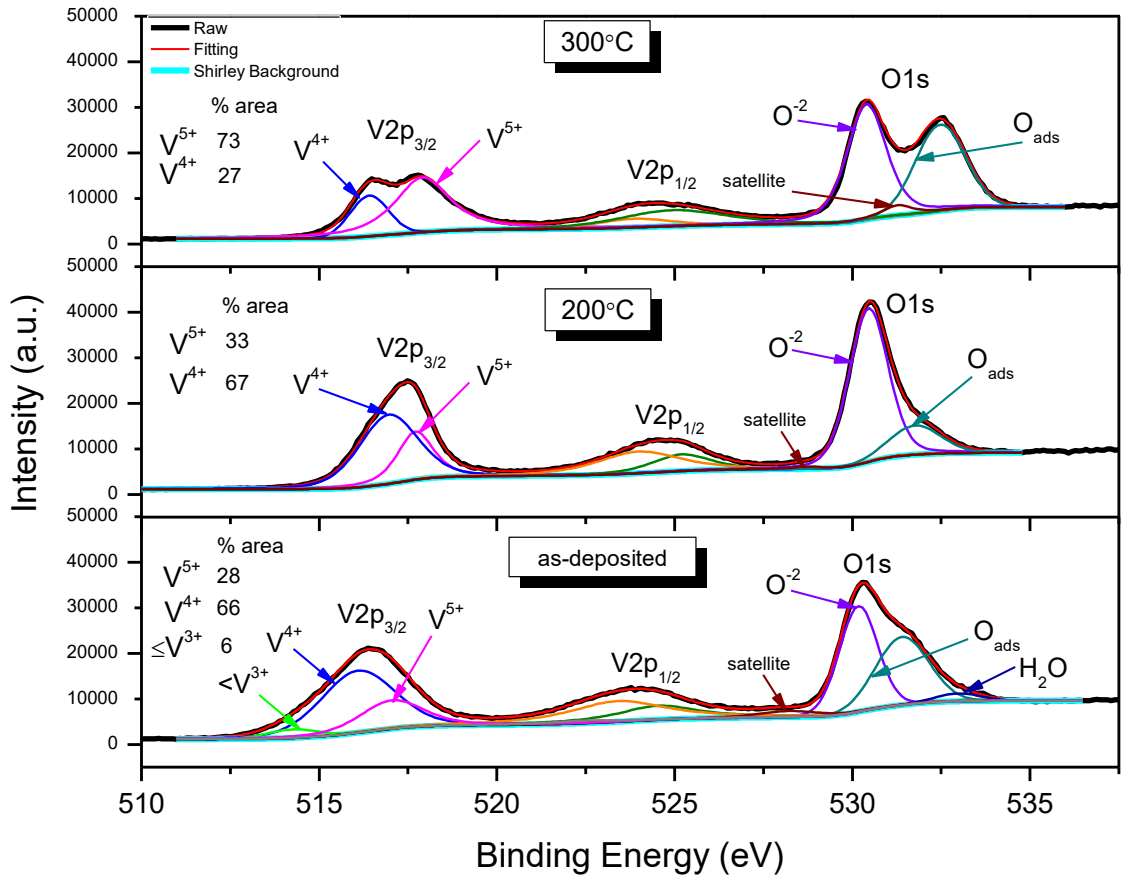


Figure 3.11. XPS spectra of as-deposited, 200°C and 300°C annealed films

Table 3.2. Fitting parameters of vanadium and oxygen peaks observed in the spectra

Sample	Valance state	V2p _{3/2}				V2p _{1/2}			
		BE (eV)	FWHM (eV)	%L-G	Area (cts-eV/s)	BE (eV)	FWHM	%L-G	Area (cts-eV/s)
As-deposited	V ⁵⁺	517.0	2.1	40	16616	524.5	2.7	91	12641
	V ⁴⁺	516.1	2.4	19	38512	523.4	3.2	80	21386
	<V ³⁺	514.3	1.7	0	3280	522.4	2.2	80	1772
200°C	V ⁵⁺	517.7	1.2	56	17109	525.2	2.0	50	9524
	V ⁴⁺	516.9	1.9	28	35440	523.9	2.8	57	17962
300°C	V ⁵⁺	517.9	1.8	78	32243	524.9	3.6	38	15725
	V ⁴⁺	516.4	1.3	0	12085	523.9	2.5	33	5829
Sample		O1s							
		BE (eV)	FWHM (eV)	%L-G		Area (cts-eV/s)			
As-deposited		530.2	1.3	5		32134			
		531.4	1.8	1		28080			
		532.9	1.5	0		2691			
200°C		530.5	1.3	20		50506			
		531.8	1.7	9		12014			
300°C		530.4	1.3	41		42258			
		532.5	1.7	0		33297			

Table 3.3. *Fitting parameters of the satellite peaks observed in the spectra*

Sample	Satellite Peaks			
	BE (eV)	FWHM (eV)	%L-G	Area (cts-eV/s)
As-deposited	528.2	2	49	3510
200°C	528.7	1	80	752
300°C	531.3	1	80	3339

3.2.4. Transmission electron microscopy results

3.2.4.1. Selected area electron diffraction (SAED) patterns

Figure 3.12a shows the SAED pattern of the substrate. The pattern consists of the diffuse rings indicating the amorphous characteristic of the substrate. On the other hand, the as-deposited film, in Figure 3.12b, consists of diffraction rings with diffraction spots on them. This reflects the polycrystalline nature of the film. After annealing at 200°C, the rings lose their sharpness and some of the faint rings disappear (see Figure 3.13a). These are indications of the decreased crystal size and crystallinity of the film. The film annealed at 300°C reaches the highest crystal size and crystallinity among all: the rings become sharper and the additional rings appear in the SAED pattern with more spots showing up on them (see Figure 3.13b). For phase analysis from the patterns, the radii of the rings were measured and the interplanar spacings (d) were calculated to match them with the PDFs. VO_x has many stoichiometric and non-stoichiometric phases, and the interplanar spacings of these phases are very close to each other. For this reason, some VO_x phases were determined as candidates based on the XRD, Raman and XPS results. These phases are VO₂, V₂O₃, V₆O₁₃, V₃O₇, and V₂O₅. The d values and intensities of these phases were presented in Table 3.4. In the SAED pattern of as-deposited film, the higher d values measured at 0.244 nm, 0.217 nm, 0.149 nm, 0.136 and 0.124 nm match with more than one phase, the lower ones located at 0.105 nm, 0.094 nm and 0.087 nm do not match any of the candidate phases. These lower values may correspond to platinum or non-stoichiometric phases of VO_x. The d values were also measured for the films annealed at 200°C and 300°C. Analogous to diffraction rings located at 0.224 nm, 0.217 nm, and 0.149 nm in the as-deposited film, the 200°C annealed film has also the diffraction rings very close to these values. These are located at 0.243 nm, 0.214 nm and, 0.141 nm and obviously are the same diffraction rings. According

to Raman and XPS results, we believe that these values mainly reflect the VO₂ and V₂O₅ phases. The value of 1.54 nm of the as-deposited film is possible to be matched with V₂O₃, V₆O₁₃, and V₂O₅ phases. When we look at the SAED pattern of 300°C annealed film, the values of 0.241 nm, 0.213 nm, 0.142 nm, 0.136 nm, 0.107 nm, 0.096 nm and 0.087 nm match up well with those of the as-deposited and the 200°C annealed film. In addition, some new values appear at 0.319 nm, 0.194 nm, 1.67 nm, and 0.114 nm in the pattern. Consequently, the phase analysis of the 300°C annealed film shows the mixed phase structure including VO₂ and V₂O₅, in accordance with XRD, Raman and XPS results.

Table 3.4. Interplanar spacing values ($d(\text{Å})$) of some VO_x phases from PDFs; in order to compare with $d(\text{Å})$ values measured from electron diffraction patterns of the as-deposited, 200°C and 300°C annealed films

V ₂ O ₃ -Monoclinic PDF#00-039-0774		VO ₂ -Monoclinic PDF#00-009-0142		V ₃ O ₇ -Monoclinic PDF#00-027-0940		V ₆ O ₁₃ -Monoclinic PDF#00-027-1318		V ₂ O ₅ -Orthorhombic PDF#00-003-0207	
d (Å)	Intensity	d (Å)	Intensity	d (Å)	Intensity	d (Å)	Intensity	d (Å)	Intensity
3.18	100	3.2	100	3.49	40	3.51	100	3.41	80
2.7	50	2.68	30	2.71	10	2.67	80	2.61	50
2.42	90	2.43	40	2.55	80	2.48	20	2.51	10
2.13	50	2.14	50	2.46	60	1.99	60	2.18	80
2.09	20	2.04	10	2.18	40	1.66	10	2.04	20
1.65	90	1.87	40	2.08	10	1.54	80	1.92	60
1.53	10	1.66	30	1.93	10	1.35	80	1.65	50
1.34	50			1.68	20	1.24	10	1.49	80
								1.36	60
								1.23	60
Measured Interplanar spacings (Å) from diffraction patterns									
As-deposited film			200°C annealed film			300°C annealed film			
	2.44			2.43				3.19	
	2.17			2.14				2.41	
	1.49			1.54				2.13	
	1.36			1.41				2.07	
	1.24			—				1.94	
	1.05			—				1.67	
	0.94			—				1.42	
	0.87			—				1.36	
	—			—				1.14	
	—			—				1.07	
	—			—				0.96	
	—			—				0.87	
The values with same colours are very close and suggest same diffraction rings on the three diffraction pattern.									

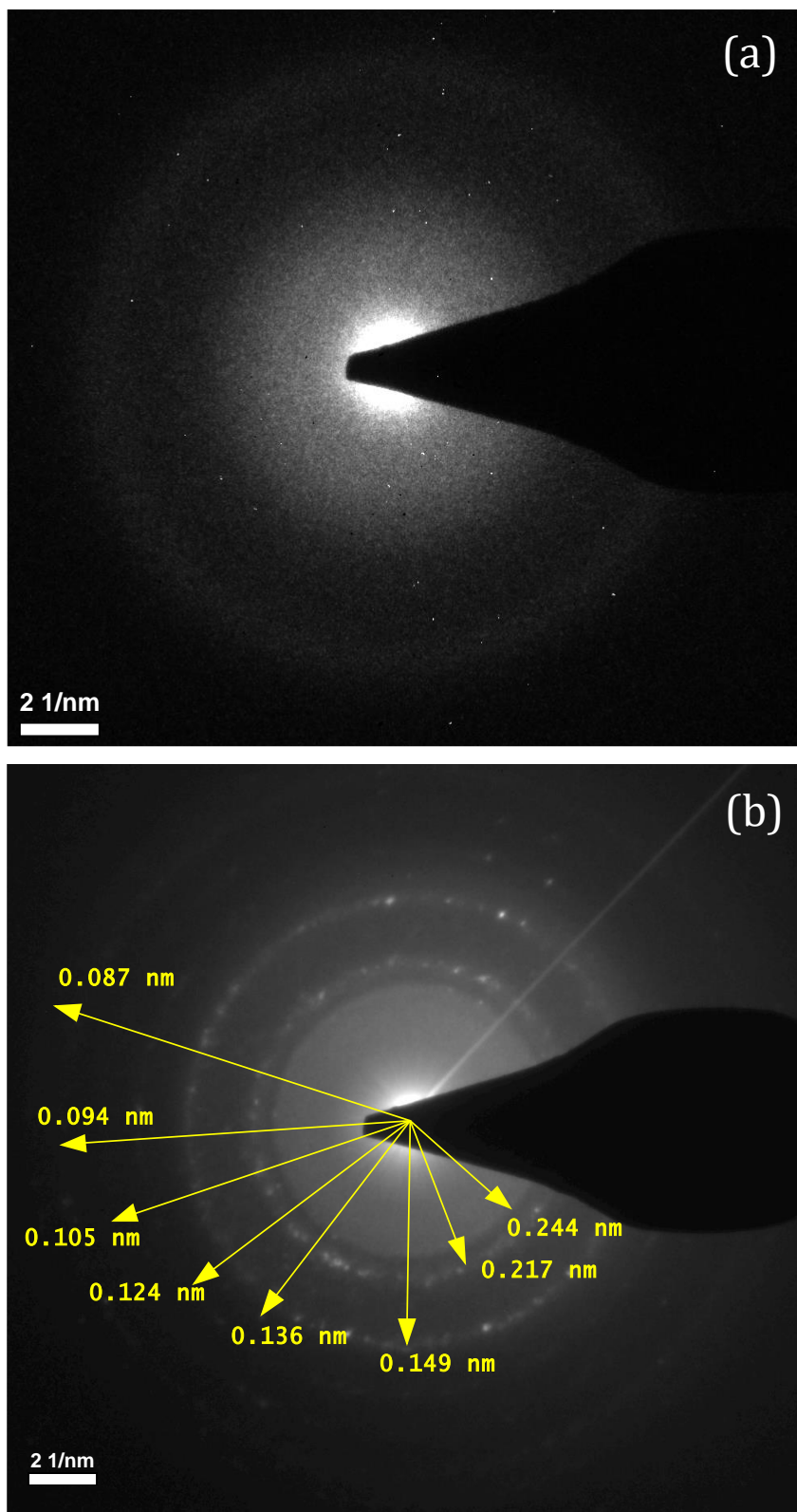


Figure 3.12. SAED patterns of a) substrate and b) as-deposited film

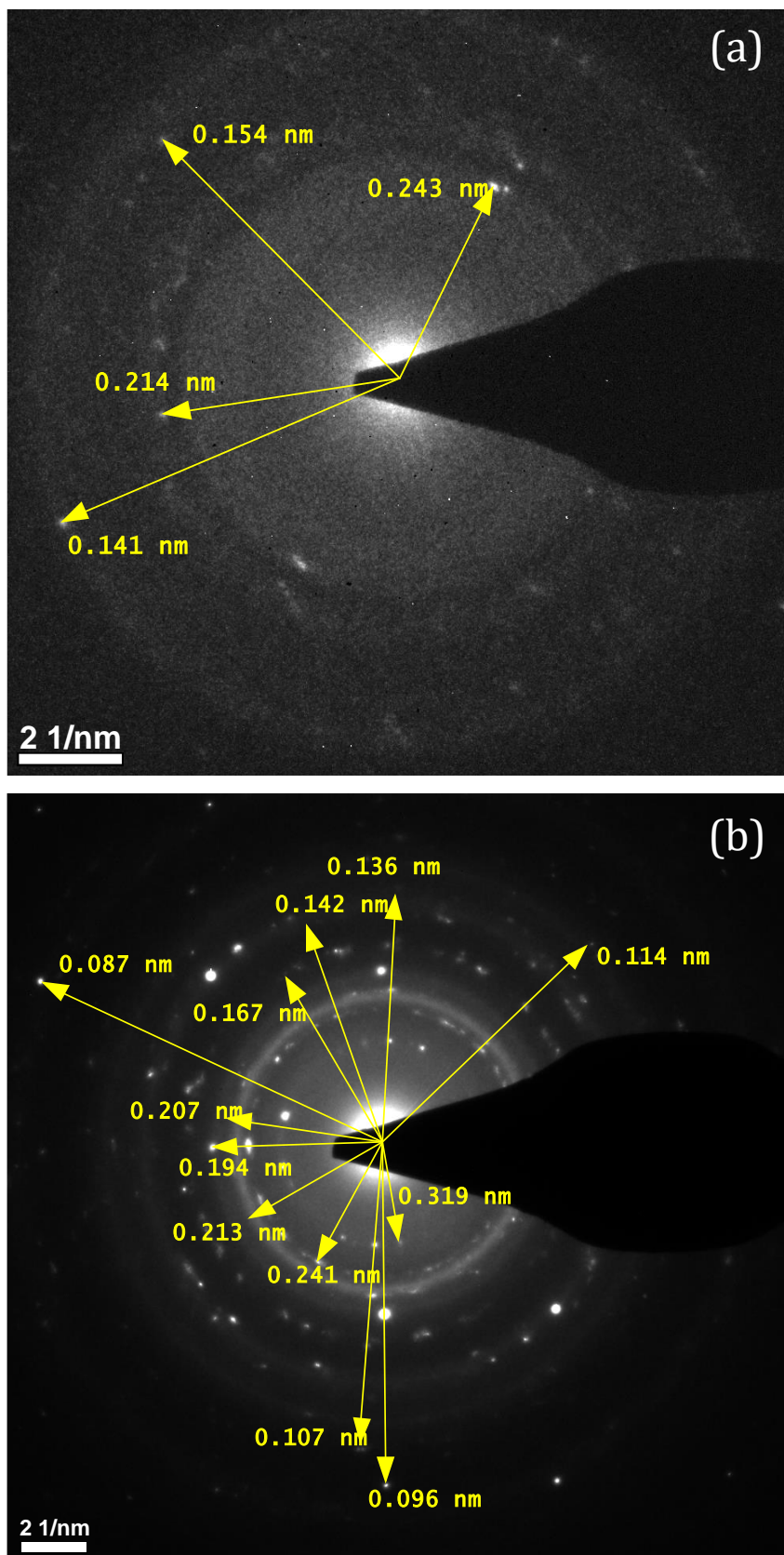


Figure 3.13. SAED patterns of a) 200°C and b) 300°C annealed films

3.2.4.2. Transmission electron microscopy images

Figure 3.14 shows the BF and DF images of the as-deposited film. Throughout the film, the dark regions in the BF image and the bright regions in the DF image are evidence of crystal grains. The white spots are seen in the BF image also appear in the films annealed at 200°C and 300°C. These spots reflect the pores in the film as it is demonstrated in elemental mapping analyzes (see section 3.2.4.3). Crystal size approximately ranges from several nm to about 20 nm throughout the film.

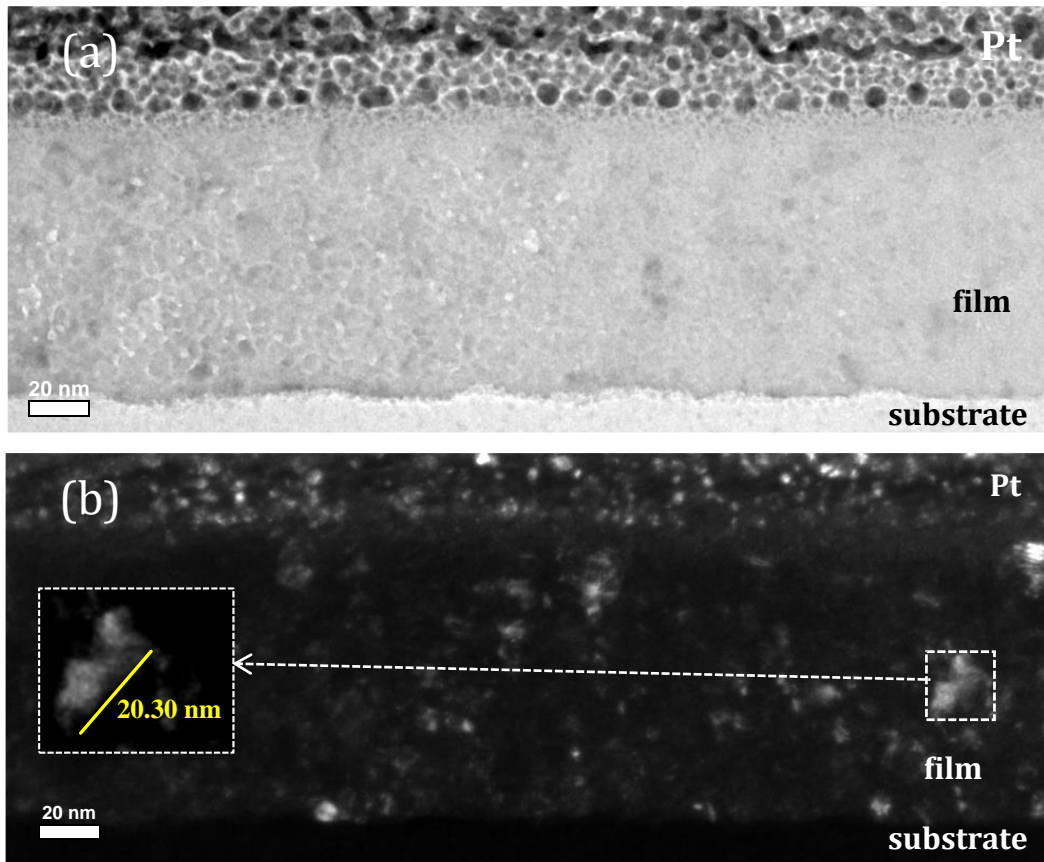


Figure 3.14. TEM images of the as-deposited film: a) BF, b) DF

The HRTEM images in Figure 3.15 show some of the crystalline regions. The interplanar spacings were measured from these visible crystals. With the support of Raman and XPS results, these crystals would belong to VO_2 and V_2O_5 or, moreover, V_2O_3 and V_6O_{13} . In this case, making a definite identification is not simple. Nevertheless, when we consider the Raman and XPS results, these can be an illustration of VO_2 and V_2O_5 crystals.

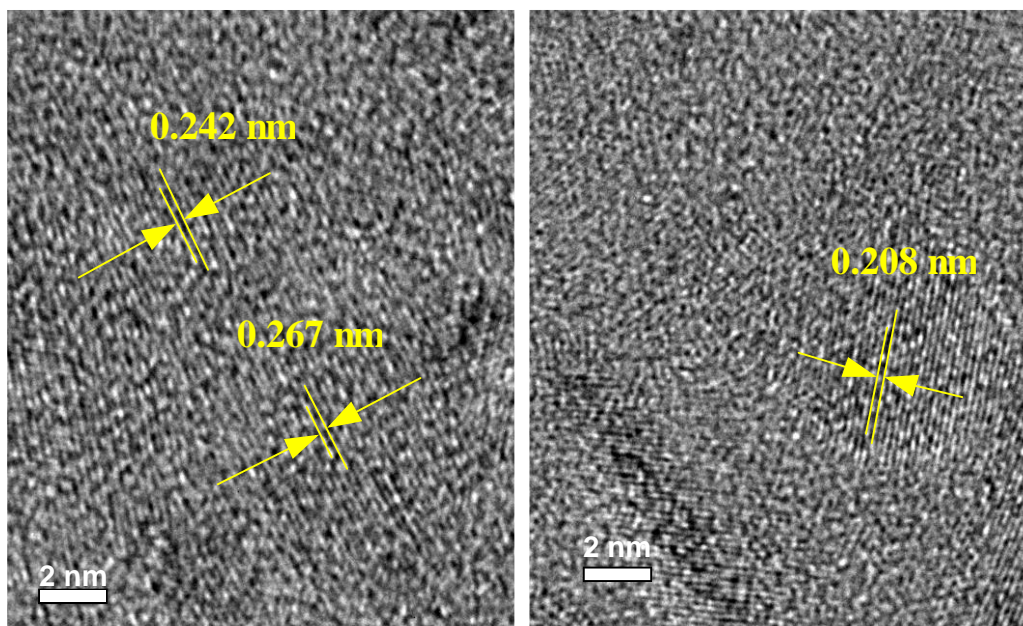


Figure 3.15. HRTEM images of the as-deposited film showing the crystal regions with measured interplanar spacings

As the BF image of the 200°C annealed film is examined, we can not see crystal regions clearly (see Figure 3.16). The HRTEM image proves the existence of small crystals (see Figure 3.17) reaching up to ~7 nm.

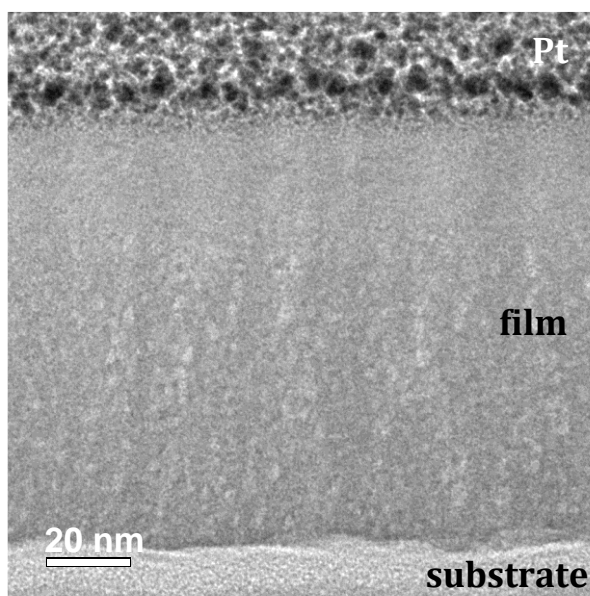


Figure 3.16. BF image of the 200°C annealed film

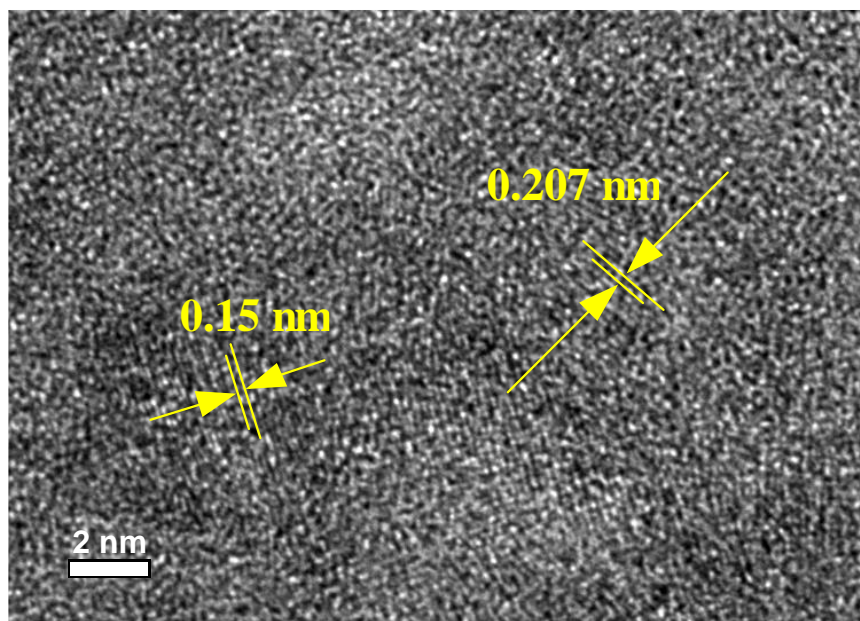


Figure 3.17. HRTEM image of the 200°C annealed film showing the crystal regions with measured interplanar spacings

The BF image of the 300°C annealed film (Figure 3.18) supports the corresponding SAED pattern. Very large crystal grains which reach ~80 nm in size are observed in the film (see the DF image in Figure 3.19a). The HRTEM images, in Figure 3.19b and c, clearly show the film's large crystals. The interplanar spacings measured via these images match with more than one phase presented in Table 3.4. The BF image shows that the white spots which illustrate the film pores also become larger.

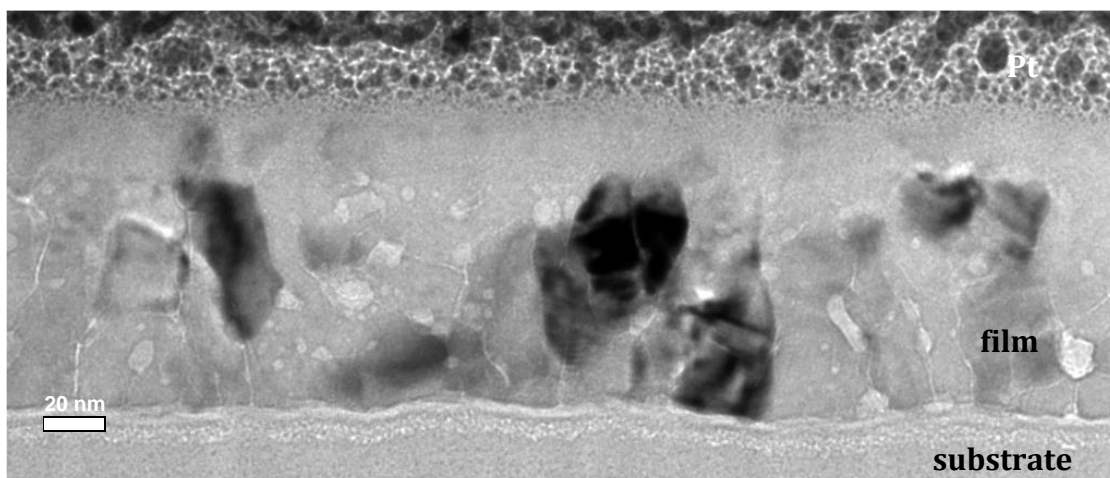


Figure 3.18. BF image of the 300°C annealed film

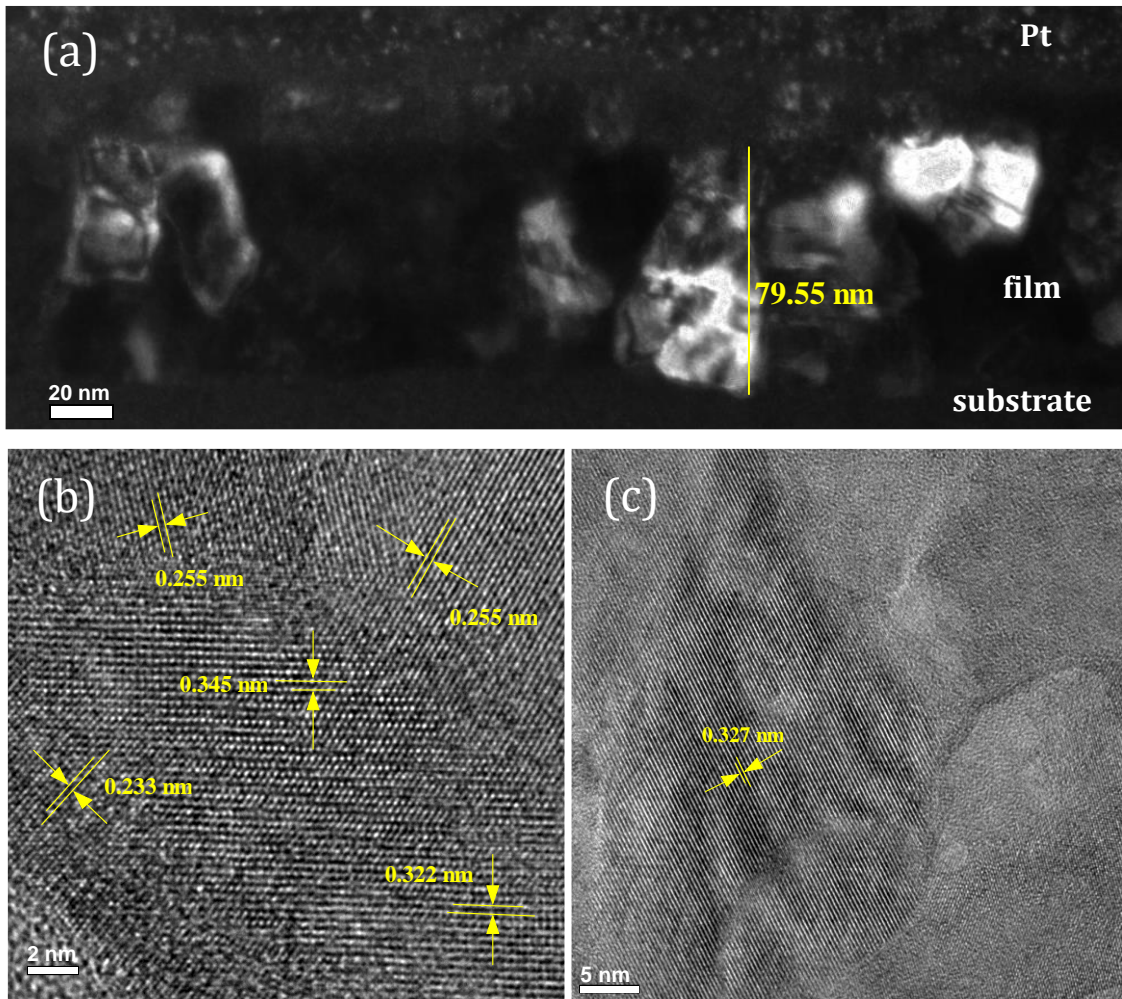


Figure 3.19. TEM images of the 300°C annealed film: a) DF image b,c) HRTEM images showing the crystal regions with the measured interplanar spacings

3.2.4.3. Elemental mapping

Elemental mapping was used to unveil porous structure of the films. The details of the ESI experiments were given in section 2.2.2.4. The cross-sectional images showing vanadium, oxygen and nitrogen maps of the as-deposited film are presented in Figure 3.20a, b, and c respectively. The nitrogen map shows that the film does not include any nitrogen element. Nitrogen exists only in the substrate as it is expected. In addition, vanadium and oxygen maps show that the film consists of only vanadium and oxygen elements which are uniformly distributed along the film. This supports the VO_x formation in the film. The dark spots in the vanadium and oxygen maps are the regions which are lacking in vanadium and oxygen elements. Therefore, they demonstrate the formation of pores inside the film.

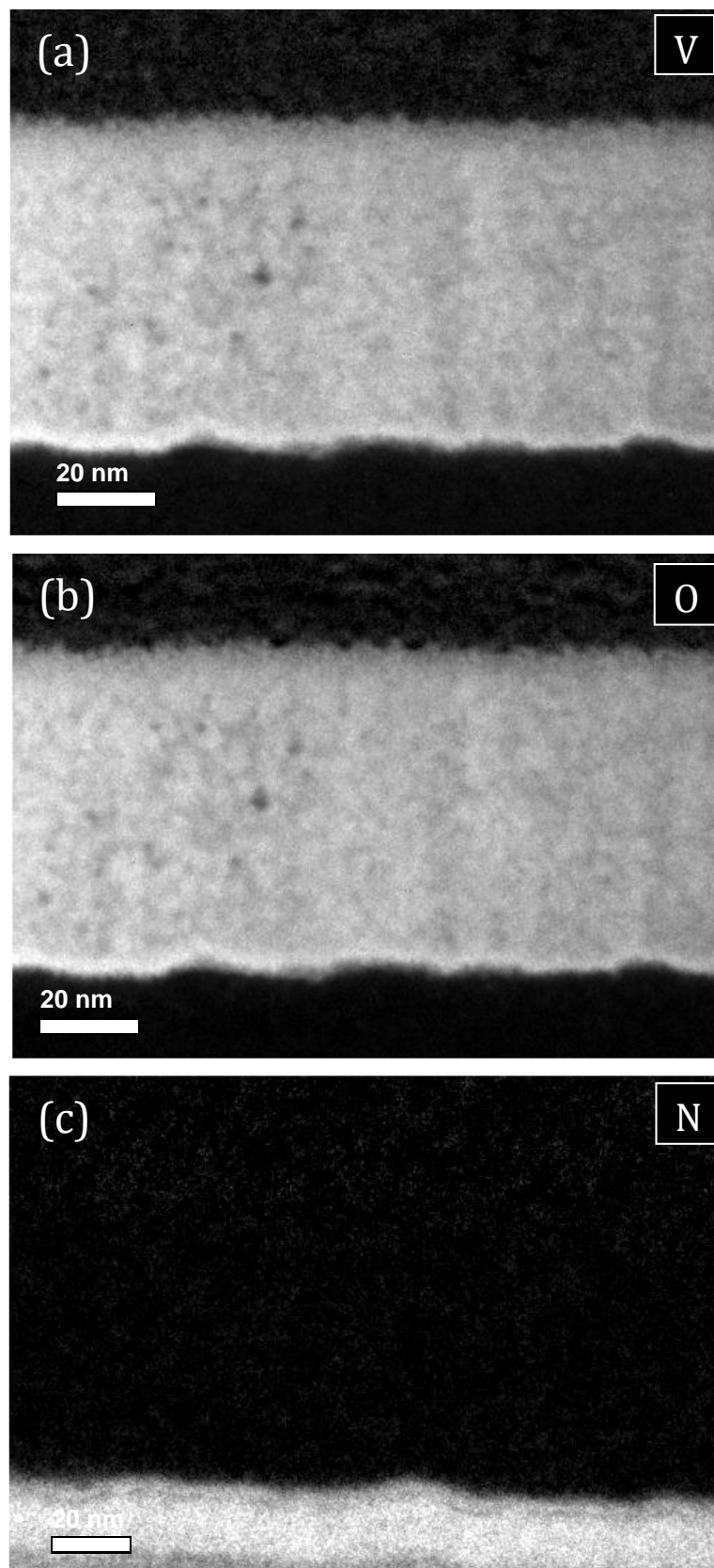


Figure 3.20. Cross-sectional elemental maps of the as-deposited film: a) vanadium b) oxygen c) nitrogen

From the vanadium and oxygen maps of the 200°C annealed film in Figure 3.21a and b, one can see that the vanadium and oxygen maps do not coincide in terms of the dark spots they have (Figure 3.22 shows that the film does not include any nitrogen). In the oxygen map, the spots are clearly seen and homogeneously distributed through the film. In the vanadium map, the corresponding sites appear to be occupied by vanadium (we also assume that vanadium exists together with oxygen as mentioned in section 2.2.2.4). However, the vanadium map still includes indistinct dark spots when examined at a close range. In order to support the existence of pores inside the film, the high angle annular dark field (HAADF) image was presented in Figure 3.23.

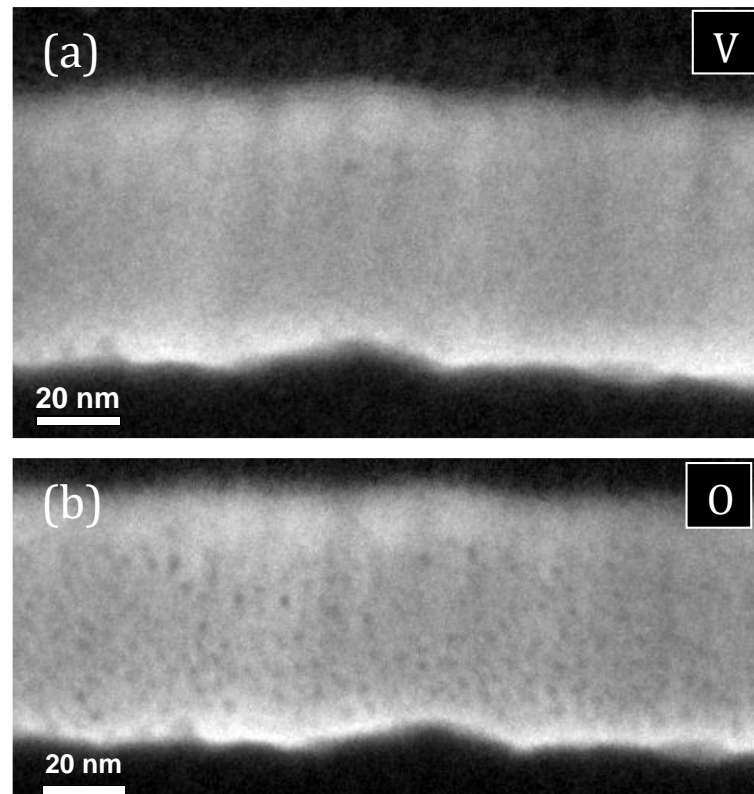


Figure 3.21. Cross-sectional elemental maps of the 200°C annealed film a) vanadium and b) oxygen

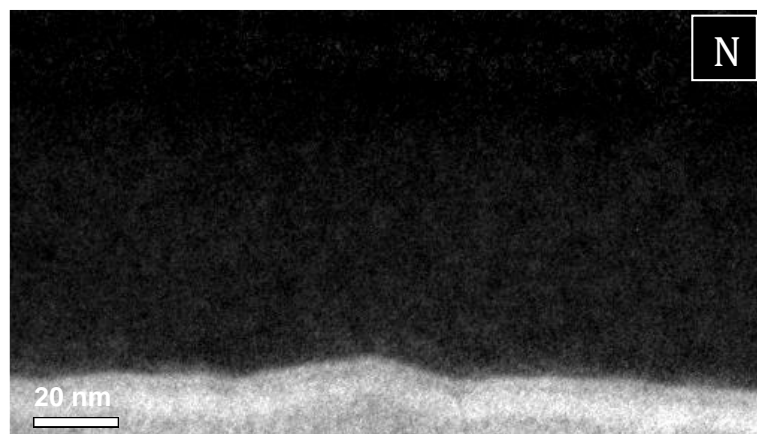


Figure 3.22. Cross-sectional nitrogen map of the 200°C annealed film

The high angle annular dark field image (HAADF) relies on atomic number (Z contrast). Therefore, while the bright regions show the VO_x compound which constitutes the film, the black regions show the pores. This image is in accordance with the oxygen map and the BF image of the film.

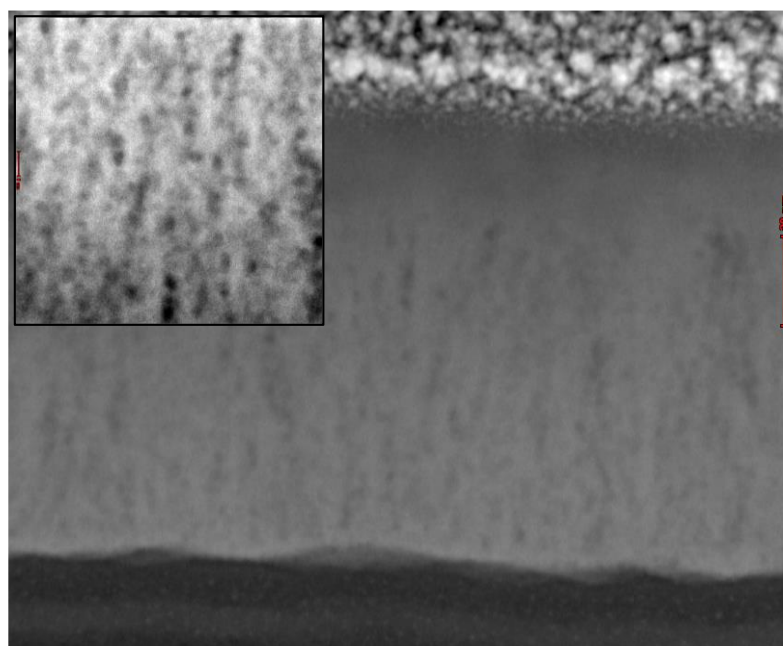


Figure 3.23. High angle annular dark field (HAADF) image of the 200°C annealed film. The inset image shows a magnified image.

After annealing at 300°C, the pores reach their largest sizes. The vanadium and oxygen maps clearly show the regions which are deprived of vanadium and oxygen. The film does not include any nitrogen element (see Figure 3.24a, b, and c).

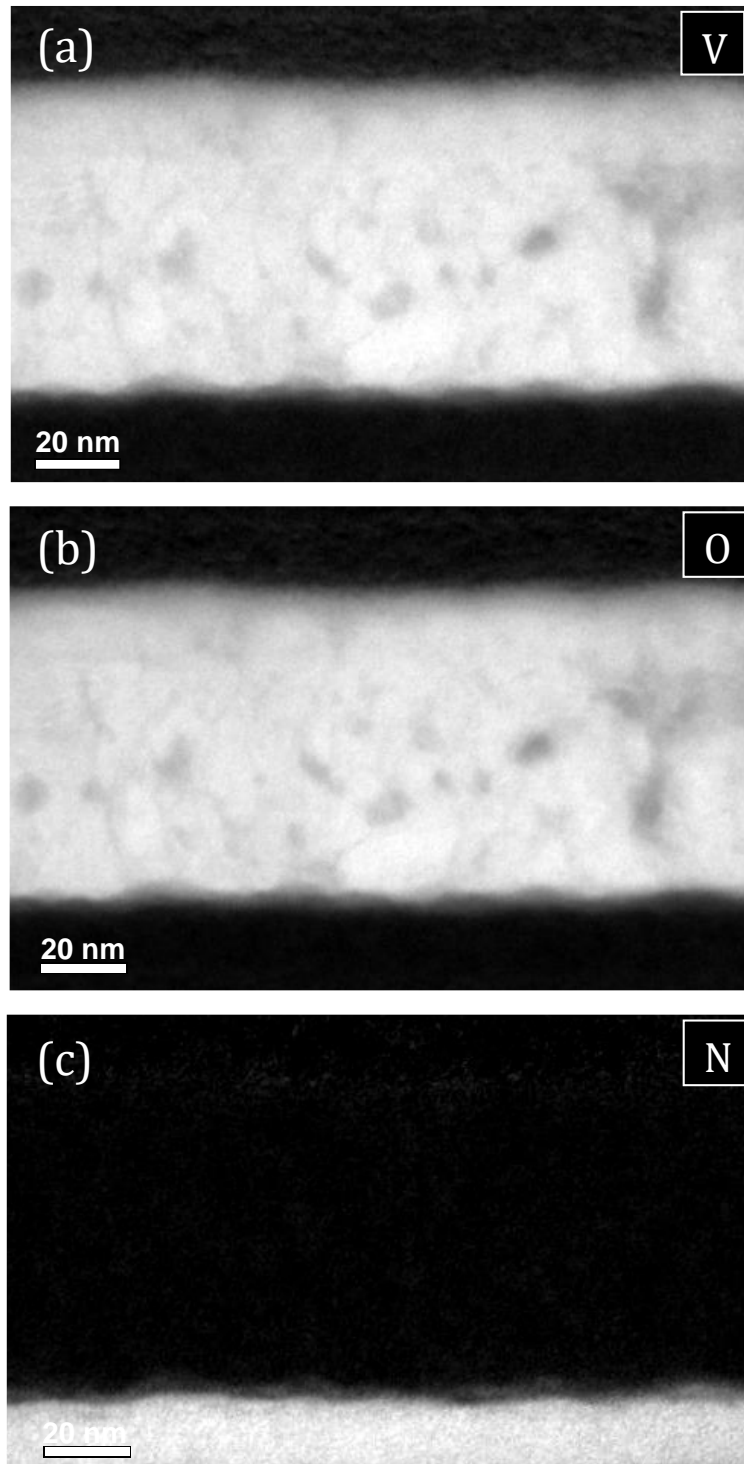


Figure 3.24. Cross-sectional elemental maps of the 300°C annealed film: a) vanadium b) oxygen c) nitrogen

3.2.4.4. Pore size distribution study of the films

To understand how pore size and distribution changes through the films, the histograms of pore area distribution were created. This is achieved by the image processing the vanadium and oxygen maps of the as-deposited, 200°C, and 300°C

annealed films. ImageJ software was used for the processing. Firstly, a region of interest was chosen and cropped. Then, the images were filtered by a bandpass filter. Afterwards, thresholding was applied to determine pore areas. Finally, the pore areas were measured via particle size analysis. By doing this, very small pore areas, which may illustrate noise in the image instead of pore area, were excluded by applying a mask. The procedure was illustrated on the vanadium and oxygen maps of the as-deposited film in Figure 3.25.

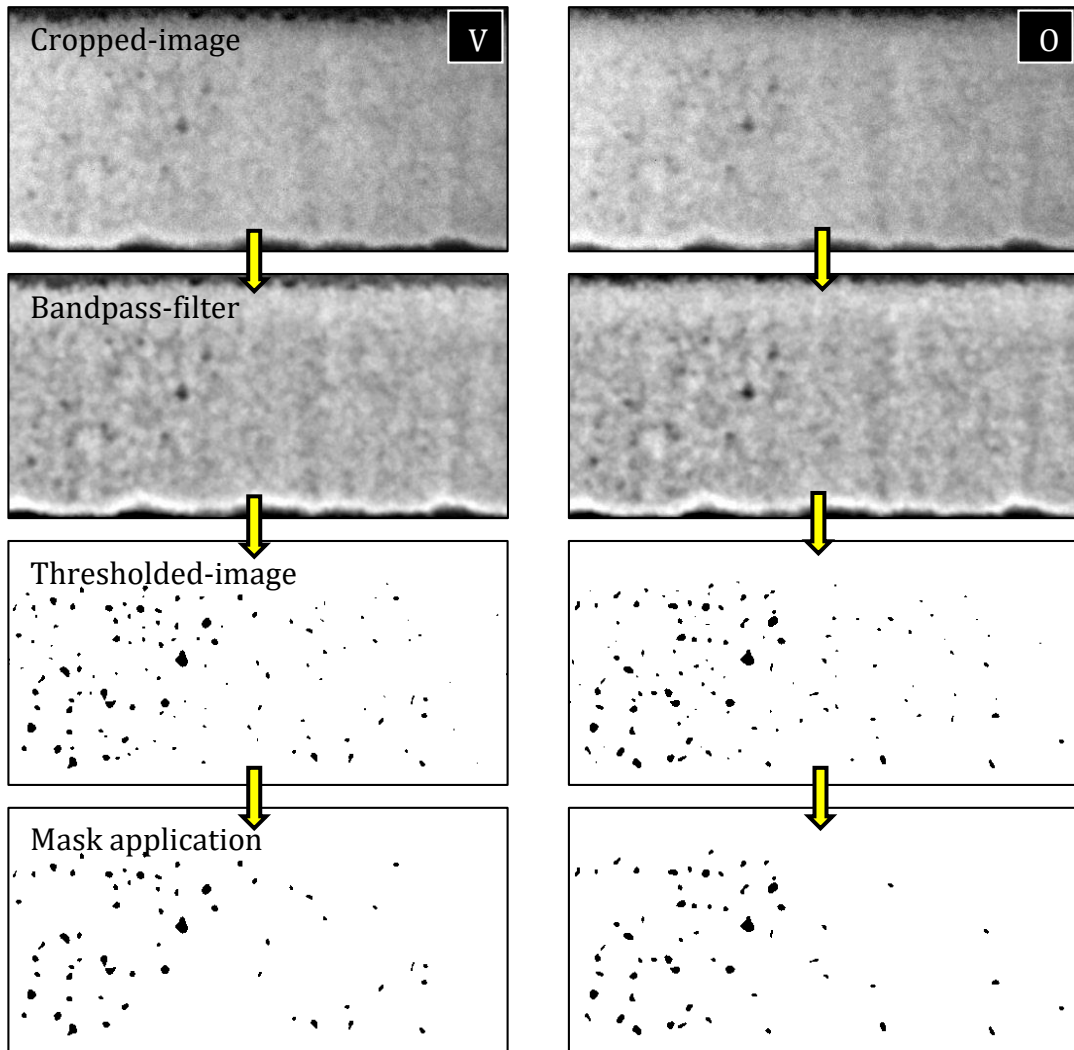


Figure 3.25. Pore area determination steps: The image processing of the as-deposited film was given as an example

Pore area determination steps were shown in Figure 3.25 as an example for the as-deposited film. The obtained histograms showing pore area distribution through the films were given in Figure 3.26 and Figure 3.27. These histograms were created by processing the elemental maps of vanadium and oxygen, respectively.

Pore area was used instead of pore diameter because pores are not spherical in shape. The counts along the vertical axes of the histograms could be used to interpret the amount of the pores. The data obtained from vanadium maps in Figure 3.26 and Figure 3.27 show that; after annealing at 200°C, the intensity of the columns decreases somewhat and the distribution becomes slightly narrower. This suggests a reduction in pore amount and pore size, respectively. At 300°C, pore area demonstrates a wide distribution. This suggests that pores become much larger than those present in as-deposited film after annealing at 200°C. The histograms obtained from oxygen maps show almost the same trend as well. The pore size and pore amount decrease slightly from the as-deposited to the 200°C annealed film. Although a decrease occurs in the amount of the smaller pores, the distribution indicates that large pores appear in the 300°C annealed film.

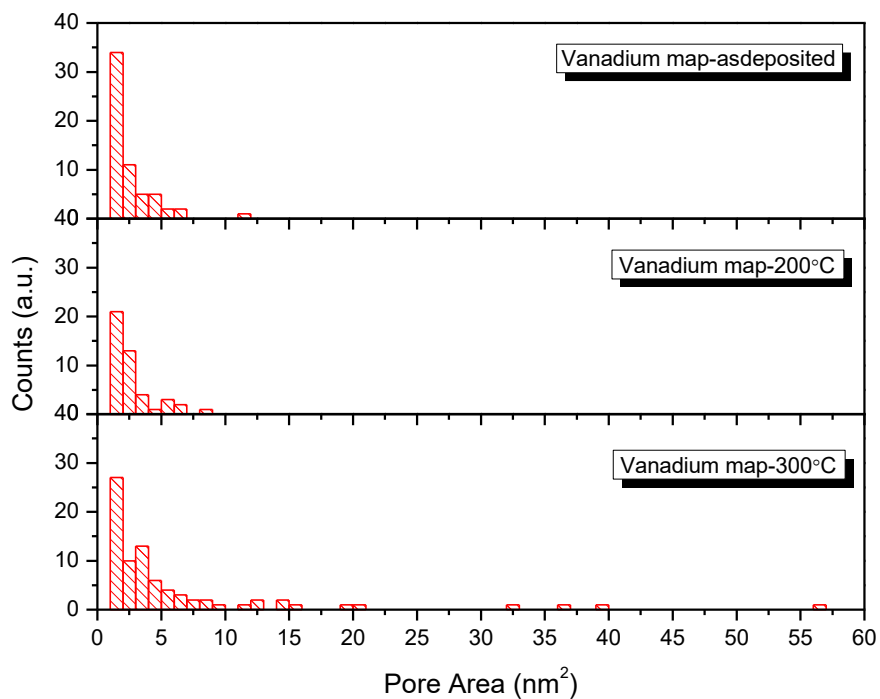


Figure 3.26. Pore area distribution histograms extracted from the vanadium maps

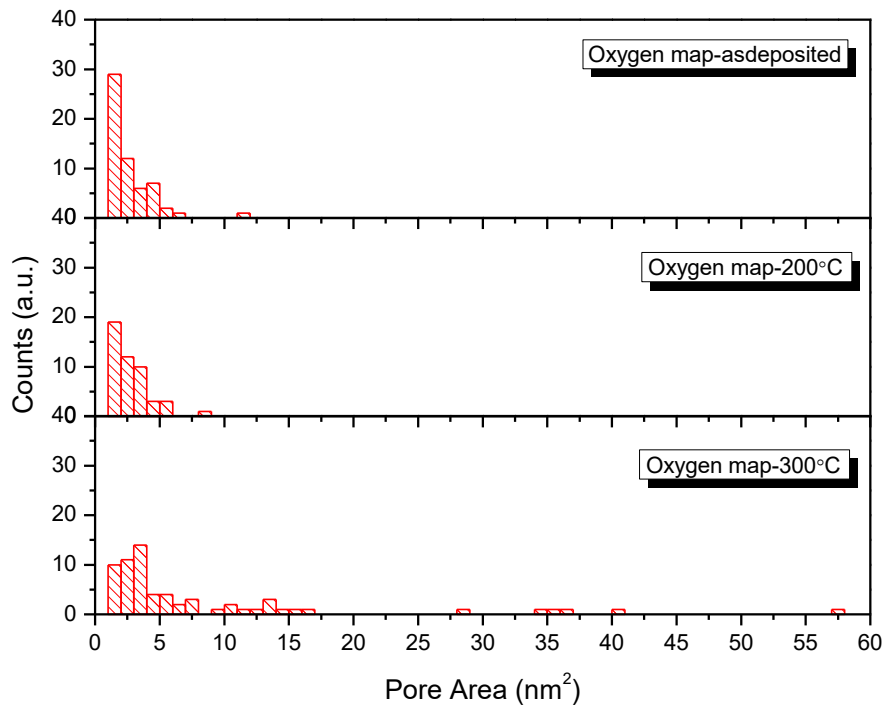


Figure 3.27. Pore area distribution histograms extracted from the oxygen maps

4. DISCUSSION

In this study, VO_x thin films were deposited by PDC-RMS technique and post-annealing procedures were applied to the as-deposited films at 200°C and 300°C in the N₂ ambient for 3 hours. In order to investigate the correlation between structural and electrical properties, various characterization techniques were used.

The sheet resistance values of the as-deposited films deposited in this study are in agreement with the sheet resistance value of as-deposited film produced in the previous study (see Table 1.1 and Table 3.1): According to our experience in film fabrication, the near 100kΩ difference between sheet resistances of the as-deposited films of two studies may be attributed to the altering sputtering system conditions after system maintenance or altering of the probes in FPP system. Therefore, we could repeat the electrical resistance value of the film, grown in as-deposited film condition. Moreover, we also applied the same post-annealing procedures to the as-deposited films with the previous study to constitute the films annealed at 200°C and 300°C. Thus, the properties of the films in this study also reflect the properties of the films from the previous study. With this approach, we used the 1/f noise values from the previous study to associate with the structural results obtained in the current study.

The structural characterization of the films revealed that all films exhibited nanocrystalline structure in varying crystallinity and grain size. They also showed porous structure; this was verified with the elemental mapping in TEM. Eventhough the XRD pattern of the as-deposited film did not show any characteristic peak indicating the presence of any crystal grain, the TEM results demonstrated the nanocrystalline structure of the film with fine grains (up to ~20 nm, see Figure 3.14b). In addition to this, the existence of pores within the film was also revealed. The corresponding BF image and the elemental maps of vanadium and oxygen illustrated that pores do not have a regular distribution throughout the film. This inhomogeneity may have a potential to alter film properties. Annealing of the as-deposited film at 200°C results in a decrease in grain size and crystallinity (the XRD pattern does not show characteristic peak). This film exhibits almost an amorphous characteristic; a few nanometer-sized crystals are distributed within the matrix. The pore size was also decreased slightly and showed a more regular distribution

throughout the film. This distribution could be observed especially from the oxygen map of the 200°C annealed film in accordance with the BF image. After annealing of the as-deposited film at 300°C, crystallinity, pore and grain size increased significantly.

After annealing of the as-deposited film at 200°C and 300°C, the phase content of the films has been also changed. The formation of V_2O_5 and VO_2 phases on the surfaces of all films detected by XPS spectra. The Raman spectrum of the as-deposited film showed the existence of V_2O_5 and V_6O_{13} phases in addition to VO_2 . The high intensity Raman peak at 140 cm^{-1} and the area percentage of the V^{+4} peak in XPS are the evidence of VO_2 dominance in this film. The intensity of the VO_2 peak at 140 cm^{-1} was lowered after annealing at 200°C, along with other characteristic peaks. The very low crystallinity of the film conforms with this observation. The low intensity broad peak accompanying the VO_2 peak in the spectrum indicates the presence of other phases like V_2O_5 and V_6O_{13} in trace amounts. VO_2 phase is the dominant phase in this film, and this is consistent with the corresponding XPS spectrum. The insignificant hysteretic behaviours observed in $\ln R$ -versus-temperature curves of the 200°C annealed films is evidence of fine nano-sized VO_2 crystals. The combination of various phase analyses puts forward the mixed phase content of the 300°C annealed film. The phase constituents comprise low resistance phases like V_2O_3 and V_6O_{13} as well as VO_2 and V_2O_5 .

According to structural results we concluded that several structural factors are responsible for the electrical properties of the films. In the as-deposited film, appearance of the high resistance phase, which is V_2O_5 , together with VO_2 is one contribution to the resistance of the film, which is relatively high. These films showed a certain crystallinity with grain sizes up to $\sim 20\text{ nm}$. At this crystallinity, the grain boundary scattering of electrons can be one additional contribution to the resistance of the film. Moreover, the pores in the film would also serve as electron scattering centers which are another contribution. The sheet resistances of the as-deposited films were reduced by annealing at 200°C. This film contains very fine crystals (a few nanometers) within an amorphous matrix. In one study reported in the literature, R. H. Chen et. al. produced amorphous VO_x films with embedded VO_2 nanocrystals. The films were produced by long-throw DC reactive magnetron

sputtering system with the substrate temperature at 200°C. Post-annealing was applied to the films at 200, 250 and 300°C in the N₂ atmosphere for 30 minutes. The sheet resistance values changed from 230 kΩ/sq to 103 kΩ/sq, from as-deposited film to 250°C annealed film. They explained the conduction mechanism and resulting resistances of the films by charge hopping mechanism (similar to the Mott's localized states conductance) between VO₂ nanocrystals [70]. Analogous to this study, we obtained a similar film structure by annealing the as-deposited films at 200°C. In addition, a drop less than one and a half time on TCR values were observed after 200°C annealing of the as-deposited films eventhough room temperature sheet resistances decrease about four times. This is consistent with the finding of the relevent study and strengthens the attribution we have made. Consequently, the conduction mechanism in our 200°C annealed film can also be explained by charge hopping mechanism. Unlike the study of R. H. Chen et. al., we did not apply substrate heating during deposition and obtained higher TCR values with little higher sheet resistances. In addition, we explored the porous structure of the films. As demonstrated in the experimental results, the pore distribution becomes more homogeneous in the film annealed at 200°C in contrast to the as-deposited and the 300°C annealed films. Annealing of the as-deposited films at 300°C increased the sheet resistances up to 310-350 kΩ/sq range. In these films, crystals grow and reach the largest size among all films. As well known, grain boundary reduction by grain size increment results in a decrease in resistivity. Therefore, lower resistivity/sheet resistance values of the 300°C annealed film than those of as-deposited film are explained mainly by grain boundary reduction. Moreover, this film contains low resistance phases such as V₆O₁₃ and V₂O₃. On the other hand, growing of the pores into large sizes can create an increasing effect on the film resistance. The TCRs of these films could not be calculated due to fluctuations in voltage although they showed lower sheet resistances than as-deposited films. This was attributed to the highly defective structure of the film.

As it is given in the literature review (see section 1.4), multiple factors can contribute to film 1/f noise property: microstructure, crystallinity, film resistivity and grain size. The general understanding is that 1/f noise decreases with increasing crystallinity, whereas film resistivity is directly proportional to 1/f noise. A

microstructure with nano-size crystals distributed over the film matrix can enhance 1/f noise properties of thin films. On the other hand, 1/f noise is expected to decrease with increasing grain size due to the grain boundary reduction [18]. However, large grains of VO₂ phase existing in film structure increase the 1/f noise because of the martensite characteristic of VO₂ [10]. In our case, we observed that 1/f noise does not alter coherently with film resistivity. The crystallinity also can not explain the 1/f noise variation: the 300°C annealed film has the highest 1/f noise value despite exhibiting the highest crystallinity. Moreover, it had been expected for this film to represent lower 1/f noise value because of the grain growth. Thus, this high value of 1/f noise can be mainly explained by the large VO₂ grains occurring inside the mixed phase content of the film. In accordance with this comment, the as-deposited film exhibits lower 1/f noise value; suggesting that the smaller VO₂ grains of the film introduce less noise into the film. For the 200°C annealed film, the 1/f noise value is the lowest among all films. This film has the smallest grain sizes including VO₂ grains. Therefore, it has already been expected from this film to show the lowest 1/f noise property. It is known that inhomogeneities and defective structure are the source of the 1/f noise. Therefore, the nanopores observed in the VO_x films may have an influence on noise property of the films. However, in order to understand the individual role of nanopores over 1/f noise property, further studies must be carried out.

5. CONCLUSION

VO_x thin films were deposited on Si₃N₄/SiO₂/Si substrates by PDC-RMS technique. From GIXRD, Raman, XPS and TEM measurements it was shown that the films consist of various phases of VO_x. The elemental mapping study revealed the porous structure of the films. In order to make the structure-property correlation, the electrical properties of the films discussed on the basis of the structural results. It is concluded that the 1/f noise variation observed in the as-deposited, 200°C and 300°C annealed films is mainly associated with the different grain size of VO₂ included inside the film structure. It was suggested that the charge hopping mechanism can be applied to the film at 200°C in order to explain electrical conduction in the film.

REFERENCES

- [1] Bahlawane, N., & Lenoble, D. (2014). Vanadium oxide compounds: structure, properties, and growth from the gas phase. *Chemical Vapor Deposition*, 20(7-8-9), 299-311.
- [2] Perucchi, A., Baldassarre, L., Postorino, P., & Lupi, S. (2009). Optical properties across the insulator to metal transitions in vanadium oxide compounds. *Journal of Physics: Condensed Matter*, 21(32), 323202.
- [3] Su, Y. Y., Cheng, X. W., Li, J. B., Dou, Y. K., Rehman, F., Su, D. Z., & Jin, H. B. (2015). Evolution of microstructure in vanadium oxide bolometer film during annealing process. *Applied Surface Science*, 357, 887-891.
- [4] Benkahoul, M., Zayed, M. K., Solieman, A., & Alamri, S. N. (2017). Spray deposition of V₄O₉ and V₂O₅ thin films and post-annealing formation of thermochromic VO₂. *Journal of Alloys and Compounds*, 704, 760-768.
- [5] Yamazaki, S., Li, C., Ohoyama, K., Nishi, M., Ichihara, M., Ueda, H., & Ueda, Y. (2010). Synthesis, structure and magnetic properties of V₄O₉—a missing link in binary vanadium oxides. *Journal of Solid State Chemistry*, 183(7), 1496-1503.
- [6] Arora, S., Paras, N., Gurjar, A., Narwal, R., Prasad, B., & Kumar, D. (2016, April). Design and simulation of uncooled microbolometer using coventorware. In *AIP Conference Proceedings* (Vol. 1724, No. 1, p. 020124). AIP Publishing.
- [7] H. Budzier and G. Gerlach, "Introduction," in *Thermal infrared sensors*, John Wiley & Sons, 2011, pp. 1-14.
- [8] Wang, B., Lai, J., Li, H., Hu, H., & Chen, S. (2013). Nanostructured vanadium oxide thin film with high TCR at room temperature for microbolometer. *Infrared Physics & Technology*, 57, 8-13.
- [9] Chen, X. Q. (2010). Linear microbolometric array based on VO_x thin film. *Journal of Infrared, Millimeter, and Terahertz Waves*, 31(5), 566-573.
- [10] Zerov, V. Y., Kulikov, Y. V., Malyarov, V. G., Khrebtov, I. A., Shaganov, I. I., & Shadrin, E. B. (2001). Vanadium oxide films with improved characteristics for IR microbolometric matrices. *Technical Physics Letters*, 27(5), 378-380.
- [11] Ahmed, A., & Tait, R. N. (2005). Noise behavior of amorphous Ge_xSi_{1-x}O_y for microbolometer applications. *Infrared physics & technology*, 46(6), 468-472.
- [12] Chi-Anh, N., & Moon, S. (2007). Excess noise in vanadium tungsten oxide bolometric material. *Infrared physics & technology*, 50(1), 38-41.

- [13] Ryu, H., Kwon, S., Cheon, S., Cho, S. M., Yang, W. S., & Choi, C. A. (2009). Evaluation of 1/f noise characteristics for Si-based infrared detection materials. *ETRI journal*, 31(6), 703-708.
- [14] Kim, D. S., Kwon, I. W., Lee, Y. S., & Lee, H. C. (2011). The bolometric characteristic of thermally oxidized thin nickel film for an uncooled infrared image sensor. *Infrared Physics & Technology*, 54(1), 10-12.
- [15] Basantani, H. A., Kozlowski, S., Lee, M. Y., Li, J., Dickey, E. C., Jackson, T. N., ... & Horn, M. (2012). Enhanced electrical and noise properties of nanocomposite vanadium oxide thin films by reactive pulsed-dc magnetron sputtering. *Applied Physics Letters*, 100(26), 262108.
- [16] Xu, R., Li, W., He, J., Sun, Y., & Jiang, Y. D. (2013). Boron-doped nanocrystalline silicon germanium thin films for uncooled infrared bolometer applications. *Infrared Physics & Technology*, 58, 32-35.
- [17] Shin, Y. B., Reddy, Y. A. K., Kang, I. K., & Lee, H. C. (2016). Nb doping effect on TiO_{2-x} films for bolometer applications. *Journal of Physics and Chemistry of Solids*, 91, 128-135.
- [18] Barhoumi, A., Leroy, G., Yang, L., Gest, J., Boughzala, H., Duponchel, B., ... & Carru, J. C. (2014). Correlations between 1/f noise and thermal treatment of Al-doped ZnO thin films deposited by direct current sputtering. *Journal of Applied Physics*, 115(20), 204502.
- [19] Kumar, R. R., Karunakaran, B., Mangalaraj, D., Narayandass, S. K., Manoravi, P., Joseph, M., ... & Singh, J. P. (2003). Room temperature deposited vanadium oxide thin films for uncooled infrared detectors. *Materials Research Bulletin*, 38(7), 1235-1240.
- [20] Berezina, O., Kirienko, D., Pergament, A., Stefanovich, G., Velichko, A., & Zlomanov, V. (2015). Vanadium oxide thin films and fibers obtained by acetylacetonate sol-gel method. *Thin Solid Films*, 574, 15-19.
- [21] Subrahmanyam, A., Reddy, Y. B. K., & Nagendra, C. L. (2008). Nano-vanadium oxide thin films in mixed phase for microbolometer applications. *Journal of Physics D: Applied Physics*, 41(19), 195108.
- [22] Ingole, R. S., & Lokhande, B. J. (2016). Effect of pyrolysis temperature on structural, morphological and electrochemical properties of vanadium oxide thin films. *Journal of Analytical and Applied Pyrolysis*, 120, 434-440.
- [23] Qiao, Y., Lu, Y., Yang, H., & Ling, Y. S. (2014). DC Magnetron Sputtering Deposition of Room-Temperature Phase Transition Vanadium Oxide Film. In *Advanced Materials Research* (Vol. 1053, pp. 332-336). Trans Tech Publications.

- [24] Ohring, M. (2001). *Materials science of thin films*. Academic press.
- [25] Safi, I. (2000). Recent aspects concerning DC reactive magnetron sputtering of thin films: a review. *Surface and Coatings Technology*, 127(2), 203-218.
- [26] Choi, J. O., Lee, H. S., & Ko, K. H. (2014). Oxidation potential control of VO₂ thin films by metal oxide co-sputtering. *Journal of materials science*, 49(14), 5087-5092.
- [27] Sellers, J. (1998). Asymmetric bipolar pulsed DC: the enabling technology for reactive PVD. *Surface and Coatings Technology*, 98(1-3), 1245-1250.
- [28] Chen, X., Lv, Q., & Yi, X. (2012). Smart window coating based on nanostructured VO₂ thin film. *Optik-International Journal for Light and Electron Optics*, 123(13), 1187-1189.
- [29] Huang, Z., Chen, C., Lv, C., & Chen, S. (2013). Tungsten-doped vanadium dioxide thin films on borosilicate glass for smart window application. *Journal of Alloys and Compounds*, 564, 158-161.
- [30] Yang, F. W., Chen, K. H., Cheng, C. M., & Su, F. Y. (2013). Bipolar resistive switching properties in transparent vanadium oxide resistive random access memory. *Ceramics International*, 39, S729-S732.
- [31] Chen, C., Yi, X., Zhang, J., & Zhao, X. (2001). Linear uncooled microbolometer array based on VO_x thin films. *Infrared physics & technology*, 42(2), 87-90.
- [32] Öksüzöğlü, R. M., Bilgiç, P., Yıldırım, M., & Deniz, O. (2013). Influence of post-annealing on electrical, structural and optical properties of vanadium oxide thin films. *Optics & Laser Technology*, 48, 102-109.
- [33] Khatibani, A. B., Abbasi, M., & Rozati, S. M. (2016). Peculiarities of Deposition Times on Gas Sensing Behaviour of Vanadium Oxide Thin Films. *Acta Physica Polonica, A*, 129(6).
- [34] Han, S. D., Moon, H. G., Noh, M. S., Pyeon, J. J., Shim, Y. S., Nahm, S., ... & Kang, C. Y. (2017). Self-doped nanocolumnar vanadium oxides thin films for highly selective NO₂ gas sensing at low temperature. *Sensors and Actuators B: Chemical*, 241, 40-47.
- [35] Hendaoui, A., Émond, N., Chaker, M., & Haddad, É. (2013). Highly tunable-emittance radiator based on semiconductor-metal transition of VO₂ thin films. *Applied Physics Letters*, 102(6), 061107.

- [36] Sun, H., Hou, X., Wei, Q., Liu, H., Yang, K., Wang, W., ... & Rong, Y. (2016). Low-temperature solution-processed p-type vanadium oxide for perovskite solar cells. *Chemical Communications*, 52(52), 8099-8102.
- [37] Lv, Y., Hu, M., Wu, M., & Liu, Z. (2007). Preparation of vanadium oxide thin films with high temperature coefficient of resistance by facing targets dc reactive sputtering and annealing process. *Surface and Coatings Technology*, 201(9), 4969-4972.
- [38] Zia, M. F., Abdel-Rahman, M., Alduraibi, M., Ilahi, B., & Alasaad, A. (2016). Synthesis and electrical characterisation of vanadium oxide thin film thermometer for microbolometer applications. *Electronics Letters*, 52(10), 827-828.
- [39] Benmoussa, M., Ibnouelghazi, E., Bennouna, A., & Ameziane, E. L. (1995). Structural, electrical and optical properties of sputtered vanadium pentoxide thin films. *Thin solid films*, 265(1-2), 22-28.
- [40] Raj, P. D., Gupta, S., & Sridharan, M. (2015). Nanostructured V₂O₅ thin films deposited at low sputtering power. *Materials Science in Semiconductor Processing*, 39, 426-432.
- [41] Niklaus, F., Vieider, C., & Jakobsen, H. (2008, January). MEMS-based uncooled infrared bolometer arrays: a review. In *MEMS/MOEMS technologies and applications III* (Vol. 6836, p. 68360D). International Society for Optics and Photonics.
- [42] Fieldhouse, N., Pursel, S. M., Horn, M. W., & Bharadwaja, S. S. N. (2009). Electrical properties of vanadium oxide thin films for bolometer applications: processed by pulse dc sputtering. *Journal of Physics D: Applied Physics*, 42(5), 055408.
- [43] Dong, X., Wu, Z., Xu, X., Wang, T., & Jiang, Y. (2014). Effects of duty cycle and oxygen flow rate on the formation and properties of vanadium oxide films deposited by pulsed reactive sputtering. *Vacuum*, 104, 97-104.
- [44] Goltvyanskyi, Y., Khatsevych, I., Kuchuk, A., Kladko, V., Melnik, V., Lytvyn, P., ... & Romanyuk, B. (2014). Structural transformation and functional properties of vanadium oxide films after low-temperature annealing. *Thin Solid Films*, 564, 179-185.
- [45] Yağcı A. M., (2015). *Electrical and 1/f noise Characterization of Nano Scale Vanadium Oxide Thin Films*. Unpublished Master's Thesis, Eskişehir: Anadolu University
- [46] Abdel-Rahman, M., Al-Khalli, N., Zia, M. F., Alduraibi, M., Ilahi, B., Awad, E., & Debbar, N. (2017, February). Fabrication and design of vanadium oxide

- microbolometer. In *AIP Conference Proceedings* (Vol. 1809, No. 1, p. 020001). AIP Publishing.
- [47] Nishi, Y., & Doering, R. (Eds.). (2000). *Handbook of semiconductor manufacturing technology*. CRC Press.
- [48] Miccoli, I., Edler, F., Pfnür, H., & Tegenkamp, C. (2015). The 100th anniversary of the four-point probe technique: the role of probe geometries in isotropic and anisotropic systems. *Journal of Physics: Condensed Matter*, 27(22), 223201.
- [49] Tupta, M. A. (2016). Resistivity measurements using a four-point collinear probe. *EE-Evaluation Engineering*, 55(11), 18-20.
- [50] Smits, F. M. (1958). Measurement of sheet resistivities with the four-point probe. *Bell Labs Technical Journal*, 37(3), 711-718.
- [51] Inaba, K. (2008). X-ray thin-film measurement techniques. *Overview. Rigaku J*, 24(1).
- [52] Hofmann, S. (2012). *Auger-and X-ray photoelectron spectroscopy in materials science: a user-oriented guide* (Vol. 49). Springer Science & Business Media.
- [53] Ureña-Begara, F., Crunteanu, A., & Raskin, J. P. (2017). Raman and XPS characterization of vanadium oxide thin films with temperature. *Applied Surface Science*, 403, 717-727.
- [54] Silversmit, G., Depla, D., Poelman, H., Marin, G. B., & De Gryse, R. (2004). Determination of the V2p XPS binding energies for different vanadium oxidation states (V 5+ to V 0+). *Journal of Electron Spectroscopy and Related Phenomena*, 135(2), 167-175.
- [55] Cushman, C. V., Chatterjee, S., Major, G. H., Smith, N. J., Roberts, A., & Linford, M. R. (2016). Trends in Advanced XPS Instrumentation. *Vacuum Technology and Coating* November.
- [56] Bumbrah, G. S., & Sharma, R. M. (2016). Raman spectroscopy–Basic principle, instrumentation and selected applications for the characterization of drugs of abuse. *Egyptian Journal of Forensic Sciences*, 6(3), 209-215.
- [57] <http://www.spectroscopyonline.com/understanding-raman-spectrometer-parameters> (Accessed: 15.12.2015)
- [58] Zhang, C., Yang, Q., Koughia, C., Ye, F., Sanayei, M., Wen, S. J., & Kasap, S. (2016). Characterization of vanadium oxide thin films with different stoichiometry using Raman spectroscopy. *Thin Solid Films*, 620, 64-69.

- [59] Julien, C., Nazri, G. A., & Bergström, O. (1997). Raman scattering studies of microcrystalline V6O13. *physica status solidi (b)*, 201(1), 319-326.
- [60] Krumeich, F. (2011). Properties of electrons, their interactions with matter and applications in electron microscopy. *Laboratory of Inorganic Chemistry, disponível em <http://www.microscopy.ethz.ch/downloads/Interactions.pdf>, consultado em, 3-08.*
- [61] Fultz, B., & Howe, J. M. (2012). *Transmission electron microscopy and diffractometry of materials*. Springer Science & Business Media.
- [62] Williams, D. B., & Carter, C. B. (1996). The transmission electron microscope. In *Transmission electron microscopy* (pp. 3-17). Springer Us.
- [63] Krumeich, F., Muhr, H. J., Niederberger, M., Bieri, F., & Nesper, R. (2000). The Cross-Sectional Structure of Vanadium Oxide Nanotubes Studied by Transmission Electron Microscopy and Electron Spectroscopic Imaging. *Zeitschrift für anorganische und allgemeine Chemie*, 626(10), 2208-2216.
- [64] Venkatasubramanian, C., Cabarcos, O. M., Drawl, W. R., Allara, D. L., Ashok, S., Horn, M. W., & Bharadwaja, S. S. N. (2011). Process-structure-property correlations in pulsed dc reactive magnetron sputtered vanadium oxide thin films. *Journal of Vacuum Science & Technology A: Vacuum, Surfaces, and Films*, 29(6), 061504.
- [65] Ju, Y., Wang, M., Wang, Y., Wang, S., & Fu, C. (2013). Electrical properties of amorphous titanium oxide thin films for bolometric application. *Advances in Condensed Matter Physics*, 2013.
- [66] Wepasnick, K. A., Smith, B. A., Bitter, J. L., & Fairbrother, D. H. (2010). Chemical and structural characterization of carbon nanotube surfaces. *Analytical and bioanalytical chemistry*, 396(3), 1003-1014.
- [67] Porwal, D., Esther, A. C. M., Reddy, I. N., Sridhara, N., Yadav, N. P., Rangappa, D., ... & Dey, A. (2015). Study of the structural, thermal, optical, electrical and nanomechanical properties of sputtered vanadium oxide smart thin films. *RSC Advances*, 5(45), 35737-35745.
- [68] Zimmermann, R., Claessen, R., Reinert, F., Steiner, P., & Hüfner, S. (1998). Strong hybridization in vanadium oxides: evidence from photoemission and absorption spectroscopy. *Journal of Physics: Condensed Matter*, 10(25), 5697.
- [69] Demeter, M., Neumann, M., & Reichelt, W. (2000). Mixed-valence vanadium oxides studied by XPS. *Surface Science*, 454, 41-44.

- [70] Chen, R. H., Jiang, Y. L., & Li, B. Z. (2014). Influence of post-annealing on resistivity of VO_x thin film. *IEEE Electron Device Letters*, 35(7), 780-782

RESUME

PERSONAL DETAILS

Name, Surname : Emrah Dirican
Foreign Language : English
Date of Birth : 26/07/1988
E-mail : edirican@anadolu.edu.tr

EDUCATION

2017 MSc at A Anadolu University, Graduate School of Science, Material Science and Engineering
2014 BSc at Anadolu University, Faculty of Engineering, Material Science and Engineering

PUBLICATIONS AND ACTIVITIES

2017, Conference Abstract, Evolution of VOx Thin Film Structure by Post-Annealing: TEM and ESI Investigation, *Authors: Emrah Dirican, Gökçenur Çakmak, Ercan Şener, Ramis Mustafa Öksüzoğlu*, 33rd International Physics Congress of Turkish Physical Society, Bodrum/Turkey, page 609, September 6-10

2016, Poster Presentation, Transmission Electron Microscopy Investigation of Vanadium Oxide Thin Films, *Authors: Emrah Dirican, Ercan Şener, Ahmet Murat Yağcı, Ramis Mustafa Öksüzoğlu*, 12th International Nanoscience and Nanotechnology Conference, Gebze Technical University, page 272, June 03-05

2016, Conference Abstract, Post annealing effects on structural and electrical properties of nanoscale VOx thin films, *Authors: Ercan Şener, Emrah Dirican and R. Mustafa Öksüzoğlu*, 12th Nano Science and Nano Technology Conference, Gebze Technical University, page 446, June 03-05

2016, Conference Abstract, Structure-electronic property correlation in nanoscale VOx thin films, *Authors: R. Mustafa Öksüzoğlu, Ahmet Murat Yağcı, Emrah Dirican, and Ercan Şener*, 12th Nano Science and Nano Technology Conference, Gebze Technical University, page 109, June 03-05

2015, Poster Presentation, Nano Ölçekli Vanadyum Oksit İnce Filmlerin Yapısal Karakterizasyonu, *Authors: Emrah Dirican, Ercan Şener, Ahmet Murat Yağcı, Ramis Mustafa Öksüzoğlu*, YMF21-Intense Material Physics Ankara Meeting, Gazi University, page 101, December 25

2015, Poster Presentation, Electrical Characterization of Nano-Size Grained Vanadium Oxide Thin Films, *Authors: Emrah Dirican, Ahmet Murat Yağcı, Sinan Özgün, Can Yavru, Rifat Kaçar, Ramis Mustafa Öksüzoğlu*, 11th International Nanoscience and Nanotechnology Conference, METU, June 22-25

2015, Conference Abstract, Mikro-Raman and XRD Study of VOx Deposited by Pulse DC-Magnetron Sputtering After Annealing, *Authors: Can Yavru, Ramis Mustafa Öksüzoğlu, Emrah Dirican, Erhan Ayas*, 11th Nano Science and Nano Technology Conference, June 23 – 25, METU, poster session 1/P32

2013, Participation as a listener, "The Materials Education Symposium (3MES)",
Anadolu University, November